Università
degli Studi
di Catania

Dottorato di Ricerca
in Scienza dei Materiali
XXV Ciclo (2009-2012)

"In Liquid" Laser Processes for Metal Nanoparticles Synthesis and Manipulation

Gabriele Carmine Messina

Tutor:
Chiar.mo Prof. G. Compagnini
Coordinatore:
Chiar.mo Prof. A. Licciardello

SCOPE OF THE THESIS

Last decades have seen an exponential spread of high level technology in everyday life. Leading trends of this explosion have been mainly two: miniaturization, since carrying a small device in a pocket means its daily use, and accessibility, because cheaper products can be afforded by larger audiences. The research of new materials able to fulfill these characteristics seems to be a logical consequence of these tendencies and probably one of the reasons for the increase of scientific interest into the nanotechnology field. Indeed, the possibility of applications of these intriguing structures in the construction of devices is becoming concrete. The step to the nanometric size involves the appearing of peculiar properties which are not present in the bulk state and this characteristic is of undeniable appeal for technological purposes. Among the large variety of different entities, metal nanoparticles are playing a major role because of their unique optical, electrical and antibacterial properties, which make them perfect candidates as base for the preparation of devices with applications in microelectronics, photonics and medical fields. In this regard, the need for pure, ligand-free nanoparticles with desired size and shape is a relevant problem both from the scientific and industrial point of interest. It is well known that Pulsed Laser Ablation in Liquid (PLAL) represents a universal technique for the preparation of innovative nanomaterials with desired characteristics. The simple variation of the nature of the target and the surrounding liquid allows the formation of a

large choice of different nanostructures, ranging from metal nanoparticles to oxides or carbon structures. Also the tuning of the laser parameters, such as energy and repetition rate, influences the characteristics of the obtained product. Furthermore, since the care of environment is becoming a topic of main interest, it should not be forgotten that laser ablation can be considered a green technique. Indeed, the absence of dangerous chemicals and the simple work conditions, such as room temperature and atmospheric pressure, point at this technique as environmentally friendly. For the reasons above, laser ablation seems to be an optimal candidate for the production of metal nanoparticles on large scale but, till now, the low production yield of this technique has stopped every attempt in this direction. In this view, the development of new strategies to increase the efficiency of laser ablation represents an interesting field of research. A study of the physics fundamentals of the process is also required in order to determine the parameters driving the efficiency variation. Nanoparticles produced by laser ablation in liquid could be used as pure or their properties can be enhanced by obtaining nanocomposites with different materials. Thus, the accurate characterization of the obtained material, together with a proper manipulation, are topics of primary importance.

CHAPTER 1: METAL NANOPARTICLES AND THEIR PROPERTIES

1.1 INTRODUCTION

The word nanocluster indicates an ensemble of atoms with dimensions varying from a few nanometers to a few hundreds. In this range of size, the increase of the ratio between the surface and the number of inner atoms is responsible for peculiar behaviours of the structure, leading to the appearance of several quantum properties which cannot be found in the bulk structure of the metal. The presence of these characteristics is appealing when considering the development of innovative materials. In this optic, metal nanoclusters can be considered as starting building blocks for the formation of larger structures with the same chemical nature or they can be mixed together with other materials such as polymers or inorganic materials to create new composites. The production of metal nanoparticles can be obtained by different techniques and the properties of the final product will depend on the chosen route. Conventionally, it is possible to distinguish between chemical and physical preparation methods even if, looking deeply at involved mechanisms, a marked boundary does not really exist. Chemical methods, often identified also as “wet” methods, since such approaches

work in liquid environment, are mainly based on the reduction of a precursor of the desired metal in aqueous or organic solutions. The Turkevitch method, developed in 1951, allows the preparation of gold nanoparticles with dimensions in the range of 10-100 nm, by the reduction of $HAuCl_4$ in a boiling solution of sodium citrate **[1]**. The role of citrate molecules is to act as reducing agents but also as stabilizers for nanoparticles. The same procedure can be applied for obtaining silver nanoparticles starting from $AgNO_3$, but with limited size control **[2]**. Nanoparticles prepared by chemical methods can be functionalized with ligands, simply adding the proper molecule to the solution. The attachment of ligands with nanoparticles is usually achieved by the presence of a sulphur termination on the molecules, which is known to strongly interact with metals such gold and silver.

Physical approaches to preparation of nanoparticles generally involve the removing of material from a solid target by different methods, such as sputtering or vaporization (in the case of Physical Vapour Deposition). The material is then driven through a reactor by a carrier gas to a zone where nucleation and growth happens and then nanoparticles are deposited on a substrate, obtaining thin films.

A particular case is represented by Chemical Vapour Deposition, in which nanoparticles are grown from volatile precursors of the desired metal. Vaporised precursors are then introduced into a reactor and absorbed onto a substrate which is held at high temperature, where absorbed molecules will thermally decompose or react with other vapours to form crystals. Main disadvantages of physical techniques are

that obtained nanoparticles are bound to a substrate and that deposited films can be contaminated by bubbles due the presence of carrier gas.
Among routes to obtain metal nanoparticles, a relevant role has been assumed by pulsed laser ablation (PLA). This approach, and in particular its variant in liquid, is indeed becoming the preparation of choice since presents a lot of advantages like the high purity of produce obtained nanoparticles, the applicability to almost all metals, the relative low cost and the eco-compatibility.

1.2 OPTICAL PROPERTIES

The smoothed surface of metals in bulk state presents a shiny appearance, and this behaviour is attributed to the total reflection of light due to the high density of electrons in the material. Contrariwise, finely divided metals look dark, because the large surface absorbs light through repeated reflection phenomena **[3]**. When metals reach nanometer size, strong absorption of light can happen when the frequency of the electromagnetic field becomes resonant with the coherent electron movement **[4]**. In the case of Au, Ag and Cu, which present free conduction electrons with plasma frequency in the visible region, nanoparticles appear colored **[5]**. Other transition metals, instead, show only broad and poorly resolved absorption bands in the ultraviolet region **[4]**. This singular characteristic is known and used since ancient times. Indeed, first evidences of colloidal solution of gold have been found in

the 5th and 4th century B.C. in Egypt and China, probably used for coloring glass and ceramics **[6]**. Among ancient artifacts, one of the most famous examples is the so-called "Lycurgus cup", a glass vessel which appears green in reflected light and red in transmitted light, dated 4th century A.D **[7]**. The nice visual effect of the cup has been attributed to the presence of a mixture of gold and silver colloids (with size ~70 nm) embedded in the glass matrix **[5]**.

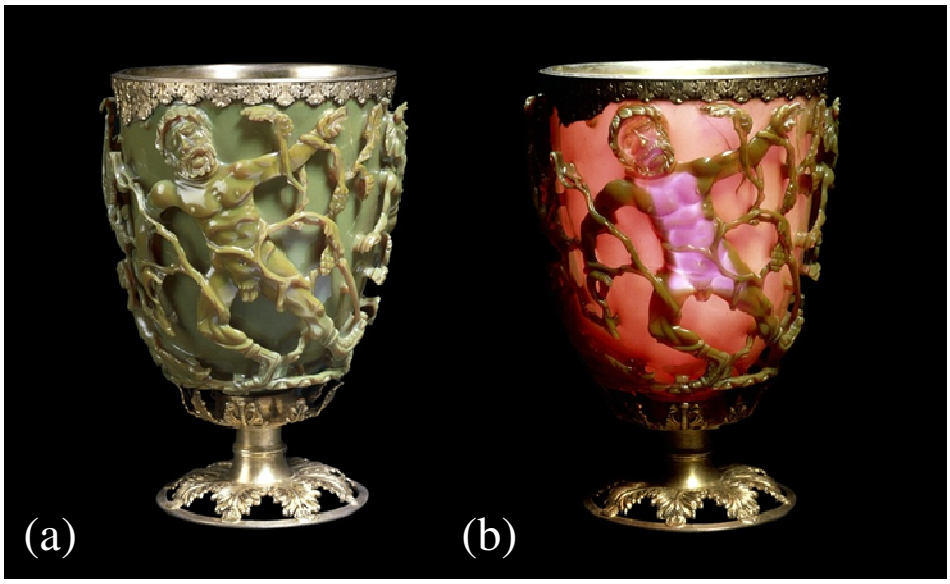

Figure 1.1 Views of the "Lycurgus cup" in (a) reflected and (b) transmitted light. From ref. **[7]**.

Metal nanoparticles were also used during the Middle Ages for the fabrication of stained glass in cathedrals **[8]**.

The first analytical approach to optical properties of gold particles in hydrosols can be recognized to Michael Faraday, with his 1857 article "Experimental Relations of Gold (and other Metals) to light" **[9]**. He attributes the ruby color to the presence of "finely dispersed" gold in solution, obtained reducing dilute gold chloride with phosphorus and tartaric acid or by heating, and widely discusses about size dependent optical properties and coagulation behaviour of gold and other metals such as platinum, palladium, rhodium, silver, tin, lead, zinc, iron, mercury, arsenic. Today is widely known that the color and optical properties of metal nanoparticles are due to the presence of a collective longitudinal excitation of conduction electrons on the surface of the nanoparticles, known as Surface Plasmon Resonance (SPR) **[10]**.

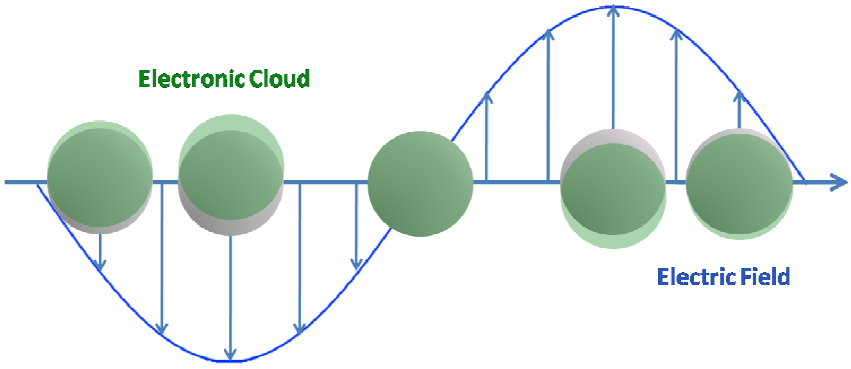

Figure 1.2 Schematic representation of the electronic cloud displacement as consequence of an oscillating electric field.

According to the Fermi liquid model, it is possible to consider a plasmon as a negatively charged electron cloud displaced from its equilibrium position around a lattice made of positively charged ions, similarly to real plasma.

This phenomenon can be described with an electrostatic model that assumes the approximation of surface electrons (with number density N and charge e) to a monodimensional slab.

If an electric field E_{app} is applied to the slab, it generates a force that can be written as:

$$F = -eE_{app} \tag{1.1}$$

Then, the charge is moved from its initial position of a displacement x and the total surface density at each end of the slab will be:

$$\sigma = Nex \tag{1.2}$$

According to Gauss's law, the field created between two surface charges is given by:

$$E = \frac{\sigma}{\varepsilon_0} \tag{1.3}$$

where ε_0 is the vacuum dielectric permittivity.

The presence of this field creates a restoring force opposite to the one described in eq. (1.1):

$$F_s = -eE_s = -\frac{Ne^2x}{\varepsilon_0} \tag{1.4}$$

and so electrons will move according to:

$$F = m\frac{d^2x}{dt^2} = -\frac{Ne^2x}{\varepsilon_0} \tag{1.5}$$

where m is the electron effective mass.

Equation (1.5) can be also written as:

$$\frac{d^2x}{dt^2} = -\frac{Ne^2}{\varepsilon_0 m}x \tag{1.6}$$

and solution to this equation is given by:

$$x = A\cos\omega t \tag{1.7}$$

with characteristic oscillation frequency ω_p:

$$\omega_p = \sqrt{\frac{Ne^2}{\varepsilon_0 m_e}} \tag{1.8}$$

Qualitatively, the irradiation of a metal nanoparticle by the oscillating electric field of light causes the coherent oscillation of conduction electrons. When the electron cloud is displaced from the nuclei, the coulomb attraction between electrons and nuclei produces a restoring force that results in oscillation of the electron cloud relative to the nuclei. The oscillation frequency depends on the density of electrons, the effective electron mass and shape and size of charge distribution.

1.2a Introduction to Mie Theory

In 1908, Mie wrote a seminal paper titled “Beiträge zur Optik trüber Medien, speziell kolloidaler Metallösungen” (literally “Contributions on the optics of turbid media, particularly colloidal metal solutions”) **[11]**, in which he presented a solution to Maxwell’s equations that describes the extinction spectra (where extinction is a term that includes scattering and absorption contributes) of spherical particles of arbitrary size. Even though the Mie model is relatively aged, it still remains of great interest being the only simple, exact solution to Maxwell’s equations that is relevant to describe nanoparticles behaviour **[12]**. Anyway, the pure Mie

approximation in general is not accurate enough to describe real situations, since the presence of complicating factors in understanding the nanoparticle optical properties, including the presence of a supporting substrate, a solvent layer on the top of nanoparticles, or particles close enough to lead to electromagnetic couplings **[12]**. Later, Gans **[13]** extended the theory to spheroid particles, showing how smaller non spherical particles can show absorbance at longer wavelength respect to sphere of the same dimension.

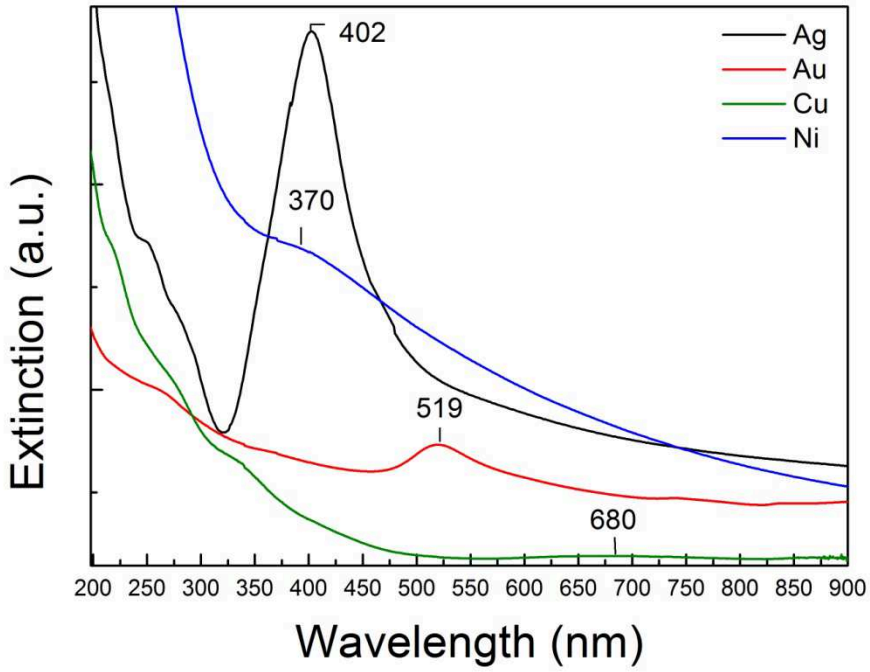

Figure 1.3 UV-Vis spectra showing the SPR peaks of silver, gold, copper and nickel colloidal solutions obtained by laser ablation of pure metals in water.

1.2b Dipole Plasmon Resonance

The plasmon resonance phenomenon has been widely discussed in literature **[12,14-15]**.

The most common approach correlates the plasmon frequency with the metal dielectric constant, which is a property that can be measured as a function of wavelength for bulk metals. Considering the interaction of light with a spherical particle smaller than the wavelength of the light, the electric field of light can be taken as constant, so the interaction is governed by electrostatics rather than electrodynamics. This is often called the quasi-static approximation, as the wavelength-dependent dielectric constant of the metal particle, ε_i and the surrounding medium ε_m are used in what is otherwise an electrostatic theory.

The electric field of the incident electromagnetic wave is denoted by the vector E_0, which is constant in the x direction so that it can be written as:

$$E_0 = E_0\hat{x} \tag{1.9}$$

where $\hat{x}$ is a unit vector.

The electromagnetic field surrounding the particle is determined by solving Laplace's equation

$$\nabla^2\varphi = 0 \tag{1.10}$$

where φ is the electric potential.

The electromagnetic field E is related to the potential φ by the equation:

$$E = -\nabla\varphi \tag{1.11}$$

In developing this solution, two boundary conditions are applied:

- The potential φ is continuous at the sphere surface.

- The normal component of the electric displacement D is also continuous, where $D=\varepsilon E$.

General solution to the Laplace's equation presents angular solutions which are just the spherical harmonics. In addition, the radial solutions are of the form r^l and $r^{-(l+1)}$ where l is the familiar angular momentum label (l=0,1,2,…) of atomic orbitals.

Considering just the l=1 solution and the field E_0 in the x direction, the potential inside a sphere of radius R (where $r<R$) is given by:

$$\varphi = Ar\sin\theta\cos\phi \tag{1.12}$$

while outside the sphere (r>R) it will be:

$$\varphi = (-E_0 r + B/r^2)\sin\theta\cos\phi \tag{1.13}$$

where A and B are constants to be determined.

Inserting these solutions into the boundary conditions and using the resulting potential φ to determine the field outside the sphere E_{out}, it is possible to deduce:

$$E_{out} = E_0\hat{x} - \alpha E_0\left[\frac{\hat{x}}{r^3} - \frac{3x}{r^5}(x\hat{x} + y\hat{y} + z\hat{z})\right] \tag{1.14}$$

Where α is the sphere polarizability and $\hat{x}, \hat{y}$ and $\hat{z}$ the unit vectors.

In eq. (1.14) the first term represents the applied field while the second one represents the induced dipole field (with induced dipole moment given by αE_0) that results from polarization of the conduction electron density.

For a sphere with the dielectric constant ε_i in a medium with dielectric constant ε_m, the solution to Laplace equation shows that the polarizability is given by:

$$\alpha = g_d R^3 \tag{1.15}$$

with

$$g_d = \frac{\varepsilon_i - \varepsilon_m}{\varepsilon_i + 2\varepsilon_m} \tag{1.16}$$

Although the dipole field in eq. (1.14) is that for a static dipole, the complete Maxwell's equation solution shows that this is actually a radiating dipole, and thus, it contributes to extinction and Rayleigh scattering by the sphere. From this it is possible to deduce the extinction and scattering efficiencies as:

$$Q_{ext} = 4xIm(g_d) \tag{1.17}$$

$$Q_{sca} = \frac{8}{3}x^4|g_d|^2 \tag{1.18}$$

where

$$x = \frac{2\pi R\sqrt{\varepsilon_m}}{\lambda} \tag{1.19}$$

The efficiency is the ratio of the cross section to the geometrical cross-section πR^2 as described by:

$$Q_{ext} = \frac{C_{ext}}{\pi R^2} \tag{1.20}$$

The factor g_d plays the key role in determining the wavelength dependence of these cross-sections, as the metal dielectric constant ε_i is strongly dependent on wavelength.

The extinction cross section C_{ext} is useful when predicting the absorption of small particles, since the attenuation of light in a dilute colloidal solution is given by **[16]**:

$$\frac{dI(\ell)}{dx} = -NC_{ext}I(\ell) \tag{1.21}$$

Where N is the number density of particles, I_0 is the intensity of light, ℓ is the path length in the spectrometer in cm.

Integration of eq. (1.21) gives the optical absorption of the solution:

$$A = \log_{10} \frac{I_0}{I(\ell)} \frac{C_{ext}}{2.303} \quad (1.22)$$

For small spherical particles ($2R<<\lambda$, where the dipole approximation is still valid), with a complex frequency-dependent dielectric function $\varepsilon_i = \varepsilon' + i\varepsilon''$, embedded in a medium of dielectric function ε_m, the extinction cross section is expressed by **[11,17-20]**:

$$C_{ext} = \frac{24\pi^2 R^3 \varepsilon_m^{3/2}}{\lambda} \frac{\varepsilon''}{(\varepsilon' + 2\varepsilon_m)^2 + \varepsilon''^2} \quad (1.23)$$

This equation predicts the existence of an absorption peak when $\varepsilon'(\omega) = -2\varepsilon_m$, while ε'' is small or weakly dependent from ω **[5,21]**.

It is also possible to notice that no absorption is contemplated for two opposite values of the imaginary part of the dielectric function, since the cross section assumes a zero value if $\varepsilon'' = 0$ (non absorption case) but also if $\varepsilon'' = \infty$ (complete reflection of light) **[16]**.

C_{ext} depends on R^3, while the number density decreases as R^3 for a given amount of colloidal material. Therefore the absorption coefficient is independent of particle size **[16]**.

Nevertheless, a dependence on the size has been observed experimentally **[14]**. This discrepancy arises from the assumption in the Mie theory that the electronic structure and dielectric constant of nanoparticles are the same as those of its bulk form, which becomes no longer valid when the particle size becomes very small **[21]**.

Indeed in small particles, electron surface scattering becomes significant **[22-24]**, because the mean free path of conduction electrons (40-50 nm in silver and gold **[25]**) is bigger than the physical dimension of the

particles themselves. The scattering of electrons with the surface in an elastic but random way will cause the loss of coherence of the overall plasmon oscillation. Also inelastic electron surface collisions will contribute to the change of the phase. This can be taken in account changing the dielectric constant of the particles, which becomes size dependent **[14,21-24]**, and an increase of the plasmon bandwidth results at the decreasing of the particle size. When the dimensions of nanoparticles further decrease, and the nanoparticles size is comparable to de Broglie's wavelength of an electron at the Fermi energy (diameters of 1-2 nm), the surface plasmon band disappears **[26-28]** because the assumption of a delocalized electronic gas is no longer valid and particles should be treated as molecular clusters with discrete electronic levels. Therefore it is possible to observe fluorescence emission due to optical transitions between single electronic states **[21]**.

On the other way, for larger particles the dipole approximation is no longer valid and it is necessary to consider also higher order oscillations, which give a size dependence of the plasmon band position (that shows a red shift with increasing diameter) as well as an increase in the bandwidth **[12]**.

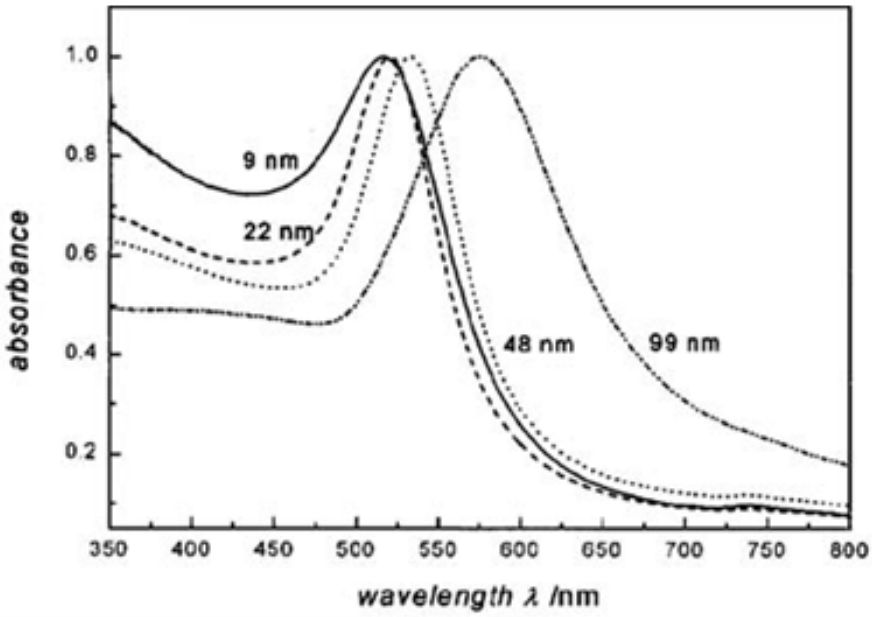

Figure 1.4 UV-Vis spectra of spherical Au nanoparticles with different sizes ranging from 9 to 99 nm, showing variation of the SPR peak on dimensions. From ref. **[29]**.

1.2c Quadrupole Plasmon Resonance

Among higher modes of plasmon excitation it is worth discussing the quadrupole mode (l=2), where half of the electron cloud moves parallel to the applied field and half moves antiparallel **[12]**. Using the same notation used for the dipole plasmon resonance and including the $l=2$ term in the Laplace equation solution, the resulting field outside the sphere, E_{out}, can be expressed as:

$$E_{out} = E_0\hat{x} + ikE_0(x\hat{x} + z\hat{z}) - \alpha E_0\left[\frac{\hat{x}}{r^3} - \frac{3x}{r^5}(x\hat{x} + y\hat{y} + z\hat{z}\right] -$$

$$\beta E_0\left[\frac{x\hat{x}+z\hat{z}}{r^5} - \frac{5z}{r^7}(x^2\hat{x} + y^2\hat{y} + xz\hat{z}\right] \quad (1.24)$$

and the quadrupole polarizability is given by:

$$\beta = g_q R^5 \quad (1.25)$$

with

$$g_q = \frac{\varepsilon_i - \varepsilon_m}{\varepsilon_i + 3/2\varepsilon_m} \quad (1.26)$$

The presence of a factor 3/2 at the denominator of eq. (1.26) instead of the factor 2 present in eq. (1.16) derives from the exponents in the radial solutions to Laplace's equation, that are the factors r^l and $r^{-(l+1)}$. In the cases of dipole excitation, we have l=1, and the magnitude of the ratio of the exponents is (l+1)/l=2, while for quadrupole excitation it becomes (l+1)/l=3/2. Following the same derivation, the quasistatic expressions including the dipole and the quadrupole contributions for the extinction and Rayleigh scattering efficiencies are:

$$Q_{ext} = 4xIm\left[g_d + \frac{x^2}{12}g_q + \frac{x^2}{30}(\varepsilon_i - 1)\right] \quad (1.27)$$

$$Q_{sca} = \frac{8}{3}x^4\left\{|g_d|^2 + \frac{x^4}{240}|g_q|^2 + \frac{x^4}{900}|\varepsilon_i - 1|^2\right\} \quad (1.28)$$

1.3 CHEMICAL PROPERTIES

The high surface to volume ratio deriving from the reduced size is the leading parameter in the description of the chemical behaviour of metal nanoparticles. This consideration is due to the fact that surface atoms

often show the presence of unsaturation or dangling bonds and as result, higher chemical reactivity **[4]**. In general, noble metals such as gold and silver are inert and as a consequence, metal nanoparticles are stable in ordinary condition **[30]**. For this reason, laser prepared noble metal nanoparticles present pure surface and this characteristic is of huge importance for applications such catalysis, where surface plays a fundamental role. Indeed, necessary condition for a catalytic process is the absorption of reactants on the catalyst, and this happens at surface sites, lattice defects and corners or edge of crystallites. It is straightforward that dimension of the particles is relevant for the reactivity, since the decrease of the dimension leads to an increase of surface sites **[31]**. Moreover, surface atoms of small particles are dynamically active with the possibility of surface reconstruction phenomena **[32]**. It has been found that the activity of tetrahedral shaped Pt nanoparticles, used for catalyzing electron-transfer reaction, decreases during the course of the reaction as a result of morphological changes toward a spherical shape, which present the most stable surface **[33]**.

If nanoparticles are used in homogeneous catalysis, there is the need to protect their surface with a stabilizer, usually a polymer like PVP **[34]**, in order to prevent aggregation phenomena and to allow their recycle, but it has been demonstrated that the presence of capping decreases the catalytic activity since surface sites are occupied by the capping molecules **[35]**.

A role of interest is covered by palladium since it is an excellent hydrogenation catalyst but it catalyzes as well the formation of a large

variety of C-C bonds **[36-37]**. Gold nanoparticles present excellent catalytic properties too, and have been used to catalyze the oxidation of CO to CO_2 **[38-41]**, and other reactions **[42]**.

Also less noble metals clusters, like iron nanoparticles, have found application in the catalysis field **[43]**.

Among metal oxides, TiO_2 nanoparticles are attracting several attentions for their unique photo-properties **[44]**. The peculiar electron transport of these nanoparticles can be used for different purposes such as water purification **[45-48]**, bactericidal coatings **[48-49]** and hydrogen production **[50]**.

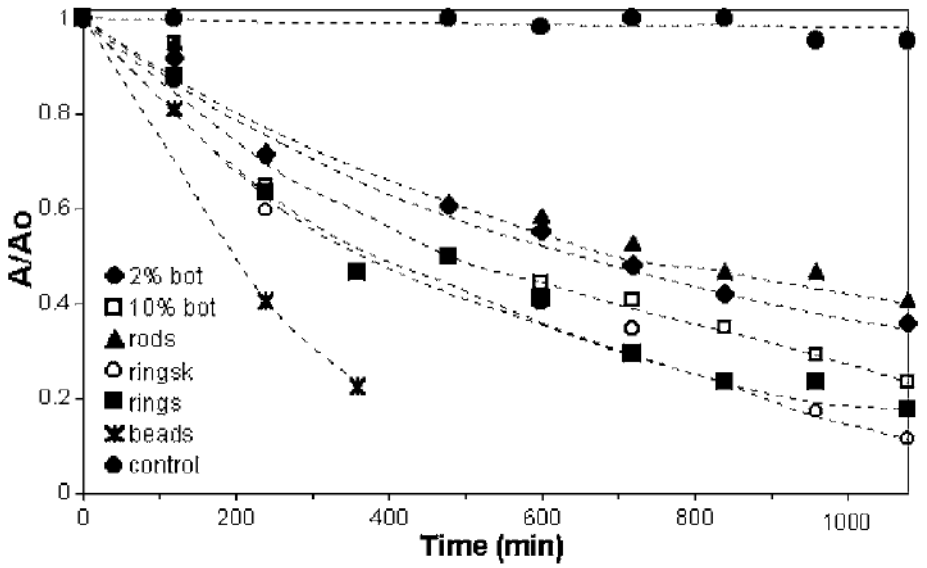

Figure 1.5 Photocatalytic degradation of 4-chlorophenol due to solar irradiation of TiO_2 nanoparticles deposited on different ceramic supports and on commercial PET bottles. From ref. **[47]**.

Metal nanoparticles present also interesting applications in the biological field. For example, silver nanoparticles show bactericidal properties as a result of their surface chemistry.

It is well known that silver exhibits strong toxicity to a wide range of microorganism **[51]** and for this reason silver based compounds have been used in many bactericidal systems **[52-53]**. Silver compounds have also been used in the medical field to treat burns and a variety of infections **[54].**

The effect is due to the fact that exposition to atmospheric oxygen leads to surface oxidation and subsequent releasing of Ag+ ions, which interfere with bacterial metabolism **[30]**.

The mechanism is not completely understood yet, but it has been proposed that ionic silver strongly interacts with thiol groups of vital enzymes and inactivate them **[55-56]** or that DNA loses its replication ability once the bacteria have been treated with silver ions **[54]**. In literature are reported also experimental evidences of structural changes in the cell membrane as well as the formation of small electron-dense granules formed by silver and sulphur **[54, 57]**.

However, recent studies have demonstrated that silver ions at concentration required to show germicidal effects, also damage fibroblasts to a significant degree **[58-59]**. For this reason, the application of silver nanoparticles to therapeutic purposes should be accurately targeted **[58-59]**.

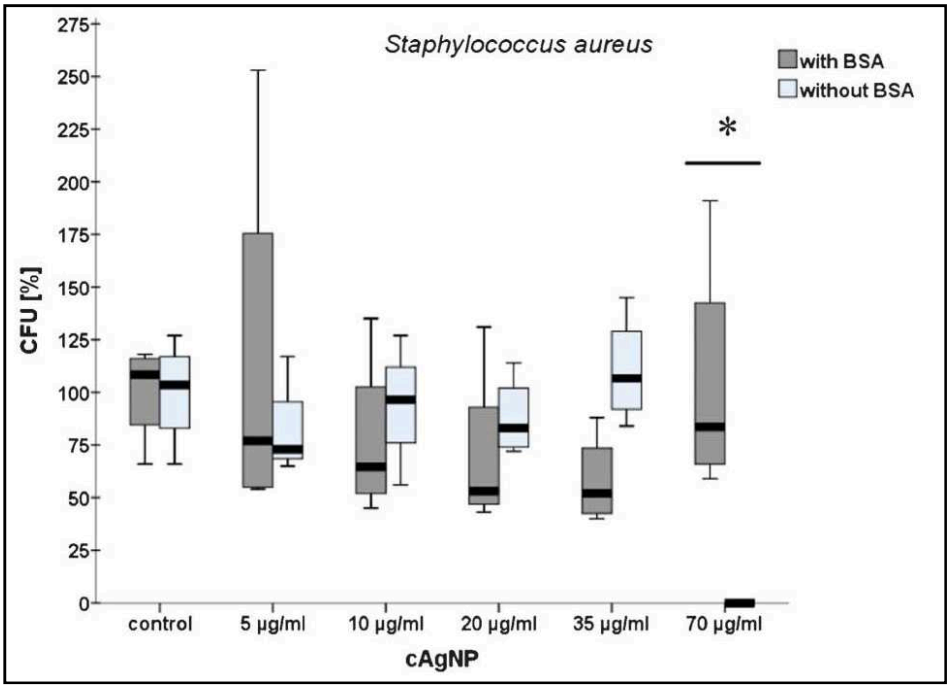

Figure 1.6 Bactericidal effects of laser-generated silver nanoparticles on Staphylococcus aureus after in vitro cultivation on Mueller-Hinton agar plates with or without BSA (1% w/v) over 24 h. From ref. **[58]**.

Gold and silver nanoparticles are also strongly reactive with sulphur and this characteristic is of particular interest for the functionalization of particle surface in biological studies **[60]**. Indeed, thiolated biomolecules can be directly bound on the surface of nanoparticles, like oligonucleotides **[61]**, peptides **[62]** or PEG **[63]**. Literature also reports the formation of gold nanoparticles-DNA aptamers used for the detection of thrombin **[64]**, platelet-derived growth factors **[65]** and cancerous cells **[66]**.

1.4 PHYSICAL PROPERTIES

The reduction of size and the subsequent increase in percentage of surface atoms is also responsible for the variation of physical properties from bulk to nanostructured particles. It has been demonstrated that phase stability of a material is size dependent **[67]**.

By simple thermodynamic considerations, the total free energy of a nanoparticle can be expressed as the sum of free energy contribution of the bulk and the surface **[67]**:

$$G_{nanoparticle} = G_{bulk} + G_{surface} \quad (1.29)$$

In a system such as a nanoparticle, which contains only few hundreds of atoms, a large fraction of them will be located on the surface. Surface atoms tend to be coordinatively unsaturated, so there is a large energy associated with the surface and the second term of eq. (1.29) becomes important for the overall phase stability **[4]**.

For example, in TiO_2 nanoparticles with dimension lower than 14 nm, anatase phase showed more stability than rutile, which is instead more stable in the case of bulk titanium dioxide **[68]**.

Another well known example of variation of physical properties with size is the decrease of melting temperature when passing from bulk to nanoclusters, with the value of the temperature depending on the size, shape and composition of the nanostructure. This phenomenon can be understood considering that liquid phase always shows lower surface energy with respect to the solid phase, where atoms are constrained by rigid bonding geometries. During the passage to the dynamic fluid phase,

the movement of surface atoms promotes the minimizing of the surface area and unfavorable surface interactions. Thus, the melting phenomenon reduces surface energy and stabilizes the liquid phase. Since at reduced dimensions the contribution of surface energy increases, the melting point shows considerable reductions **[4]**.

The estimation of the melting point can be obtained by the following relationship **[69]**:

$$T_m = T_b - \frac{M}{R} \tag{1.30}$$

Where T_m is the melting temperature of the nanoparticle, T_b is the melting point of the bulk metal, R is the radius of the nanoparticle and M is a constant which depend on the material in specified conditions.

Recently a model for calculating the reduction of melting temperature which also takes in account the shape factor has been proposed **[70]**.

The melting temperature of a nanoparticle of any shape is given by **[70]**:

$$T_m = T_b \left(1 - 6\alpha \frac{r}{D}\right) \tag{1.31}$$

Where α is the shape factor, r is the atomic radius and D is the diameter of the nanoparticle ($D=2R$).

The shape factor α is given by:

$$\alpha = \frac{S'}{S} \tag{1.32}$$

where S' is the surface of a particles of any shape which presents the same volume of a spherical particle of surface S.

Qualitatively, this can be explained considering that since melting starts at the surface, a larger surface will favour this process, and the melting point will present a lower value **[71-72]**.

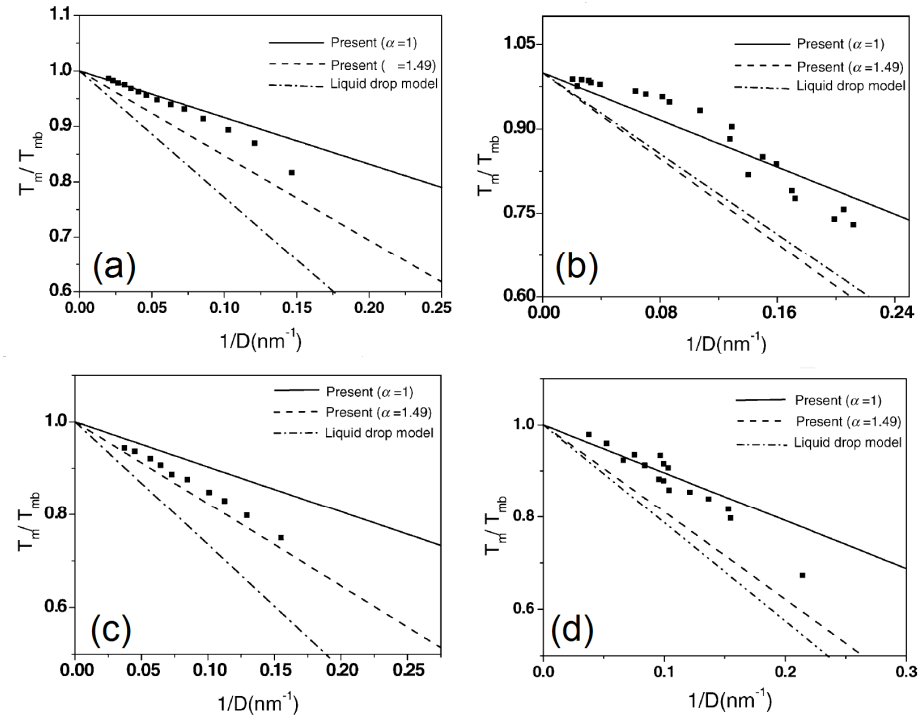

Figure 1.7 Calculated variation of the melting temperature as a function of the inverse radius for (a) Sn (b) Pb (c) In (d) Bi nanoparticles. The symbols (■) represent experimental values from ref. **[70]**.

When nanoparticles reach the size of few nanometers, which is smaller than the de Broglie wavelength of electrons at the Fermi energy for most metals, quantum effects appear in nanoparticles **[73]** and this leads to variations of the conductivity from the bulk behaviour.

Indeed, once the band electronic level turns into discrete electronic level, the motion of electrons does not obey the Ohm's law which instead rules bulk metals **[4]**.

To transfer an electron to a nanoparticle it is necessary to give to the system an energy called charge energy:

$$E_C = \frac{e^2}{2C} \tag{1.33}$$

where e is the charge of an electron and C the capacitance of the nanoparticle.

For a nanocluster surrounded by a medium with dielectric constant ε, the capacitance of the nanoparticle depends on its size:

$$C(R) = 4\pi\varepsilon\varepsilon_0 R \tag{1.34}$$

where R is the radius of the nanoparticles.

From eq. (1.33) and (1.34) it is clearly visible that high amount of energy required to add a single charge to a metal nanoparticle because capacitance is very low as it decreases with the decreasing radius. Qualitatively this can be explained considering that a charge carrier is no longer solvated in an effectively infinite medium **[4]**.

To produce single-electron tunneling processes, the thermal energy of the particle must be much lower than the coulomb energy in order to keep the electron in the particle:

$$k_B T \ll E_C \tag{1.35}$$

where k_B is the Boltzmann constant and T is the temperature of the system.

Otherwise the electron will be able to pass the nanoparticle by thermal excitation.

The current-voltage diagram for an ideal quantum dot will not show current till the potential reaches the value:

$$U_{coulomb} = \pm e/(2C) \tag{1.36}$$

And then an electron can be transferred. The charging of the nanocrystal occurs in increments of single electrons, giving rise to staircase with equally spaced steps in the I–V spectrum **[74]**.

Since for each step the charge transport is blocked till the overcoming of the Coulomb potential, this phenomenon is called Coulomb blockade.

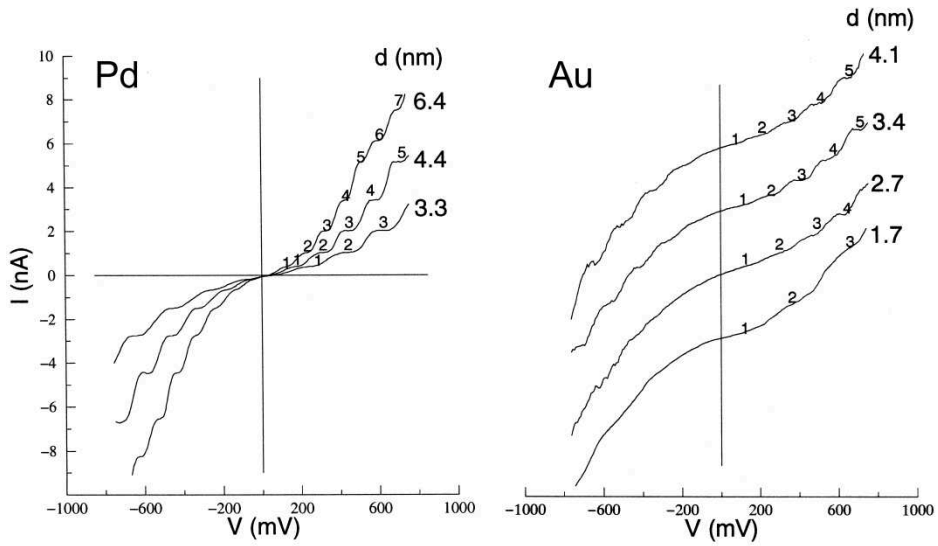

Figure 1.8 Current-Voltage diagrams of isolated Pd and Au nanoclusters of different sizes showing the Coulomb staircase effect. From ref. **[74]**.

REFERENCES

[1] J. Turkevich, P.C. Stevenson, J. Hillier*, Discuss. Faraday Soc.*, 1951, **11**, 55-75

[2] Z.S. Pillai, P.V. Kamat, *J. Phys. Chem. B,* 2004, **108**, 945-951

[3] G. Schmid, in "Nanoscale Materials in Chemistry", K.J. Klabunde, R.M. Richards (Eds.), Wiley: New York, 2009, p. 19

[4] C. Burda, X. Chen, R. Narayanan, M.A. El-Sayed, *Chem. Rev.*, 2005, **105**, 1025-1102

[5] L.M. Liz-Marzan, *Mater. Today*, 2004, **7**, 26-31

[6] M.C. Daniel, D. Astruc, *Chem. Rev.,* 2004**, 104***,* 293-346

[7] http://www.britishmuseum.org/explore/highlights/highlight_objects/pe_mla/t/the_lycurgus_cup.aspx

[8] C.P. Poole Jr., F.J. Owens, "Introduction to Nanotechnology", Wiley: New York, 2003, p. 72

[9] M. Faraday, *Phil. Trans. R. Soc. London*, 1857, **147**, 145-181

[10] C. Kittel, "Introduction to Solid State Physics", Wiley: New York, 1996.

[11] G. Mie, *Ann. Phys.*, 1908, **25**, 377–445

[12] K.L. Kelly, E. Coronado, L.L. Zhao, G.C. Schatz, *J. Phys. Chem. B*, 2003, **107**, 668-677

[13] R. Gans, *Ann. Phys.*, 1912, **37**, 881–900

[14] U. Kreibig, M. Vollmer, "Optical Properties of Metal Clusters" Springer Series in Materials Science 25, Springer: Berlin, 1995.

[15] U. Kreibig, in: R.E. Hummel, P. Wissmann (Eds.), "Handbook of Optical Properties; Vol. II: Optics of Small Particles,Interfaces and Surfaces", CRC Press:Boca Raton, 1997, pp 145-190

[16] J. Pérez-Juste, I. Pastoriza-Santos, L.M. Liz-Marzán, P. Mulvaney, *Coord. Chem. Rev.*, 2005, **249**, 1870–1901

[17] H.C. van der Hulst, "Light Scattering by Small Particles", John Wiley and Sons: New York, 1957

[18] M. Kerker, "The Scattering of Light and Other Electromagnetic Radiation", Academic Press: New York, 1969

[19] L. Genzel, T.P. Martin, U. Kreibig, *Z. Phys. B*, 1975, **21**, 339-346.

[20] C.F. Bohren, D.F. Huffman, "Absorption and Scattering of Light by Small Particles", Wiley: New York, 1983

[21] S. Link, M.A. El-Sayed, *Annu. Rev. Phys. Chem.*, 2003, **54**, 331–366

[22] U. Kreibig, U. Genzel, *Surf. Sci.*, 1985, **156**, 678-700

[23] U. Kreibig, C. von Fragstein, *Z. Phys.*, 1969, **224**, 307-323

[24] U. Kreibig, *Z. Phys.*, 1970, **234**, 307-318

[25] N.W. Ashcroft, N.D. Mermin ND., "Solid State Physics", Saunders College: Philadelphia, 1976

[26] M.M. Alvarez, J.T. Khoury, T.G. Schaaff, M.N. Shafigullin, I. Vezmar, R.L. Whetten, *J. Phys. Chem. B,* 1997, **101**, 3706-3712

[27] T.G. Schaaff, M.N. Shafigullin, J.T. Khoury, I. Vezmar, R.L. Whetten, W.G. Cullen, P.N. First, C. Gutiérrez-Wing, J. Ascensio, M.J. Jose-Yacamán, *J. Phys. Chem. B*, 1997, **101**, 7885-7891

[28] M.J. Hostetler, J.E. Wingate, C.J. Zhong, J.E. Harris, R.W. Vachet, M.R. Clark, J.D. Londono, S.J. Green, J.J. Stokes, G.D. Wignall, G.L.

Glish, M.D. Porter, N.D. Evans, R.W. Murray, *Langmuir*, 1998, **14**, 17-30

[29] S. Link, M.A. El-Sayed, *J. Phys. Chem. B*, 1999, **103**, 4212-4217

[30] N.N. Greenwood, A. Earnshaw, "Chemistry of the Elements", Elsevier Science: Oxford, 1997

[31] A. Wieckowski, E.R. Savinova, C.G. Vayenas (Eds.), "Catalysis and Electrocatalysis at Nanoparticle Surfaces", Marcel Dekker: New York, **2003**, p. 970

[32] R. Narayanan, M.A. El-Sayed, *J. Phys. Chem. B.*, 2004, **108**, 5726–5733

[33] R. Narayanan, M.A. El-Sayed, *J. Am. Chem. Soc.*, 2004, **126**, 7194–7195

[34] N. Toshima in "Fine Particles Sciences and Technology – From Micro - to New Particles", E. Pellizzetti (Ed.), Kluwer : Dordrecht ,1996, pp. 371 – 383

[35] Y. Li, M.A. El-Sayed, *J. Phys. Chem. B*, 2001, **105**, 8938-8943

[36] D. Astruc in "Nanoparticles and Catalysis", D. Astruc (Ed.), Wiley: New York, 2008, pp. 1-48

[37] D. Astruc, *Inorg. Chem.*, 2007, **46**, 1884-1894

[38] M. Haruta, T. Kobayashi, H. Sano, N. Yamada, *Chem. Lett.*, 1987**, 2**, 405-408

[39] M. Haruta, N. Yamada, T. Kobayashi, S. Iijima, *J. Catal.*, 1989**, 115**, 301-309

[40] M. Haruta, S. Tsuboda,T. Kobayashi, H. Kagehiama, M.J. Genet, B. Demon, *J. Catal.*, 1993, **144**, 175-192

[41] M. Haruta, *CATTECH*, 2002, **6**, 102-115

[42] D.T. Thompson, *Nano Today*, 2007, **2**, 40–43

[43] J. G. De Vries, *Dalton Trans.*, 2006, **3**, 421-429

[44] J.A. Anta, *Curr. Opin. Colloid Interface Sci.*, 2012, **17**, 124-131

[45] C. Wei, W.Y. Lin, Z. Zainal, N.E. Williams, K. Zhu, A.P. Kruzic, R.L. Smith, K. Rajeshwar, *Environ. Sci. Technol.*, 1994, **28**, 934-938

[46] Y. Chen, K. Wang, L. Lou, *J. Photochem. Photobiol. A*, 2004, **163**, 281–287

[47] J.M. Meichtry, H,J. Lin, L. de la Fuente, I.K. Levy, E.A. Gautier, M.A. Blesa, M.I. Litter, *J. Sol. Energy Eng.,* 2007, **129**, 119-126

[48] P.C. Maness,S. Smolinski, D.M. Blake, Z. Huang, E.J. Wolfrum, W.A. Jacoby, *Appl. Environ. Microbiol.*, 1999, **65**, 4094–4098

[49] G. Fu, P.S. Vary, C.T. Lin, *J. Phys. Chem. B*, 2005**, 109***,* 8889-8898

[50] M. Ni, M.K.H. Leung, D.Y.C. Leung, K. Sumathy, *Renew. Sustain. Energ. Rev.*, 2007, **11**, 401–425

[51] S.Y. Liau, D.C. Read, W.J. Pugh, J.R. Furr, A.D. Russell, *Lett. Appl. Microbiol.*, 1997*,* **25**, 279–283

[52] K. Nomiya, A. Yoshizawa, K. Tsukagoshi, N.C. Kasuga, S. Hirakawa, J. Watanabe, *J. Inorg. Biochem.*, 2004, **98**, 46–60

[53] A. Gupta, S. Silver, *Nat. Biotechnol.* 1998, **16,** 888-890

[54] Q. L. Feng, J. Wu, G.Q. Chen, F.Z. Cui, T.N. Kim, J.O. Kim, *J. Biomed. Mater. Res.*, 2000, **52**, 662–668

[55] Y. Matsumura, K. Yoshikata, S. Kunisaki, T. Tsuchido, *Appl. Environ. Microbiol.*, 2003, **69**, 4278–81

[56] A. Gupta, M. Maynes, S. Silver, *Appl. Environ.Microbiol.*, 1998, **64** 5042–5045

[57] L. Nover, K.D. Scharf, D. Neumann, *Mol. Cell. Biol.*, 1983, **3**, 1648–55

[58] S. Grade, J. Eberhard, A. Neumeister, P. Wagener, A. Winkel, M. Stiesch, S. Barcikowski, *RSC Adv.*, 2012, **2**, 7190-7196

[59] S. Grade, J. Eberhard, P. Wagener, A. Winkel, C.L. Sajti, S. Barcikowski, M. Stiesch, *Adv. Eng. Mater.*, 2012, **14**, B231–B239

[60] R.K. DeLong, C.M. Reynolds, Y. Malcolm, A. Schaeffer, T. Severs, A. Wanekaya, *Nanotech. Sci. Appl.*, 2010, **3**, 53–63

[61] W. Chen, A. Bian, A. Agarwal, L. Liu, H. Shen, L. Wang, C. Xu, N.A. Kotov, *Nano Lett.*, 2009, **9**, 2153–2159

[62] R. Lévy, Z. Wang, L. Duchesne, R.C. Doty, A.I. Cooper, M. Brust, D.G. Fernig, *Chem. Bio Chem.*, 2006, **7**, 592–594

[63] H. Otsuka H, Y. Nagasaki, K. Kataoka, *Adv. Drug Deliv. Rev.*, 2003, **55**, 403–419

[64] H. Cho, B.R. Baker, S. Wachsmann-Hogiu, C.V. Pagba, T.A. Laurence, S.M. Lane, L.P. Lee, J.B.H. Tok, *Nano Lett.*, 2008, **8**, 4386–4390

[65] C.C. Huang, Y.F. Huang, Z. Cao, W. Tan, H.T. Chang, *Anal. Chem.*, 2005, **77**, 5735–5741

[66] C.D. Medley, J.E. Smith, Z. Tang, Y. Wu, S. Bamrungsap, W. Tan, *Anal Chem.*, 2008, **80**, 1067–1072

[67] V.H. Grassian *J. Phys. Chem. C*, 2008, **112**, 18303-18313

[68] H.Z. Zhang, J.F. Banfield, *J. Mater. Chem.*, 1998, ***8***, 2073-2706

[69] P. Pawlow, *Z. Phys. Chem.*, 1909, **65**,1-35

[70] W.H. Qi, M.P. Wang, *Mater. Chem. Phys.*, 2004, **88**, 280–284

[71] P.R. Couchman, W.A. Jesser, *Nature*, 1977, **269**, 481-483

[72] F. Ercolessi, W. Andreoni, E. Tosatti, *Phys. Rev. Lett.* 1991, **66**, 911-914

[73] M.J. Madou, **"**Fundamentals of Microfabrication and Nanotechnology, (Vol. 1) : Solid-State Physics, Fluidics, and Analytical Techniques in Micro- and Nanotechnology", CRC Press: Boca Raton, 2011, p. 365

[74] P. John Thomas, G.U. Kulkarni, C.N.R. Rao, *Chem. Phys. Lett.*, 2000, **321**, 163–168

CHAPTER 2: PULSED LASER ABLATION IN LIQUID

2.1 INTRODUCTION

The term laser ablation refers to the removal of material from a solid target by incidence of light. The laser pulse presents a penetration depth which depends on the laser wavelength and the refraction index of the material, typically with values around 10 nm. The expulsion of material from the target is due to different mechanisms **[1]**.

At high energy flux, the ejected matter is typically converted into plasma, formed by atoms, molecules, ions, electrons, clusters and particulates in a physical state characterized by high temperature, high pressure and high density **[2-3]**.

The difference of pressure between the plasma and the surrounding environment leads to the nearly adiabatic expansion of the plasma **[4]** and in particular conditions, materials from the target can condense and form nanostructures **[5]**.

This process has been used for different purposes, such the pulsed laser deposition (PLD), where laser is used to vaporize material from a target in vacuum or in a carrier gas that is then deposited on a suitable substrate to obtain thin films, with lower cost and higher purity with respect to other techniques **[6-7]**.

The removal of material due to ablation can be also used for surface cleaning, with applications both in technological field than in preservation and restoration of artworks **[8]**. It is common to make difference between "dry laser cleaning", in which material is directly removed by absorption of light and "steam laser cleaning" obtained by submerging the substrate in a liquid environment. The substrate is then covered by a thin liquid layer which, irradiated by light, undergoes violent boiling, and the pressure generates from the explosion of bubbles removes the material **[8]**.

The mechanism of laser ablation is also the base of different characterization techniques, such as MALDI (Matrix Assisted Laser Desorption/Ionization) mass spectrometry **[9]** or LIBS (Laser Induced Breakdown Spectroscopy) **[10]**.

In the field of nanomaterials synthesis, laser ablation in liquid environment is of particular interest for several reasons. First of all, it can be considered an almost universal preparation technique, since the variation of the target material and the surrounding liquid can lead to the formation of a large variety of products, and size and shape of obtained nanocrystals can be tuned by the variation of laser parameters such as fluence and laser wavelength. Moreover, laser ablation in liquid leads to clean surface nanoparticles, an important requirement when these nanostructures are employed in the production of nanocomposites. Moreover, laser ablation in liquid can be considered as environmentally friendly and cheap with respect to other production techniques. Indeed, it

does not need the use of dangerous chemicals or the use of expensive and energy consuming pressure or temperature apparatuses.

2.2 THE MECHANISM OF LASER ABLATION IN LIQUID

2.2a Plasma Formation

Conventionally, the phenomenon of laser ablation starts when light hits the target. The energy coming from the laser is absorbed by the material and couples with electrons in valence and conduction bands. If the energy is higher than a certain threshold, which depends on the material itself, breaking of electron bonds is possible with subsequent removing of material **[11]**. Optical energy is also redistributed by carrier-carrier, carrier-phonon and phonon-phonon interactions. The energy relaxation time presents the same order of time required to approach thermal energy distributions, which are Fermi-Dirac for electrons and Bose-Einstein for phonons. For metal and semiconductors, energy thermalisation times are of the order of 10^{-12} to 10^{-11} seconds **[12]**.

When using femtosecond laser pulses, common values of laser irradiance (10^{13} W/cm^2) are higher than ionization threshold, that thus takes place before the expulsion of the material **[1]**. This is a non-equilibrium process, since the pulse duration is shorter than relaxation phenomena and the lattice remains “cold” **[13]**.

It is also possible that electrons with sufficient kinetic energy will move away from the solid before starting the thermalisation of the lattice **[14]**.
A resulting charge separation is then established and ions will be ejected from the target, either by Coulomb explosion **[15]** or by electrostatic ablation **[16]**.
In the case of fs ablation, the amount of ablated material depends only on the penetration depth and the diameter of the laser beam and the crater left by the beam present well defined borders **[17-18]**.
On the other way, when nanosecond lasers are used, the pulse duration overpasses the time for reaching the system thermalisation through electron collisions and thermal conduction phenomena. Ions and electrons are accelerated by mutual collisions inside the plasma, and its temperature reaches the equilibrium **[19-21]**.
The main mechanism of ablation is thermal ablation, which is direct sublimation or melting followed by evaporation, boiling or phase explosion, but also spallation **[19,22-23]**.
Confirmations of thermal ablation during laser processes have been obtained by shadowgraph images that show the ejection of metal droplets from the target in the case of nanosecond pulses **[24-25]** and millisecond pulse width **[26]**.
In the case of picosecond laser pulses, a complete understanding of involved phenomena is not clear yet and the ablation mechanism depends on the thermal characteristic of the metal **[27]**. Different models have been proposed to explain the behaviour under low fluence **[28]** and high fluence **[29]** regimes.

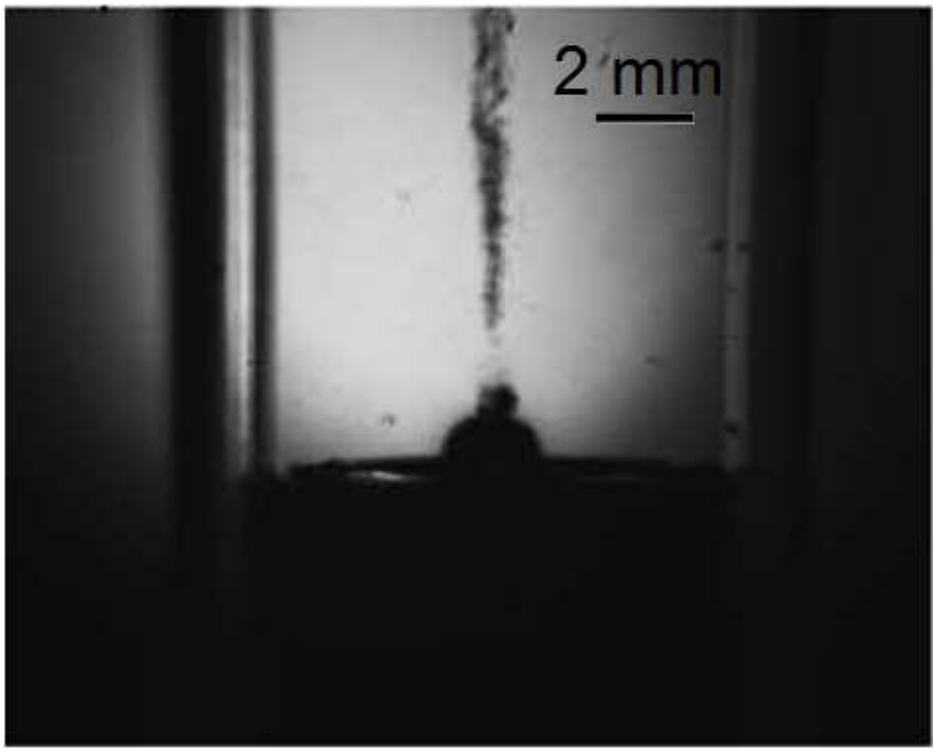

Figure 2.1 Shadowgraph image of laser ablation of an Ag target in water at a laser fluence of 36 J/cm^2 and a delay time of 10 μs showing the ejection of metal nanodroplets from the target. From ref. **[24]**.

Independently of the pulse width, when the irradiance of the laser exceeds a certain threshold, the "breakdown" of matter happens, that is the generation of plasma **[2,3,30]** that is sustained mainly by ionization/recombination and excitation/de-excitation mechanisms due to electron collisions **[1]**.

Multiphoton ionization is the simultaneous absorption of different photons and is the process responsible for atoms ionization and generation of free electrons ("seed electrons") that are then involved in avalanche ionization by collisions with the neutral species **[1,30]**. It has been hypothesised also the possibility of Coulomb explosion phenomena, which consist in the ejection of ions if removed electrons are not replaced in picosecond timescales by other from the surrounding solid. This lead to a surface charge and ions in the lattice undergo repulsion effects. If repulsion overcomes the bonding energy, ions can be expelled from the target with kinetic energies in the order of 10^2 eV. Due to electrostatic nature, this process is not common for conductors **[31]** but is more probable during ablation of dielectrics and semiconductors **[32]**.There is no marked separation between different regimes discussed above, thus a quantitative description of the breakdown process is very complex **[1]**.

In the case of fs lasers, it should be considered that the pulse is so short that any significant movement of atoms from the lattice happens after the end of the pulse **[4]**, while for longer pulses, shielding effects of the plasma can happen and most energy will not reach the target but will be absorbed by ionization processes and Inverse Bremsstrahlung or reflected **[33-34]**. Inverse Bremsstrahlung involves absorption of photons by free electrons accelerated during collisions with neutral or ionized species. The importance of collisions of electron with neutral species is lower than electron-ion collisions, but assumes importance in the initial phase of the plume when ionization level is still low **[4]**.

For plasma induced by IR lasers, as laser light at 1064 nm, absorption by Inverse Bremsstrahlung is predominant and ionization breakdown may occur even at intensities near the ablation threshold **[35]**. On the other way, photon absorption by photoionization processes takes places when using visible and UV laser light. It has been demonstrated that during UV ablation of metal targets with irradiation intensities of 0.1-1 GW/cm^2 the plume can reach temperatures of a few eV and ionization degrees higher than 0.1. Since these high temperatures cannot be reached by Inverse Bremsstrahlung processes, it means that direct photoionization phenomena play a dominant role **[35-36]**.
On the other way, Inverse Bremsstrahlung and direct single-photon processes gives the kinetic energy for plasma expansion, which can be considered isothermal in the initial part of the process, since temperature is kept constant by the absorption of radiation **[37]**.

2.2b Plasma Expansion

After the end of the pulse, the vaporised material exists as a thick layer of 10-100 μm of a dense, partly ionized gas propagating supersonically away from the target in a three dimensional adiabatic expansion, often called "plume" **[4]**. This is due to the accumulation of thermal energy of the excited species present in the initial phase that is then converted in kinetic energy by plasma species. Theoretical treatments consider that the expansion is also isentropic, since there is no heat conduction

between different plume parts, due to high pressure and temperature conditions **[4]**.

The liquid environment presents a strong confinement effect limiting the expansion rate. Results of this effect is a very high number density inside the plasma (with $N>10^{19}$cm^{-3}), coupled with a fast decrease of the temperature due to the prevalence of recombination phenomena, and a persistence of the plume to a few hundred nanoseconds **[1]**, which is a lifetime 10 time shorter than that of plasma in air **[38]**.

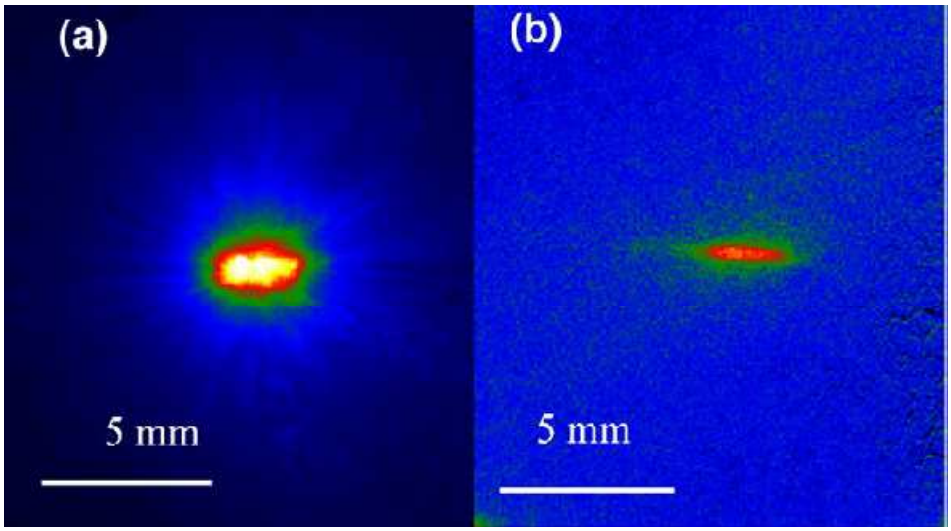

Figure 2.2 Laser-induced plasma emission imaging in air (a) and bulk water (b) at the same experimental conditions (λ=532 nm, E=300 mJ, gate window=3 μs). From ref. **[39]**.

The intense thermal diffusion of the species inside the plasma can lead to collisions, aggregations (and condensation), formation of new molecules or nucleation phenomena. Usually smaller particles, with dimension of

nanometers, are formed during expansion of the plasma as a consequence of condensation of atoms in vapour phase, while bigger nanoparticles, with dimension of micrometers, probably derive from direct expulsion from the solid target **[40]**.

It should be noticed that, when working in a liquid environment, even if at the initial moments of ablation the plasma presents high pressure, the expansion is globally controlled by the interaction between ablated species and the background environment. Practically, plume expansion continues till the inner pressure is equal to surrounding environment pressure **[4]**.

Most common models describe a splitting of the plasma in two components with different speeds. During expansion, the component at higher speed moves through the ablation environment as if expanding in vacuum, while the slower component moves as a piston in a gas. The slower component pushes a layer of liquid far from the target, releasing an internal and external shock wave. The formation of the shockwave does not happen in a harsh way, but it is the result of increasing hydrodynamic interactions between the plasma and the fluid **[4]**.

The high pressure in the plasma is usually attributed to two contributions, which are the adiabatic expansion of the plasma itself under the confinement of the liquid and the extra pressure increase deriving from the shock wave. A series of experimental technique to measure the pressure by characterization of the shock wave and a theoretical model to describe the laser induced pressure generation have been developed by Fabbro and coworkers **[41-48]**. The pressure inside the plasma has been

also measured by recording the acoustic wave in water induced by the plasma **[49-50]**.

Following the Fabbro analytical model, **[41-48]** the maximum pressure expressed in GPa generated by the laser induced plasma in water is given by:

$$P = 0.01\sqrt{\frac{\alpha}{\alpha+3} Z I_0} \quad (2.1)$$

where α is the fraction of internal energy devoted to thermal energy (usually α~0.25), I_0 the incident power intensity expressed in g/(cm^2·s), and Z the reduced shock impedance between target and the confining water expressed in GW/cm^2.

Z is defined by the relation:

$$\frac{2}{Z} = \frac{1}{Z_{water}} + \frac{1}{Z_{target}} \quad (2.2)$$

where Z_{water} and Z_{target} are the shock impedances of the water and the target, respectively.

Pressure in the order of GPa are reported in literature, as a value of 5.5 GPa obtained with pulse duration of about 50 nm with a wavelength of 1064 nm and a power density of 10 GW/cm^2 **[43-46]**, or a value of 2-2.5 GPa measured when a 0.308 μm XeCl excimer laser with pulse duration of 50 ns and power of 1-2 GW/cm^2 is used to ablate an Al target in water **[46]**. It has also been demonstrated a dependence of the pressure on the laser parameters like wavelength and pulse duration. Indeed, it is reported that laser pulses of 3 ns generated a plasma-induced pressure of 10 GPa, while for longer pulse (30 ns) the plasma pressure is only 5 GPa **[47]**.

It should be noted that the relationship between temperature and pressure in the laser induced plasma is not completely consistent with the predictions from the ideal gas state equation, since the formation of the laser induced plasma is a far from thermodynamic equilibrium process and the plasma cannot be considered as an ideal gas. Indeed, the pressure estimated by the equation:

$$P = \frac{nN_A k_B T}{V} \tag{2.3}$$

where n is the gas density, N_A is the Avogadro constant, k_B the Boltzmann constant and V the gas volume, is much lower than values of measured pressure.

Temperature of the plasma can be measured by optical emission spectroscopy of the ablated species **[38,51-53]**.

In a plasma plume in liquid, emission spectra appear dominated by a black body-like broad continuum, due to radiative recombination and, more limitedly, to Bremsstrahlung emission **[54]** which can be treated as a Planck-like distribution to determine the temperature **[55]**. Consistently with the high ionization degree of this kind of plasma, also few broadened lines due to transitions between low-lying energy levels can be observed **[39]**, which allow the calculation of temperature by the Boltzmann plot method **[56-57]**.

The density of species in the laser-induced plasma can be estimated by measurements of the expansion volume of the plume, measured from the images of the light emitting region, and the calculation of the amount of the ablated species from the volume of the crater left on the surface of the target. Considering the plasma plume as a hemisphere with the diameter

of the FHWM intensity, the volume of the plasma plume has been estimated to be 9.9×10^{-7} cm^3 in the case of ablation of graphite in water **[38]**.

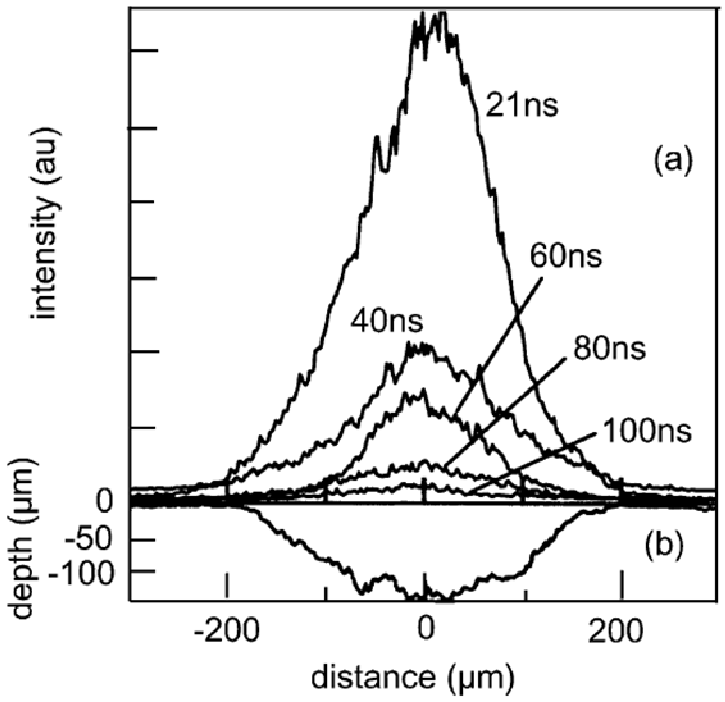

Figure 2.3 (a) Intensity distribution of the light emitting region and (b) the vertical sectional profile of the hole left at the target surface after 100 shots irradiation with 1064 nm Nd:YAG of graphite in water (pulse width 20 ns and fluence 10 J/cm^2). From ref. **[38]**.

In the same experiment it has been supposed that the crater on the target surface increases linearly with the number of laser pulse and the ablating volume due to a single laser pulse has been determined to be 7.4×10^{-8}

cm^3 **[38]**. From these values, the density of species in the plasma plume has been calculated to be 6.7×10^{21} cm^{-3}, that is higher than the plasma electron density estimated for a water–graphite system with similar irradiation conditions (10^{19}-10^{20} cm^{-3}) **[58]**, but lower than the number of atom density of a graphite solid target (10^{23} cm^{-3}) **[38]**.

Since part of the initial energy of the plume is used for the formation of the shockwave, the expansion can be considered adiabatic just for a short period of time. When the expansion stops, particles diffuse from the volume of the plume and undergo thermalisation.

The strong confinement of the plasma by the liquid medium deeply influences thermodynamic and kinetic properties of the plasma evolution, with a consequent formation of a complex reaction environment. Due to high temperature and pressure, several kinds of reactions can happen at the liquid-plasma interface. Apart from reactions at high temperature that involve species inside the plasma, there is also the possibility of target-liquid species interaction. Since high pressure and high temperature conditions lead to excitation and evaporation of molecules of the surrounding liquid at the interface, this induced plasma can mix with the plasma generated by the laser and form new species. Moreover, ablated species can be pushed far away from the target by high pressure, and reach the liquid where they react. Considering that these reactions involve both species from the solid target and from the liquid, these mechanisms offer the possibility for the formation of new species combining properly the target and the liquid **[40]**.

For example, iron oxides were prepared by laser ablation of an iron target in water **[59]** and CN nanocrystals were prepared from PLA of a pure graphite target in ammonia solution **[60]**.

Latest stage of the evolution of the plasma plume is the cooling down and condensation in the confining liquid. Part of the plume would condense and deposit back on the target due to the confined pressure from the liquid **[40]**. This effect has been used to develop a new technique of plasma deposition in liquid **[61-65]**.

Another part of the plasma plume will condense and disperse in the liquid phase, generating nanocrystals.

Shorter quenching times of ablation in liquid have several consequences on products obtained by laser ablation in liquid. First of all, the sudden quenching reduces the possibility of growing of crystals, leading in this way to the formation of smaller nanoparticles. For example, the use of lasers with pulses duration shorter than 20 ns allows obtaining particles with dimension in the order of nanometers **[40]**. Fast quenching times can also influence the characteristics of obtained structures, since it is possible to cool generated in metastable forms. For example, the intermediate transformation phase from graphite to cubic diamond has been observed during the synthesis of nanodiamonds by ablation of graphite in water **[66]**.

An extremely important feature of the laser ablation in water is the formation of a cavitation bubble. The laser-induced plasma at high temperature transfers a significant amount of its internal energy to the surrounding liquid, producing a layer of vapour around the plasma

volume. The layer of vapour grows into a cavitation bubble that expands and then collapses on a timescale on the order of hundreds microseconds, which is order of magnitudes longer than the plasma duration itself **[1,67-69]**. This topic will be widely discussed in section 3.6.

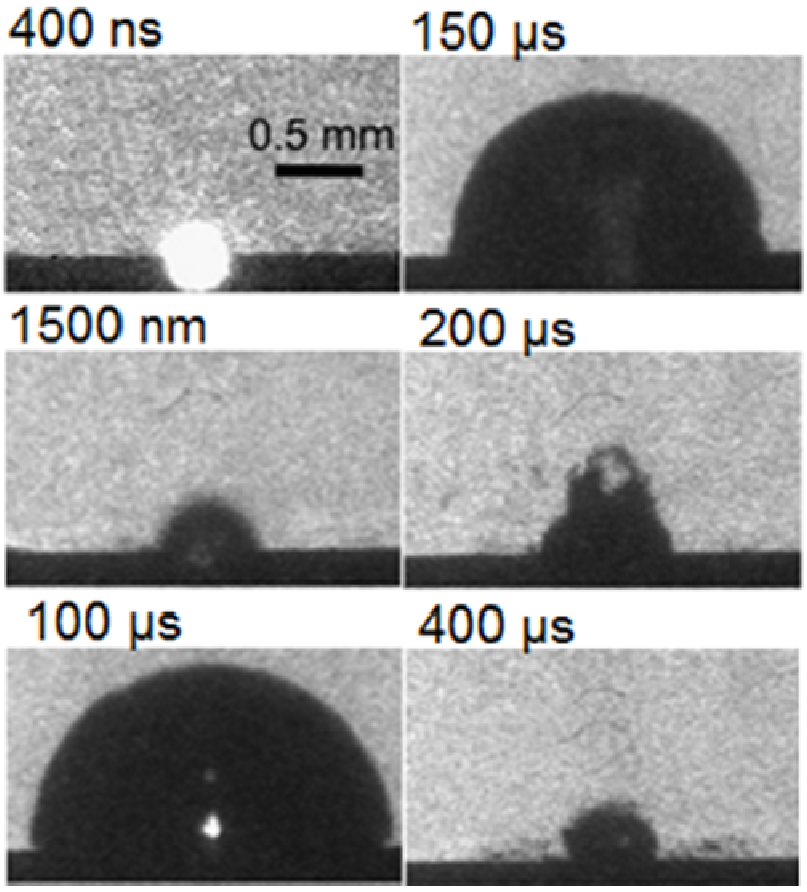

Figure 2.4 Shadowgraph of the cavitation bubble produced by laser irradiation of a Cu target in water, with pulse width of 90 ns and pulse energy of 1.7 mJ. From ref. **[70]**.

2.3 NANOCRYSTAL FORMATION BY LASER ABLATION IN LIQUID ENVIRONMENTS

Most common products of laser ablation in liquid, and in particular in water, are metal nanoparticles. When targets constituted by noble metals, silicon or carbon are irradiated, ablated products are usually pure elemental particles **[71]**, while the ablation of reactive metals in water leads to the formation of oxide or hydroxide nanoparticles **[59,72-74]**.

2.3a Metals

Great interest has been devoted to synthesis of metals since their application as catalyst. Ablation of Au and Ag targets in water by 510.5 nm Cu vapour with 20 ns pulse duration has led to the formation of nanodisks with diameters of 10-60 nm **[75]**. It has been demonstrated that the relatively mild regime of laser irradiation influences the shape and is then favorable to the disk shape formation, since the relatively high stability of these colloidal systems in the absence of surface agents **[75]**.
The formation of spherical nanoparticles is more common and literature reports the preparation of Au, Ag, Ti and Si by ablation in of Ag, Au, Ti and Si in various liquid environments **[76-78]**. Au and Pt have been synthesized with average sizes of 5-30 nm by Nd:YAG irradiation of metallic target in n-alkanes **[79-81]** and the formation of gold nanocrystals has been reported by femtosecond ablation of an Au target in aqueous solution of cyclodextrins as well **[82-84]**. Since these metals are easily oxidable in water, Ni and Co nanocrystals were prepared by

laser ablation of Ni and Co targets in flowing ethanol **[85]**. Different noble metal nanoparticles with diameters lower than 5 nm, have been synthesized by 532 nm Nd:YAG laser ablation of Au, Ag and Pt targets in aqueous solution of sodium dodecyl sulfate **[86-88]**. Literature reports also the formation of Ag nanoparticles by laser ablation of Ag in water, methanol and isopropanol, while Cu colloids were produced by ablation of CuO powders in 2-propanol **[24,89-90]**.

2.3b Oxides and Sulfides

Oxides nanocrystals can be prepared by ablation of an oxidable metal target in water as tin, which led to the formation of oxide nanocrystals with small dimensions if ablated in water or aqueous solution of sodium dodecyl sulfate **[91]**.

Oxide can be also prepared by ablation of an oxide target, like the case reported in literature for CeO_2 nanoparticles, obtained by Nd:YAG ablation of a CeO_2 target in water **[92]**.

Interesting results have been obtained with aluminum, since nanocrystals of aluminum hydroxides with triangular, rectangular and fibrous shapes have been fabricated by nanosecond ablation of an Al rod in water **[93]** and ultrafine aluminum oxide powders **[94]**.

Magnesium and zinc hydroxides nanoparticles have been produced as well by ablation of Mg and Zn plate target submerged in deionized water or aqueous solutions of sodium dodecyl sulfate **[95-96]**.

Of particular interest are results obtained in the case of ablation of sulfides, since it has been demonstrated the possibility to use laser ablation to produce innovative Inorganic Fullerene like structures **[97-98]**.

In particular, literature reports that the ablation of HfS_3 powders in tert-butyl disulfide allows the formation of Hf_2S layered nanostructures and quasi-spherical nanoparticles of HfS with size of 20-80 nm **[97]**.

Moreover, it has been demonstrated that the source of sulphur should be the target itself, since the ablation of MoS_2 target in water led to the production of Inorganic fullerene-like MoS_2 and spherical MoO_3 structures, and a detailed mechanism for the formation of these structure has been proposed **[98]**.

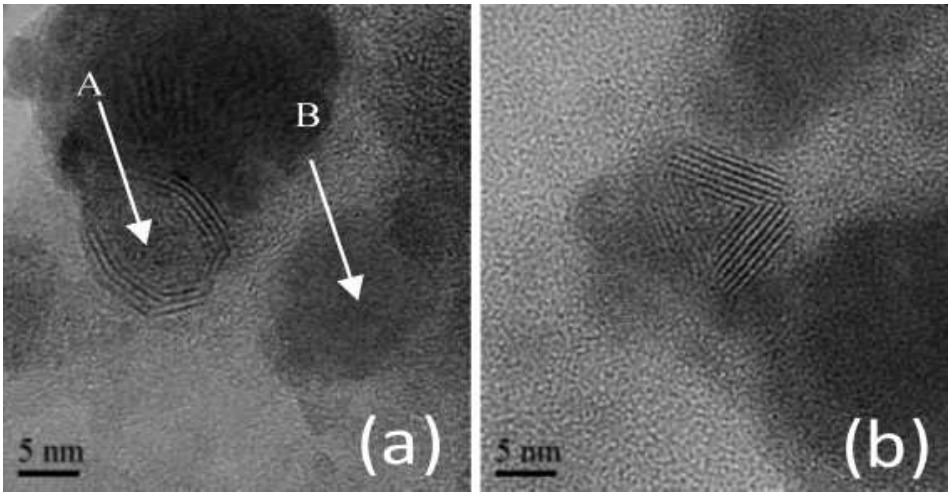

Figure 2.5 (a) TEM image of MoS2 (A) and MoO3 (B) IF-nanostructures, (b) TEM image of MoS2structures with different shape. From ref. **[98]**.

2.3c Product Control by Ablation Environment

As discussed in section 2.2b, the surrounding solution has a deep influence on nanoparticles formation and thus on their chemical nature, since inside the plasma, molecules of the liquid can react with target species. For example the ablation of a graphite target in water can lead to the synthesis of diamond **[99-100]**, while in ammonia it is possible to generate C_3N_4 **[101]**.

The species in the liquid can also affect the nucleation and growth of crystals. For example, during diamond nanocrystals synthesis, the H and OH ions from the solution can promote diamond growth by suppressing graphite sp^2 bonding **[102]**. It has also been reported that surface chemistry has an effect on the size distribution. This has been demonstrated adding different compounds (KCl, NaCl, NaOH and cyclodextrins) to water when ablating gold **[83]**. The size distribution of nanoparticles can be narrowed by using surfactant solutions of sodium dodecyl sulfate **[86-87]** or cyclodextrins **[84]**.

The control of the size due to the surfactant depends on a control of the reaction rate at the interface and on the stability of produced nanoparticles with effects varying on the nature of the charge on the particles surface and of the surfactant **[103]**. The high temperature of the reaction environment due to laser irradiation and to the presence of plasma can induce boiling, evaporation or excitation at the liquid-plasma interface.

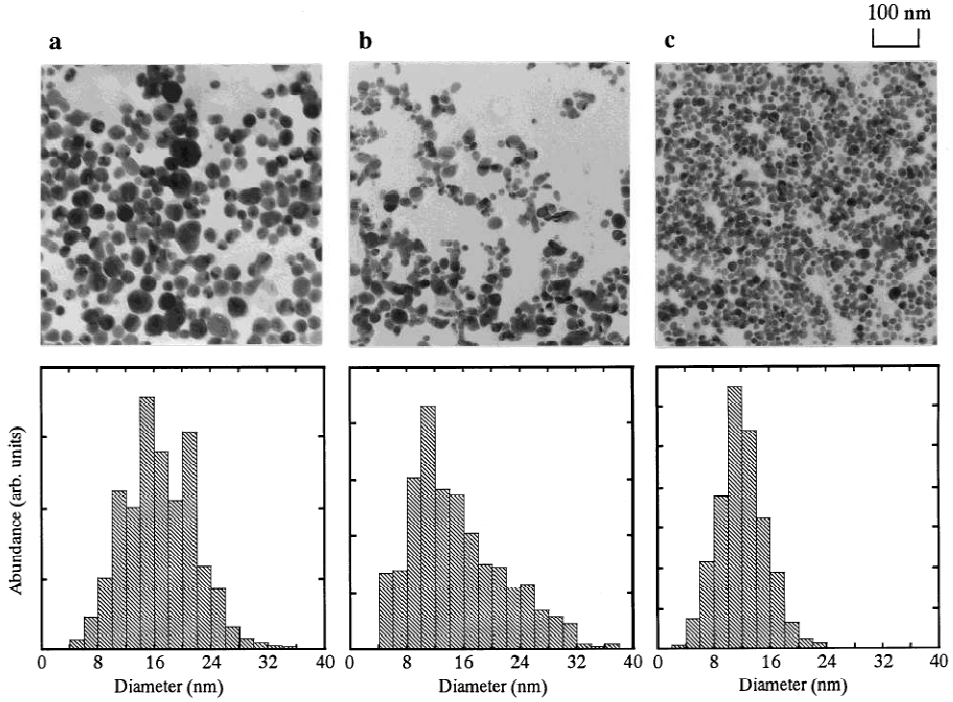

Figure 2.6 Electron micrographs and size distributions of silver nanoparticles produced by laser ablation at 90 mJ/pulse in a SDS aqueous solution with concentration of (a) 0.003 (b) 0.01 and (c) 0.05 M, respectively. It is clearly visible an average size decrease at the increase of the SDS concentration. From ref. **[103]**.

It has been demonstrated that the use of surfactant can interfere also with the shape of growing particles, with resulting structures not obtainable by ablation in pure water.

For example, AgCl nanocubes have been prepared by laser ablation of Ag in 10^{-5}-10^{-1} M NaCl aqueous solution **[105]**.

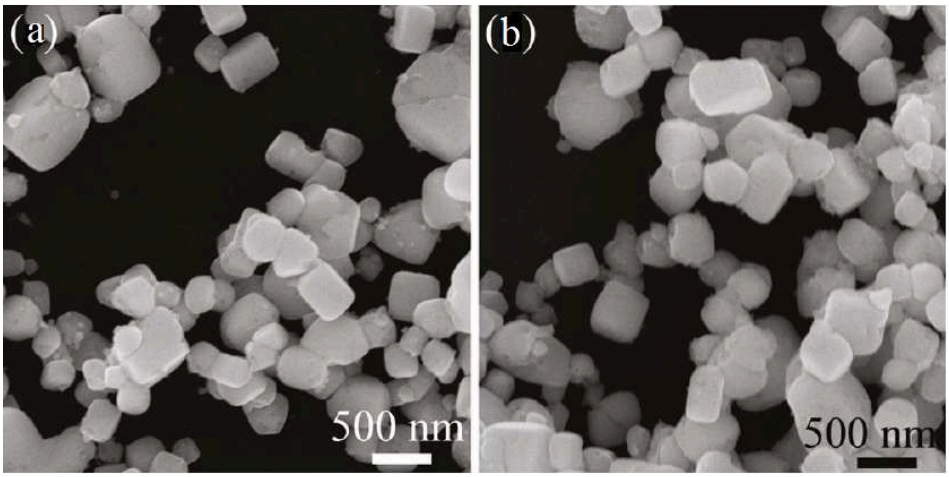

Figure 2.7 SEM images of AgCl cubes obtained in (a) 0.005 M and (b) 0.001 M NaCl solution. From ref. **[105]**

Also Ag_2O cubes, pyramids, triangular plates, pentagonal rods and bars were obtained by ablation of Ag bulk in polysorbate 80 aqueous solutions **[106]**. The surfactant sticks only to particular crystal faces of the structure during the growth and leads to the formation of different geometries **[106]**.

REFERENCES

[1] A. De Giacomo, M. Dell'Aglio, R. Gaudiuso, S. Amoruso, O. De Pascale, *Spectrochim. Acta B*, 2012, **78**, 1–19

[2] A. Bogaerts, Z. Chen, *Spectrochim. Acta B*, 2005, **60**, 1280–1307

[3] B. Le Drogoff, J. Margot, F. Vidal, S. Laville, M. Chaker, M. Sabsabi, T.W. Johnston, O. Barthélemy, *Plasma Sources Sci. Technol.*, 2004, **13**, 223–230

[4] J. Schou, S. Amoruso, J.G. Lunney, in: C. Phipps (Ed.), "Laser Ablation and its Applications", Springer: Berlin, 2007, pp. 67-95

[5] T.E. Itina, *J. Phys. Chem. C*, 2011, **115**, 5044–5048

[6] H.M. Smith, A.F. Turner, *Appl. Optics,* 1965, **4**, 147-148

[7] D. B. Chrisey , G. K. Hubler (Eds.), "Pulsed Laser Deposition of Thin Films", John Wiley & Sons: New York, 1994

[8] B. Luk'yanchuk (Ed.), "Laser cleaning", World Scientific: Singapore, 2000

[9] F. Hillenkamp, J. Peter-Katalinić (Eds.), "MALDI MS: A Practical Guide to Instrumentation, Methods and Applications", Wiley: Weinheim, 2007

[10] D.W. Hahn, N. Omenetto, *Appl Spectrosc.*, 2010, **64**, 335-366

[11] R. Srinivasan, B. Braren, *Chem. Rev*., 1989, **89**, 1303-1316

[12] D. von der Linde, K. Sokolowski-Tinten, in: K.N. Drabovich, V.I. Emelyanova, V.A. Makarov (Eds.), "Icono '98: Fundamental Aspects of Laser-Matter Interaction and New Nonlinear Optical Materials and

Physics of Low-Dimensional Structures", Spie Proceedings Series 3734, , SPIE: Bellingham, 1998

[13] B. Rethfeld, A. Kaiser, M. Vicanek, G. Simon, *Phys. Rev. B*, 2002, **65**, 2143031–21430311

[14] J. Hermann, M. Benfarah, G. Coustillier, E. Axente, J.F. Guillemoles, M. Sentis, P. Alloncle, T.E. Itina, *Appl. Surf. Sci.*, 2006, **252**, 4814–4818.

[15] N.M. Bulgakova, R. Stoian, A. Rosenfeld, I.V. Hertel, E.B. Campbell, in: C. Phipps (Ed.), "Laser Ablation and its Applications", Springer: Berlin, 2007, pp. 17–36.

[16] E.G. Gamaly, A.V. Rode, B. Luther-Davies, in: R. Eason (Ed.), "Pulsed Laser Deposition of Thin Films", Wiley: New York, 2007, pp. 99–129.

[17] B.N. Chichkov, C.Momma, S.Nolte, F. von Alvensleben, A. Tünnermann, *Appl. Phys. A Mater.*, 1996, **63**, 109–115.

[18] X. Zeng, X.L. Mao, R. Greif, R.E. Russo, *Appl. Phys. A Mater.* 2005, **80**, 237–241

[19] M.N.R. Ashfold, F. Claeyssens, G.M. Fuge, S.J. Henley, *J. Chem. Soc. Rev.*, 2004, **33**, 23-31

[20] Y.F. Lu, in: A.H. Guenther (Ed.) "International Trends in Applied Optics", SPIE: Bellingham, 2002. pp. 67-84

[21] G. Bekefi, "Principles of Laser Plasmas", Wiley: New York, 1976.

[22] D. Bleiner, A. Bogaerts, *Spectrochim. Acta B*, 2006, **61**, 421–432

[23] A. Miotello, R. Kelly, *Appl. Phys. A*, 1999, **69**, S67–S73 (Suppl.).

[24] T. Tsuji, Y. Tsuboi, N. Kitamura, M. Tsuji, *Appl. Surf. Sci.*, 2004, **229**, 365-371

[25] J.H. Yoo, S.H. Jeong , R. Greif , R.E. Russo, *J. Appl. Phys.*, 2000, **88**,1638-1649

[26] K.Y. Niu, J. Yang, S.A. Kulinich, J. Sun, H. Li, X.W. Du , *J. Am.Chem. Soc.*, 2010, **132**, 9814-9819

[27] R. Le Harzic, D. Breitling, M. Weikert, S. Sommer, C. Föhl, S. Valette, C. Donnet, E. Audouard, F. Dausinger, *Appl. Surf. Sci.*, 2005, 249, 322-331

[28] J. Cheng, W. Perrie, M. Sharp, S.P. Edwardson, N.G. Semaltianos, G. Dearden, K.G.Watkins, *Appl. Phys. A*, 2009, **95**, 739-746

[29] J. Cheng, W. Perrie, B. Wu, S. Tao, S.P. Edwardson, G. Dearden, K.G. Watkins, *Appl. Surf. Sci*., 2009, **255**, 8171–8175

[30] D.E. Cremers, L.J. Radziemski, in: "Handbook of Laser-Induced Breakdown Spectroscopy", John Wiley & Sons: New York, 2006, pp. 99–168

[31] L.V. Zhigilei, Z. Lin, D.S. Ivanov, *J. Phys. Chem. C*, 2009*,* **113**, 11892–11906

[32] N.M. Bulgakova, R. Stoian, A. Rosenfeld, I.V. Hertel, W. Marine, E.E.B. Campbell, *Appl. Phys. A*, 2005, **81**, 345–356

[33] L.J. Radziemski, D.A. Cremers (Eds.), "Laser-Induced Plasma and Aapplications",Marcel Dekker: New York, 1989.

[34] J.A. Aguilera, C. Aragón, F. Peñalba, *Appl. Surf. Sci.*, 1998, **127–129**, 309–314

[35] S. Amoruso, R. Bruzzese, N. Spinelli, R. Velotta, *J. Phys. B*, 1999, **32,** R13I-R172.

[36] J.G. Lunney, R. Jordan, *Appl. Surf. Sci.*, 1998, **127-129**, 941-946

[37] Y.R. Zel'dovich, Y.P. Raizer, "Physics of Shock Waves and High-Temperature Hydrodynamic Phenomena", Dover: Cambridge, Massachusetts, 2001

[38] K. Saito, K. Takatani, T. Sakka, Y.H. Ogata, *Appl. Surf. Sci.*, 2002, **197**, 56-60

[39] A. De Giacomo, M. Dell'Aglio, O. De Pascale, M. Capitelli *Spectrochim. Acta B*, 2007, **62**, 721–738

[40] G.W. Yang, *Progr. Mater. Sci.*, 2007, **52**, 648–698

[41] D. Devaux, R. Fabbro, L. Tollier, E. Bartnicki, *J. Appl. Phys.*, 1993, **74**, 2268-2273

[42] P. Peyre, R. Fabbro, *Optics Quantum Electron*., 1995, **27**, 1213-1229.

[43] L. Berthe, R. Fabbro, P. Peyer, L. Tollier, E. Bartnicki, *J. Appl. Phys.*, 1997, **82**, 2826-2832

[44] P. Peyer, X. Scherpereel, R. Fabbro, *J. Mater. Sci.*, 1998, **33**, 1421-1429

[45] L. Berthe, R. Fabbro, P. Peyer, E. Bartnicki, *J. Appl. Phys.*, 1999, **85**, 7552-7555

[46] L. Berthe, A. Sollier, R. Fabbro, P. Peyer, E. Bartnicki, *J. Phys. D*, 2000, **33**, 2142-2145

[47] P. Peyer, L. Berthe, R. Fabbro, A. Sollier, *J. Phys. D*, 2000, **33**, 498-503

[48] A. Sollier, L. Berthe, R. Fabbro, *Eur. Phys. J. Appl. Phys.*, 2001, **16**, 131-139

[49] S. Zhu, Y.F. Lu, M.H. Hong, X.Y. Chen, *J. Appl. Phys.*, 2001, **89**, 2400-2403

[50] S. Zhu, Y.F. Lu, M.H. Hong, *Appl. Phys. Lett.*, 2001, **79**, 1396-1398

[51] T. Sakka, K. Takatani, Y.H. Ogate, M.J. Mabuchi, *J. Phys. D*, 2002, **35**, 65-73

[52] T. Sakka, K. Saito, Y.H. Ogata, *Appl. Surf. Sci*., 2002, **197-198**, 246-250

[53] K. Saito, T. Sakka, Y.H. Ogata, *J. Appl. Phys.*, 2003, **94**, 5530-5536

[54] A. De Giacomo, M. Dell'Aglio, O. De Pascale, *Appl. Phys. A*, 2004, **79**, 1035–1038

[55] A. De Giacomo, R. Gaudiuso, M. Dell'Aglio, A. Santagata, *Spectrochim. Acta B*, 2010, **65**, 385–394

[56] N. Ohno, M.A. Razzak, H. Ukai, S. Takamura, Y. Uesugi, *Plasma Fusion Res.*, 2006, **1**, 028-1/028-9

[57] H.R. Griem, "Principles of Plasma Spectroscopy", Cambridge University Press: Cambridge, 1997

[58] T. Sakka, S. Iwanage, Y.H. Ogata, A. Matsunawa, T. Takemoto, *J. Chem. Phys.*, 2000, **112**, 8645-8653

[59] P.P. Patil, D.M. Phase, S.A. Kulkarni, S.V. Ghaisas, S.K. Kulkarni, S.M. Kanetkar, S.B. Ogale, V.G. Bhide, *Phys. Rev. Lett.* ,1987, **58**, 238-241

[60] G.W. Yang, J.B. Wang, *Appl. Phys. A*, 2000, **71**, 343-344

[61] Y.F. Lu, S.M. Huang, X.B. Wang, Z.X. Shen, *Appl. Phys. A*, 1998, **66**, 543-547

[62] A.A. Lyalin, A.V. Simakin, E.N. Loubnin, G.A. Shafeev, *Appl. Phys. A*, 1999, **68**, 373-376

[63] S.M. Huang, Y.F. Lu, Z. Sun, *Appl. Surf. Sci.*, 1999, **151**, 244-250

[64] A.V. Simakin, E.D. Obraztsova, G.A. Shafeev, *Chem. Phys. Lett.* 2000, **332**, 231-235

[65] W. Inoue, M. Okoshi, N. Inoue, *Appl. Phys. A*, 2004, **79**, 1457-1460

[66] G.W. Yang, J.B. Wang, *Appl. Phys. A*, 2001, **72**, 475–479

[67] P. Giovanneschi, D. Dufresne, *J. Appl. Phys.*, 1985, **58**, 651–652

[68] J.G. Fujimoto, W.Z. Lin, E.P. Ippen, C.A. Puliafito, R.F. Steinert, *Invest. Ophthalmol. Vis. Sci.*, 1985, **26**, 1771–1777

[69] A. Vogel, S. Busch, U. Parlitz, *J. Acoust. Soc. Am.*, 1996, **100**, 148–164

[70] T. Sakka, S. Masai, K. Fukami, Y.H. Ogata, *Spectrochim. Acta B*, 2009, **64**, 981–985

[71] J. Sun , S. L. Hu , X. W. Du , Y. W. Lei , L. Jiang , *Appl. Phys. Lett.* 2006, **89**, 183115

[72] K.Y. Niu , J. Yang , J. Sun , X.W. Du , *Nanotechnology*, 2010, **21**, 295604

[73] K.Y. Niu, J. Yang, S.A. Kulinich, J. Sun, X.W. Du, *Langmuir*, 2010, **26**, 16652-16657

[74] H.M. Zhang, C.H. Liang, Z.F. Tian, G.Z. Wang, W. P. Cai, *J. Phys. Chem. C*, 2010, **114**, 12524-12528

[75] A.V. Simakin, V.V. Voronov, G.A. Shafeev, R. Brayner, F. Bozon-Verduraz, *Chem. Phys. Lett.*, 2001, **348**, 182-186

[76] A. Pyatenko, K. Shimokawa, M. Yamaguchi, O. Nishimura, M. Suzuki, *Appl. Phys. A*, 2004, **79**, 803-806

[77] S.I. Dolgaev, A.V. Simakin, V.V. Voronov, G.A. Shafeev, F. Bozon-Verduraz, *Appl. Surf. Sci.*, 2002, **186**, 546-551

[78] F. Bozon-Verduraz, R. Brayner, V.V. Voronov, N.A. Kirichenko, A.V Simakin, G.A. Shafeev, *Quantum Electron.*, 2003, **33**, 714-720

[79] G. Compagnini, A.A. Scalisi, O. Puglisi, *Phys. Chem. Chem. Phys.*, 2002, **4**, 2787-2791

[80] G. Compagnini, A.A. Scalisi, O. Puglisi, *J. Appl. Phys.*, 2003, **94**, 7874-7877

[81] G. Compagnini, A.A. Scalisi, O. Puglisi, C. Spinella, *J. Mater. Res.*, 2004, **19**, 2795-2798

[82] J.P. Sylvestre, S. Poulin, A.V. Kabashin, E. Sacher, M. Meunier, J.H.T. Luong, *J. Phys. Chem. B*, 2004, **108**, 16864-16869

[83] J.P. Sylvestre, A.V. Kabashin, E. Sacher, M. Meunier, J.H.T. Luong, *J. Am. Chem. Soc.*, 2004, **126**, 7176-7177

[84] A.V. Kabashin, M. Meunier, C. Kingston, J.H.T. Luong, *J. Phys. Chem. B*, 2003,**107**, 4527-4531

[85] W.G. Zhang, Z.G. Jin, *Sci. China Ser. B*, 2004, **47**, 159-165

[86] F. Mafune, J. Kohno, Y. Takeda, T. Kondow, H. Sawabe, *J. Phys. Chem. B*, 2001, **105**, 5114-5120

[87] F. Mafune, J. Kohno, Y. Takeda, T. Kondow, H. Sawabe, *J. Phys. Chem. B*, 2002, **106**, 7575-7577

[88] F. Mafune, J. Kohno, Y. Takeda, T. Kondow, H. Sawabe, *J. Phys. Chem. B* 2003, **107**, 12589-12596.

[89] T. Tsuji, K. Iryo, N. Watanabe, M. Tsuji, *Appl. Surf. Sci.*, 2002, **202**, 80-85

[90] T. Tsuji, T. Kakita, M. Tsuji, *Appl. Surf. Sci.* 2003, **206**, 314-320

[91] C.H. Liang, Y. Shimizu, T. Sasaki, N. Koshizaki, *J. Phys. Chem. B*, 2003, **107**, 9220-9225

[92] J. Chen, Q. Dong, J. Yang, Z. Guo, Z. Song, J. Lian, *Mater. Lett.*, 2004, **58**, 337– 341

[93] Y.P. Lee, Y.H. Liu, C.S. Yeh, *Phys. Chem. Chem. Phys.*, 1999, **1**, 4681-4686

[94] K. Yatsui, T. Yukawa, C. Grigoriu, M. Hirai, W. Jiang, *J. Nanopart. Res.* 2000, **2**, 75-83

[95] C.H. Liang, Y. Shimizu, Y. Masuda, T. Sasaki, N. Koshizaki, *Chem. Mater.*, 2004, **16**, 963-965

[96] C.H. Liang, Y. Shimizu, T. Sasaki, N. Koshizaki, *Chem. Phys. Lett.*, 2004, **389**, 58-63

[97] M. Nath, C.N.R. Rao, R. Popvitz-Biro, A. Albu-Yaron, R. Tenne, *Chem. Mater.*, 2004, **16**, 2238-2243

[98] G. Compagnini, M.G. Sinatra, G.C. Messina, G. Patanè, S. Scalese, O. Puglisi, *Appl. Surf. Sci.*, 2012, **258**, 5672–5676

[99] G.W. Yang, J.B. Wang, Q.X. Liu, *J. Phys: Condens. Mater.*, 1998, **10**, 7923-7927

[100] J.B. Wang, C.Y. Zhang, X.L. Zhong, G.W. Yang, *Chem. Phys. Lett.*, 2002, **361**, 86-90

[101] H. Furusawa, T. Sakka, Y.H. Ogata, *J. Appl. Phys.*, 2004, **96**, 975-982

[102] C.Y. Zhang, C.X. Wang, Y.H. Yang, G.W. Yang, *J. Phys. Chem. B*, 2004, **108**, 2589-2593

[103] F. Mafuné, J. Kohno, Y. Takeda, T. Kondow, H. Sawabe, *J. Phys. Chem. B*, 2000**, 104***,* 9111-9117

[104] X. Zhang , H.B. Zeng, W. Cai, *Mater. Lett.*, 2009, **63**, 191-193

[105] Z. Yan, G. Compagnini, D.B. Chrisey, *J. Phys. Chem. C*, 2011, **115**, 5058-5062

[106] Z. Yan , R. Bao , D.B. Chrisey , *Langmuir*, 2011, **27**, 851-855

CHAPTER 3: HIGH YIELD PRODUCTION OF METAL NANOPARTICLES BY WIRE ABLATION

3.1 INTRODUCTION

The large number of recent studies on unique and intriguing antibacterial, optical and electric properties of silver nanoparticles (Ag NPs) has opened the way to several tries to exploit them for the creation of devices of different nature. As a result, companies have increased their interest in the creation of new techniques for the production of nanoparticles with the desired quality for applications in high technology devices **[1-3]**. From this point of view, pulsed laser ablation in liquids (PLAL) seems to be an excellent preparation method, since it allows the preparation of high pure ligand-free NPs in liquid phase ready for incorporation in different matrices **[4-5]** or functionalization with biomolecules **[6]**. On the other side, the main disadvantage of laser ablation is the low amount of produced material. One of the strategies to increase the productivity could be considering the use of high-power laser sources, but it should be evaluated that systems such as excimer lasers with UV wavelengths are expensive, feature which is not compatible with an industrial approach. Thus, the employ of solid state lasers still remains the favored choice.

Literature shows several reports about nanoparticles preparation by high power pulsed Nd:YAG lasers, but it seems that the mere increase of the source power does not enhance productivity significantly **[7-9]**.

For this reason, a deep knowledge of the ablation mechanism is required in order to develop new strategies to enlarge production rate. From the study of the cavitation bubble dynamics it has been demonstrated that the spatial bypassing of the bubble itself, obtained using fast optics scanning, can lead to an increase of the productivity **[10]**. Best results have been reached for a scan speed of 500 mm/s, corresponding to an interpulse distance of 125 μm, which avoids the hit of the cavitation bubble containing primary nanoparticles that can scatter, absorb or reflect the subsequent laser pulse. It has been also reported that if the interpulse distance increases again, it results in an inadequate overlap that leads to thermally isolated areas, causing inefficient material removal **[10]**.

Also the influence of the surrounding liquid medium on ablation efficiency has been widely investigated. It has been demonstrated that the thickness of the liquid layer above the target is responsible for variations in the amount of ablated material **[11]**. In particular, the optimum yield has been obtained for a water layer of 1.2 mm, since the shock wave, and thus the amount of removed material, depends on the pressure generated by the liquid layer. The introduction of a liquid flow inside the ablation environment can influence the ablation ratio as well **[12]**. On one side, the liquid flow helps the detachment of material from the solid target leading to an increase of the amount of material in the liquid. On the other side, if the laser wavelength used for the ablation is near the

plasmon resonance of produced nanoparticles, such for example when ablating gold or silver with the second harmonic of a Nd:YAG laser (λ= 532 nm), the circulating liquid removes the particles from the ablation medium, avoiding the absorption of the laser radiation.

It is also possible to reduce the dimension of the target in order to obtain a more efficient use of the laser energy. Glass and metal nanoparticles have been prepared by laser ablation of microspheres (LAM) using a KrF laser. It has been found that the reduction of the bulk size provokes a less significant energy loss by heat phenomena and as a consequence, microsphere present a lower ablation threshold respect to bulk targets, meaning a more efficient energy harvesting **[13-17]**.

However, when working with microspheres, two main problems should be taken in account: the low hitting rate of the laser beam with microspheres and the poor collecting method of the nanoparticles **[13-14]**.

Further developments in this direction have been reached by operating the laser ablation of a tiny wire, which acting as a monodimensional conductor, allows to increase the production yield of nanoparticles **[18]**.

In addition, a wire target can be fed continuously inside a chamber, characteristic that makes this approach suitable for industrial applications.

A scaled up process, indeed, needs two main requirements, which are high amount of products and continuity, assured when all reactants (in the case of laser ablation the target and the surrounding liquid) are fed in a continuous way.

Then, the use of a wire continuously fed inside the chamber, together with the use of a liquid flow, will assure the continuous nature of the process.

3.2 EXPERIMENTAL DETAILS

The fulfilling of all the experimental requirements have been assured by the use of a custom designed ablation chamber, reported in fig. 3.1.

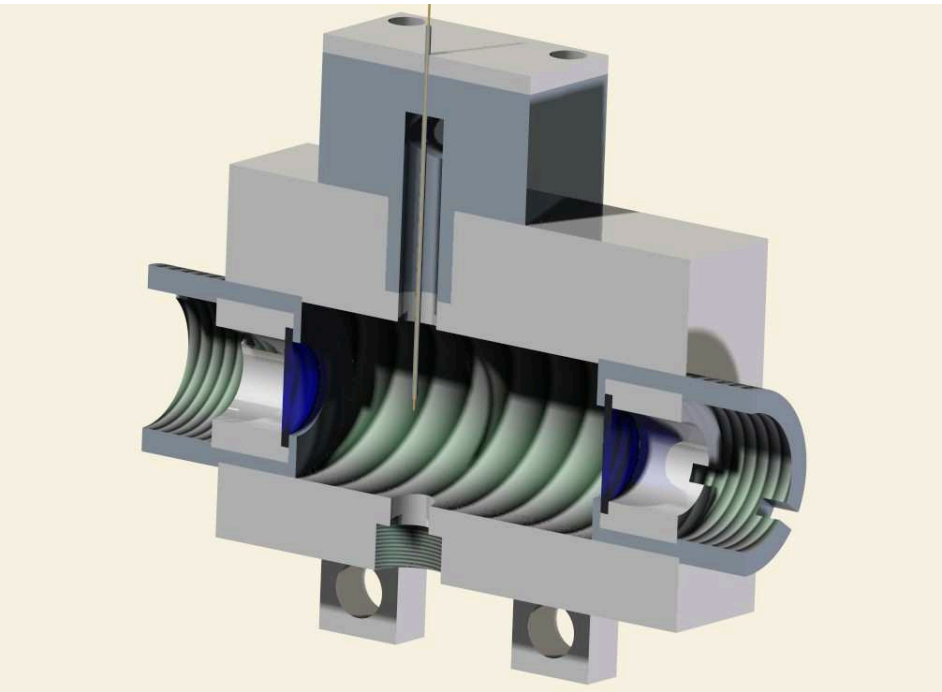

Figure 3.1 Cutaway drawing of the ablation chamber used for the ablation of the silver wire in water flow.

The top of the chamber presents a wire feeding system controlled by a computer unit and the entrance of the water flow, assured by a pump (which has been set at a rate of 9 ml/sec). The wire and the liquid are introduced in the same direction inside the chamber in order to avoid possible bending of the wire, which could affect the reproducibility of the process. The laser source used for experiments is the first harmonic (λ=1064 nm) of a Nd:YAG (model Spitlight DPSS 250 from InnoLas) with 10 nanosecond pulse duration. The laser beam undergoes diameter reduction (from 6 to 3 mm) by passing through a Galilean telescope and then crosses the chamber where it provides to ablate the wire.

Fluencies used in this work ranged from 0.4 J/cm^2 to 1.5 J/cm^2 and repetition rate from 1 Hz to 10 Hz.

Experiments have been carried out on 99.9% pure silver wires with seven different diameters (250 μm, 750 μm and 1500 μm diameter wires from Advent Materials, 125 μm and 500 μm from Alfa Aesar, 350 μm from Goodfellow, 1000 μm from Strem Chemicals). Results have been compared with those obtained using a silver plate as target (Ag 99,9% 1 mm thick from Goodfellow) and platinum and tungsten wires with 500 μm diameter (99.9% pure Pt and W wire from Strem Chemicals).

In order to assure the centring of the laser beam on the wire target, the energy coming out from the rear window of the chamber has been minimized by measuring it with a power meter (FieldMaxII-Top from Coherent, Inc.) and the steady state condition of the process has been controlled by a camera positioned on the side of the chamber.

The ablation rate has been calculated reaching steady state ablation condition and then measuring the feeding speed of the wire inside the chamber. A steady state ablation is reached when the feeding speed allows the complete ablation of the wire when moving to the lower part of the chamber. From the feeding speed and the diameter of the wire it is so possible to calculate the amount of ablated wire and then the ablated mass per time. The applicability of this procedure was verified by comparison with gravimetric determination of ablation rate.

To obtain information about the ablation mechanism different techniques have been used and in particular optical emission spectroscopy for the plasma characterization, fast shadowgraph for plasma and cavitation dynamics and laser scattering for the mechanisms of delivery of the produced materials in the liquid.

Fig. 3.2 shows the experimental set-up for the plasma and cavitation bubble characterization part of this work. The laser used for the ablation is a Nd:YAG 532 nm (PILS-GIANT model from Quanta System), with 8 nanoseconds pulse width, a repetition rate 10 Hz and adjustable energy up to 400 mJ. The experimental set-up for the emission spectra acquisition of plasma in water consists of a spectroscopic system (a monochromator Jobin Yvon TRIAX 550, an ICCD Jobin Yvon i3000 and a pulse generator Stanford inc. DG 535 for the synchronization of laser pulse and ICCD) and a stainless steel chamber for water atmospheric pressure experiments. The chamber is equipped with 90° spacer tubes to locate a focusing lens and sapphire optical windows. The sample is placed inside the chamber onto a rotating target holder with the

possibility of 10 mm axial movement. To focus the laser pulse on to the sample, a 4.0 cm focusing lens in air is inserted into the spacer tube since it allows adjusting the distance between the lens and the sample. To collect the plasma emission through the dedicated optical window a biconvex 7.5 cm focal quartz lens has been placed outside the chamber.

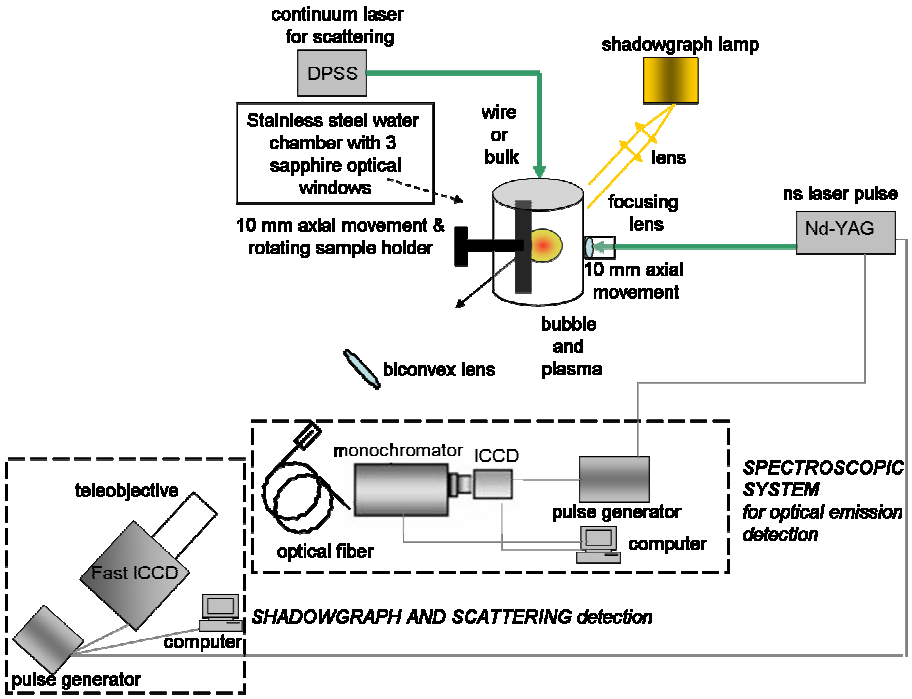

Figure 3.2 Experimental setup for optical emission spectroscopy, shadowgraph and scattering experiments.

The set-up for the shadowgraph measurements consists of a light source, a set of lens to reduce light divergence, the water chamber, a fast ICCD detection system (PI Max II, 1024x1024 pixels) with a teleobjective

(Nikon) to collect the shadow of the bubble and a pulse generator to synchronize laser pulses with the ICCD.

The set up for the scattering measurements consists of a continuum laser DPSS at 532 nm (Cobolt Samba, 25 mW, CW) and a spectroscopic system that is the same used for the shadowgraph experiment. The scattering measurements have been performed simultaneously to the shadowgraph one. The laser pulse has been focused onto a target or a wire placed inside the chamber filled with de-ionized water. For the optical emission spectroscopy the sample was rotated during the measurements to limit the depth of crater excavation on the surface, instead during the shadowgraph and scattering analyses, the sample was kept fixed to avoid the bubbles formation along the optical path, but shifting it after each measurement. Different targets have been employed both in bulk and wire shapes such as Cu, Ag, Ti, Fe and Pt.

3.3 NORMALIZATION OF EFFICIENCY DATA

The use of an unfocused beam with a diameter of 3 mm assures the complete and continuous ablation with a total consumption of the wire in the laser impinging region. In this condition, the laser beam dimension is always larger than the diameter of the wire, completely surrounding it. Thus, only part of the energy coming out from the laser will arrive on the target, while the other part will pass through the wire not contributing to

the ablation of the target. For this reason, collected data need to be corrected through a proper normalization method before being compared. The normalization on energy of ablation efficiency values has been carried out approximating the energy profile of the TEM_{00} mode of the laser beam to a two dimensional Gaussian distribution. Since the laser beam presents a diameter of 3 mm, the energy profile can be described by a distribution with a value of $\sigma^2=0.2$ as described in eq. (3.1).

$$f(x,y) = \frac{1}{0.4\pi} e^{-\frac{1}{2}\left(\frac{x^2}{0.2}+\frac{y^2}{0.2}\right)} \tag{3.1}$$

The integral of eq. (3.1) on the boundaries of a circumference with a radius of 1.5 mm will give the total amount of energy coming out from the laser. The calculated integral is reported on eq. (3.2).

$$\int_0^{2\pi}\int_0^{1.5} \frac{1}{0.4\pi} r e^{-\frac{1}{2}\left(\frac{\cos\vartheta^2+\sin\vartheta^2}{0.2}\right)} d\vartheta dr = 0.996393 \tag{3.2}$$

In the case of wire targets, integral boundaries should be fixed considering the diameter of the wire itself. In this way, wires with higher diameters will absorb a higher amount of energy respect to smaller wires. The integral of the curve between boundaries of the target is then proportional to the energy arriving on it and the maximum of the curve should correspond to the energy arriving on the wire, since the laser beam is centered. Calculated integrals which represent the value of absorbed energies, are reported as following here for wires with diameter ranging from 125 µm (eq.(3.3)) to 1500 µm (eq.(3.9)).

$$\int_{-0.0625}^{0.0625}\int_{-1.5}^{1.5} \frac{1}{0.4\pi} e^{-\frac{1}{2}\left(\frac{x^2+y^2}{0.2}\right)} dxdy = 0.111057 \qquad 125\ \mu m \tag{3.3}$$

$$\int_{-0.125}^{0.125}\int_{-1.5}^{1.5} \frac{1}{0.4\pi} e^{-\frac{1}{2}\left(\frac{x^2+y^2}{0.2}\right)} dxdy = 0.21997 \qquad 250\ \mu m \tag{3.4}$$

$$\int_{-0.175}^{0.175}\int_{-1.5}^{1.5}\frac{1}{0.4\pi}e^{-\frac{1}{2}\left(\frac{x^2+y^2}{0.2}\right)}dxdy = 0.304191 \qquad 350\ \mu m \quad (3.5)$$

$$\int_{-0.25}^{0.25}\int_{-1.5}^{1.5}\frac{1}{0.4\pi}e^{-\frac{1}{2}\left(\frac{x^2+y^2}{0.2}\right)}dxdy = 0.423512 \qquad 500\ \mu m \quad (3.6)$$

$$\int_{-0.375}^{0.375}\int_{-1.5}^{1.5}\frac{1}{0.4\pi}e^{-\frac{1}{2}\left(\frac{x^2+y^2}{0.2}\right)}dxdy = 0.597788 \qquad 750\ \mu m \quad (3.7)$$

$$\int_{-0.5}^{0.5}\int_{-1.5}^{1.5}\frac{1}{0.4\pi}e^{-\frac{1}{2}\left(\frac{x^2+y^2}{0.2}\right)}dxdy = 0.735861 \qquad 1000\ \mu m \quad (3.8)$$

$$\int_{-0.75}^{0.75}\int_{-1.5}^{1.5}\frac{1}{0.4\pi}e^{-\frac{1}{2}\left(\frac{x^2+y^2}{0.2}\right)}dxdy = 0.905746 \qquad 1500\ \mu m \quad (3.9)$$

A graphical representation of the amount of energy arriving on the target is reported in fig. 3.3.

The ratio between values calculated for the wires and the one on the whole surface represents the ratio between energy coming inside the chamber and the energy absorbed by the wire.

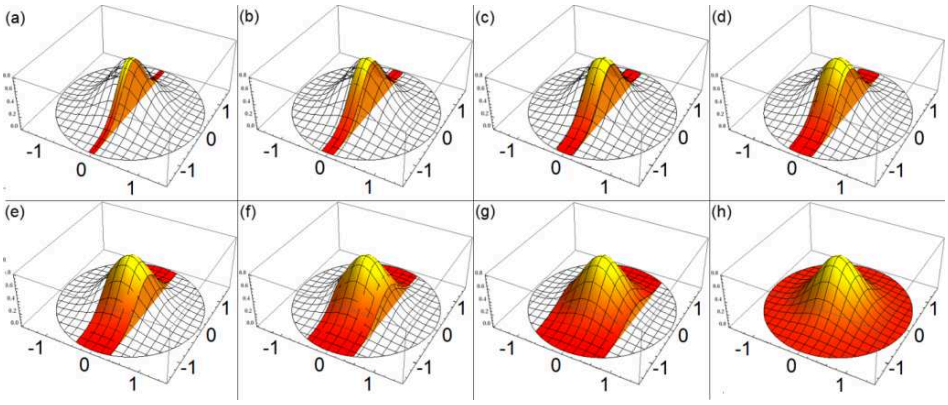

Figure 3.3 Graphical representation of the calculated amount of energy arriving on the target for wire with diameter of (a) 125 µm (b) 250 µm (c) 350 µm (d) 500 µm (e) 750 µm (f) 1000 µm (g) 1500 µm and (h) bulk target.

Since the laser used for the experiments presents a M^2 factor of 1.8, which means that there is a not negligible divergence of the laser beam energy profile from the Gaussian shape, it seemed appropriate to compare calculations with experimental energy values in order to determine the accuracy of the model.

To achieve this, the energy coming out from the back window of the chamber has been measured when no target is positioned inside it and when wire ablation with different wires is happening. Results are reported in fig. 3.4.

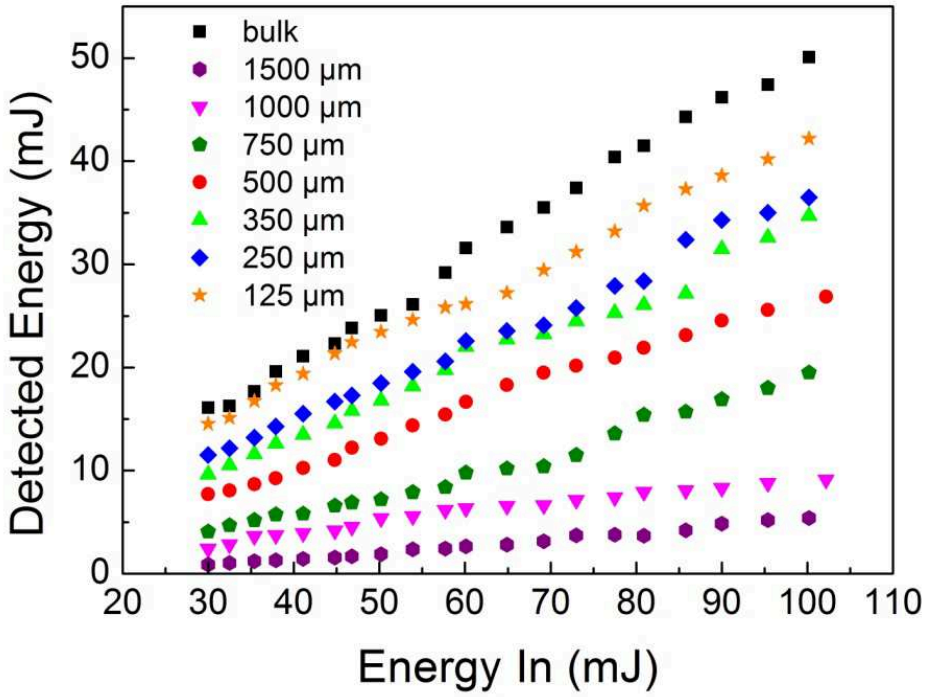

Figure 3.4 Detected energy from the back window of the chamber when no target is positioned it (black squares) and when ablation of wire happens (colored markers).

Measured energy values obtained for different wires have been subtracted to the energy detected when no target is positioned inside the chamber. Resulting values of energy, reported in fig. 3.5, correspond to the amount of energy which is absorbed by the wire, even if this not means that all the energy is used for the ablation of the wire itself.

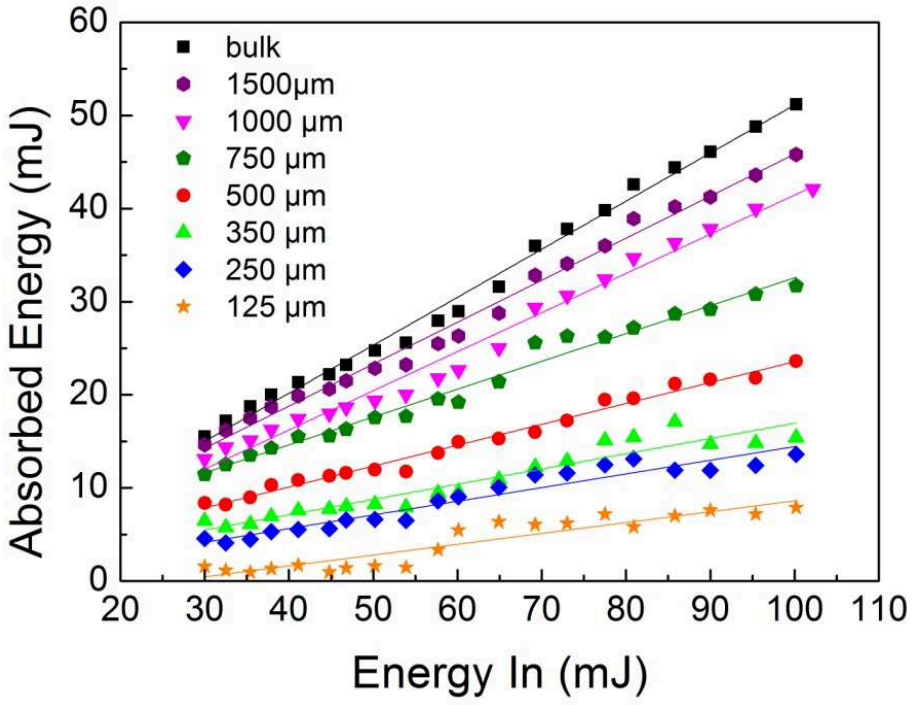

Figure 3.5 Values of energy absorbed by wires of different shapes obtained by the subtraction of Detected Energy values for different wire diameters to "no target" one reported in fig. 3.4.

The ratio between the slopes of the curves obtained for the wires and the slope of the curve for the bulk have been compared to calculated values in order to check the reliability of the model and are reported in fig. 3.6.

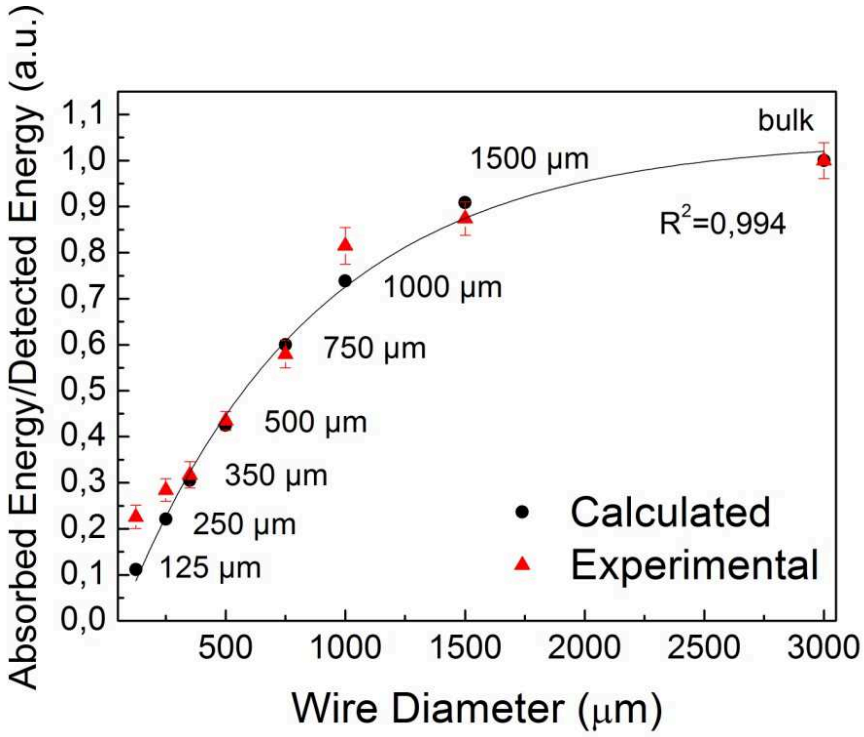

Figure 3.6 Calculated (black circles) and experimental (red triangles) energy ratios for wire of different diameters and for bulk target.

It is possible to observe a good agreement between calculated and experimental values with a moderate failure at low diameters. This can be interpreted considering that the surface reflects part of the radiation arriving on it in a way which depends on the angle of incidence, as described by Snell's law, and then on the curvature radius. Although the incident beam is always larger than the wire diameter, reflection occurs

at the edge of the wire due to its curvature. For smaller wires, the fraction of reflected light is higher since the laser intensity follows a Gaussian distribution.

3.4 ABLATION EFFICIENCY

Fig. 3.7 reports such normalized ablation efficiency as a function of fluence for silver wires with seven different diameters, ranging from 125 µm to 1500 µm and a silver plate target for comparison.

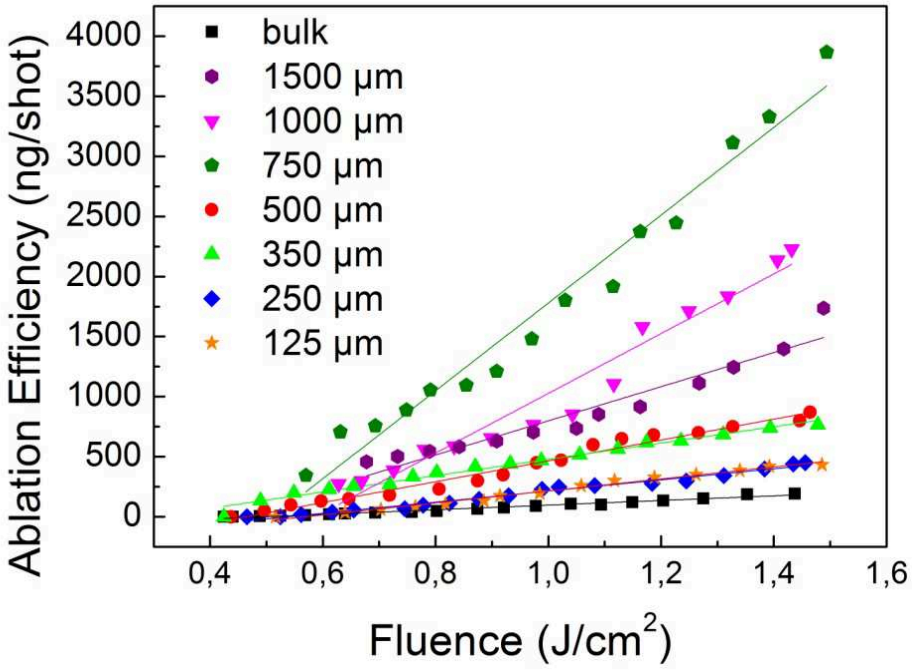

Figure 3.7 Corrected ablation efficiency in function of the fluence for wires with diameter ranging from 125 µm to 1500 µm (colored markers) and bulk target (black squares).

It is straightforward to note a linear increase of the ablated material at the increasing of the fluence for all the targets considered in the experiment. The linear correlation of ablated mass with the fluence has already been reported in literature in the case of a bulk target **[19]**.

Optical emission spectroscopy measurements performed on the ablation plume have shown influence of the laser fluence on the plume temperature, which was found to be proportional to the ablated volume **[20]**.

This means that an increase of the laser fluence leads to a larger amount of ablated material. In any case, variations of these plume properties were only observed in the range of fluencies close to the ablation threshold that is the case reported for these experiments **[21]**.

It is also to notice that efficiency values obtained for all targets are higher than those reported in literature in the same fluence **[22]**.

Such a difference can be attributed to the use of a liquid flow inside the ablation chamber. This moves away nanoparticles from the ablation region, avoiding that the ablated material remains attached to the target. **[12]**.

Efficiency values at the maximum fluence used for the experiments (1.5 J/cm^2) have been plotted in function of the wire diameter and obtained results are reported in fig. 3.8.

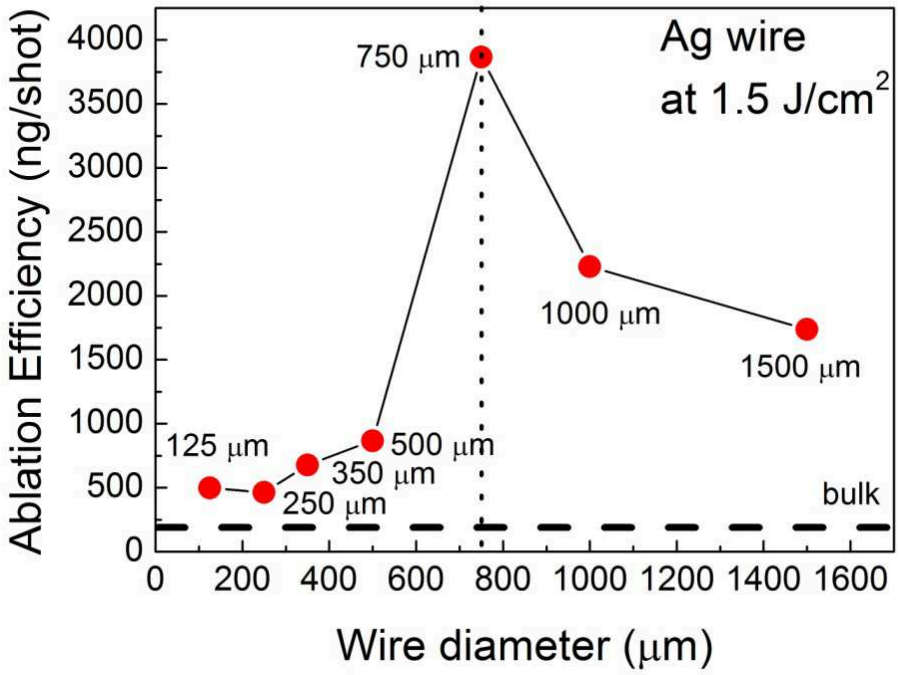

Figure 3.8 Ablation efficiency of silver targets at 1.5 J/cm^2 as a function of the wire diameter. The efficiency value for a bulk target is also reported for comparison.

The most intriguing consideration about particle production is how it varies in function of the wire diameter.

First of all, it is to note that all the efficiency values for wire ablation are greater than in bulk case by at least a factor of 2. This evidence can be interpreted considering that during wire ablation, heat dissipation happens only in one dimension, as already discussed.

Going into details of the figure, it is possible to observe that efficiency reaches a maximum and then decreases. Such a trend should be justified

considering different effects. One of them involves the way in which heat is dispersed during the ablation process. As previously discussed in literature **[23-24]**, inefficient heat dispersion leads to accumulation of heat on the surface of the target and a subsequent phase explosion-like mechanism might cause a higher ablation efficiency of material. This means that there is a correlation between ablation efficiency data and the way heat is dispersed inside the target. For cylindrical shapes, heat transmission decreases with decreasing cross section. Thus, thicker wires will dissipate heat more easily resulting in a more efficient heat loss and subsequently lower production rate. For a very thick wire, ablation efficiency should reach the limit of a bulk target (reported as a dash line in fig. 3.8). This non-linear decrease can be clearly seen in fig. 3.8 for wire diameters higher than 750 μm. In more detail, heat loss is described by the heat equation (3.10):

$$\frac{\partial T(x,t)}{\partial t} = \alpha \cdot \Delta T(x,t) \tag{3.10}$$

Heat dispersion is determined by the area-specific heat loss given by the Laplace-operator Δ and the thermal diffusivity α. To verify the influence of thermal diffusivity, we also performed experiments at fixed diameters by using metallic wires (of silver, platinum and tungsten) with different thermal diffusivities. The graph in fig. 3.9 presents a definite linear relation between nanoparticle production and thermal diffusivity α, with the highest amount of material obtained for platinum, which presents the lowest thermal diffusivity value.

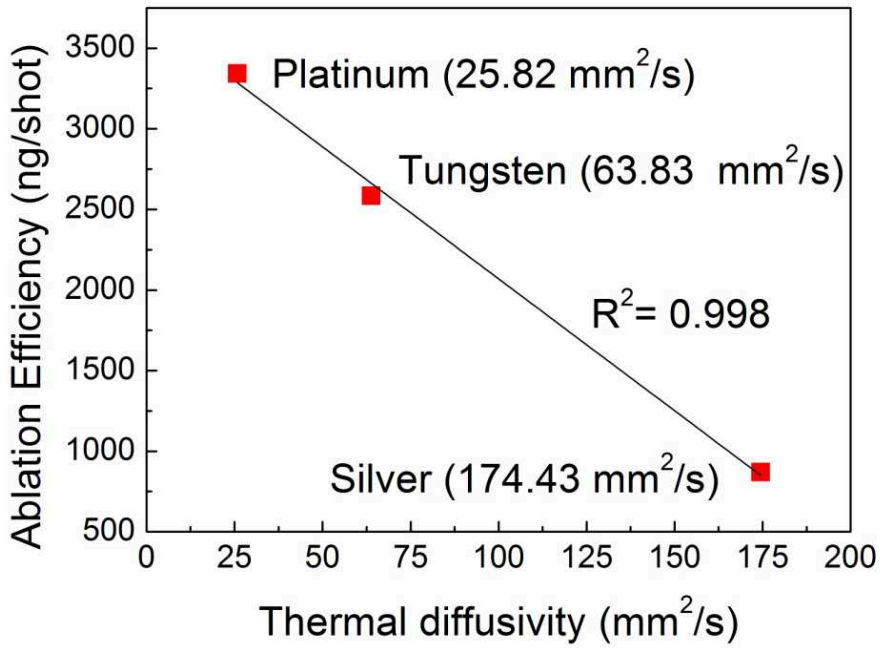

Figure 3.9 Ablation efficiency at 1.5 J/cm^2 as a function of thermal diffusivity for wires with 500 μm diameter made of Platinum (25.82 mm^2/s), Tungsten (63.83 mm^2/s) and Silver (174.43 mm^2/s).

These results show correlation of ablation efficiency with heat loss, in accordance with eq. (3.10), and so it seems appropriate to state that heat dispersion play a fundamental role in the production rate of nanoparticles at this stage.

The above picture is not able to describe the efficiency behaviour for diameters lower than 750 μm. Indeed, several effects should be taken into account when the diameter of the wire decreases further:

1) The increasing of the surface to volume ratio at the decreasing of the wire diameter, contributing to higher heat dissipation, since heat exchanges with the surrounding liquid are more favored.

2) The overall reflectivity of a wire is radius dependent, as already discussed previously. Then, when a thin wire is irradiated, less energy is absorbed and used for ablation of material, since higher intensities are reflected, as shown in fig. 3.10. For very thin wires, irradiation is due only to the top of the Gaussian beam, which is more intense.

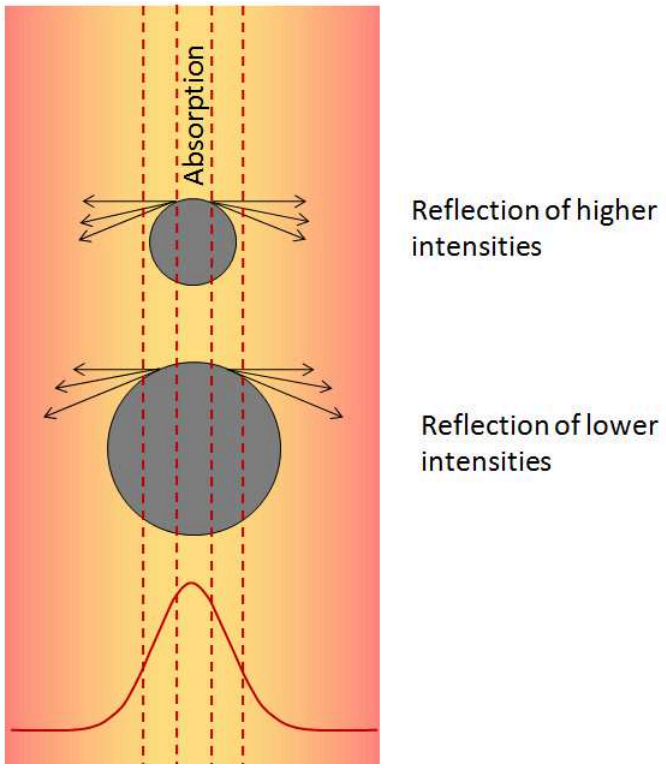

Figure 3.10 Reflection of the incoming laser beam for thin and thick wires.

3) Cavitations bubble dynamics differs if a bulk or a wire target is used.
It should be considered that all these effects contribute to the increase of the efficiency in the first part of fig. 3.8.
Particularly interesting seems to be the correlation between the reported data and the cavitation bubble behaviour for wires. Cavitation bubble is a free liquid region surrounding the ablated spot containing the material expelled by the target.
The investigation of cavitation bubble is a complicate mechanism, since it involves processes that happen in short timescales. So, they require high temporal and spatial resolution **[25]**.

3.5 LASER INDUCED PLASMA ANALYSIS

As already discussed in section 2.2a, when a solid target is irradiated through a liquid with irradiance higher than 0.1 GW/cm^2, atomization and ionization processes of the irradiated spot occur and a plasma, called Laser Induced Plasma (LIP), is produced. The mechanisms responsible for the plasma formation are the same for the plasma formation during laser ablation in gas phase **[26]**. Laser energy is converted in excitation of bound electrons in the solid target, if the laser energy is beyond the ablation threshold, electrons are removed by the electromagnetic field of the atomic nuclei by Multiphoton Ionization. When working with nanosecond pulses, those free electrons, also referred as seed electrons, can continue to absorb laser photons by Inverse Bremsstrahlung,

increasing in this way their kinetic energy and inducing further ionization by electron impact collisions.

Those events lead to the explosive formation of a dense plasma, which initially expands at supersonic velocity. As a consequence of the fast expansion, the plasma acts as piston against the surrounding environment, generating shock waves which travel in opposite direction that means toward the target on one direction and toward the liquid in the other **[27]**.

The shock wave directed toward the target can by described by eq. (3.11), which allows estimating the maximum pressure of the shock wave in MPa **[28]**.

$$P_{SW,inw} = 10^{-2}\sqrt{\frac{\alpha}{\alpha+3}\cdot\sqrt{z}\cdot\sqrt{I_0}} \tag{3.11}$$

Where α is the interaction efficiency (which typically assumes a value of 0.3^2**[29]**), z is the reduced impedance expressed in g/cm^2·s **[28]** and I_0 is the laser irradiance in GW/cm^2. In experiments reported ablating a Cu wire, the pressure of the inward shockwave varies from $3\cdot10^8$ to $7\cdot10^8$ Pa. When ablating a bulk target, this pressure on the solid target does not affect the experiments, provided that the target is well fixed on the rotating holder. On the other hand they are high enough to induce oscillations of wire or thin plates.

The outward cavitation bubble can be directly investigated by shadowgraph experiments.

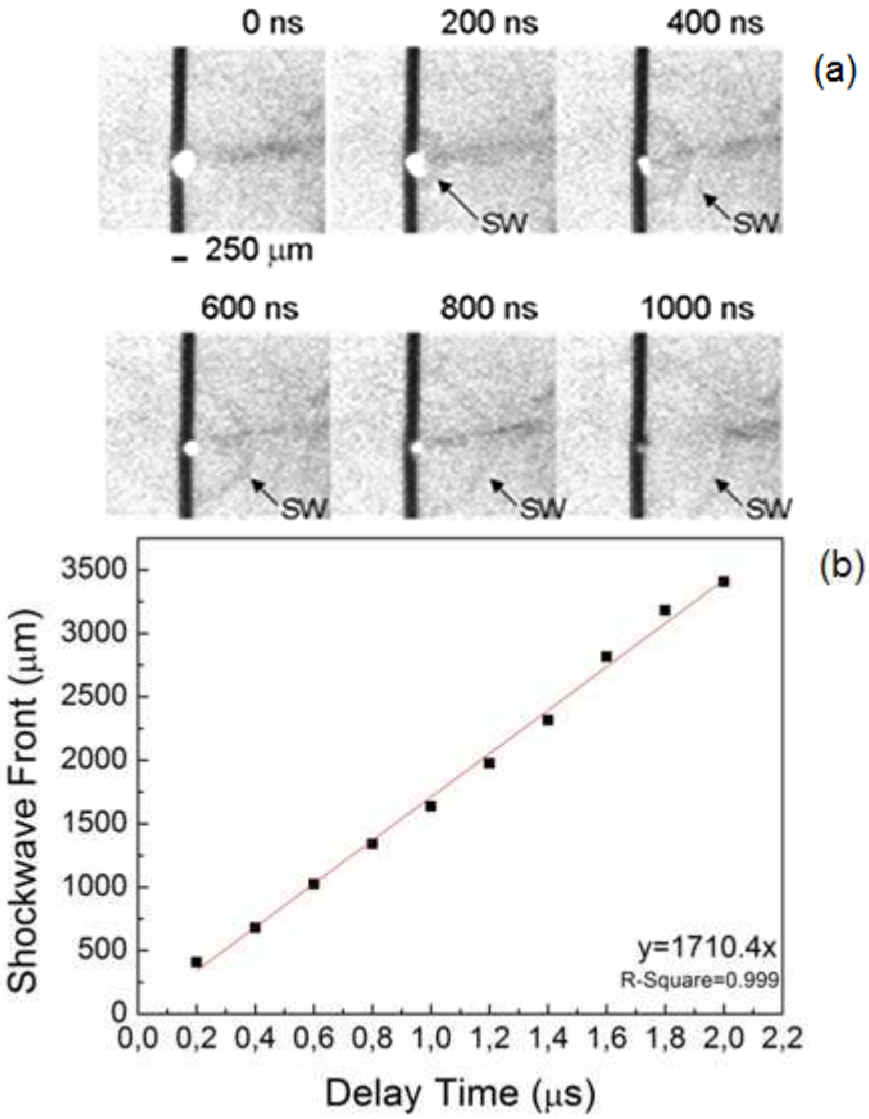

Figure 3.11 (a) Time-resolved shadowgraph images of shockwave front induced by laser focused on a Cu wire in water and (b) shockwave front space displacement vs. delay time plot. (Wire Diameter = 250 µm, Fluence 68 J/cm^2, gate width= 200 ns).

Fig. 3.11a-3.11b reports the images of the shockwave and the corresponding plot of space displacement as a function of time. It is visible how, in the time range of measurement, the shock wave has a constant propagation rate (1710 m/s) just slightly beyond the sound speed in water (which is Mach 1.14). This means that the shock wave propagation does not deliver enough energy to induce a transition phase as the maximum temperature of the water after the shock wave is around 320 K, as estimated by classical shock wave theory **[30]**.

It is possible to conclude that the outward shock wave does not play any significant role in the cavitation effect.

By time-resolved plasma images it has been observed that plasma reaches the maximum emission volume after few hundreds of nanoseconds. The plasma energy is suddenly transferred to the surrounding liquid, thus inducing a phase transition and the formation of a thin layer of vapour around the plasma volume, representing the starting point of the cavitation bubble.

As detected by vibrational studies, when the high temperature leads to the formation of the vapour layer, it reaches high pressure that compress both the plasma back to the target, both the surrounding water **[31]**. To investigate the characteristics of the laser induced plasma, optical emission spectroscopy measurements have been carried out.

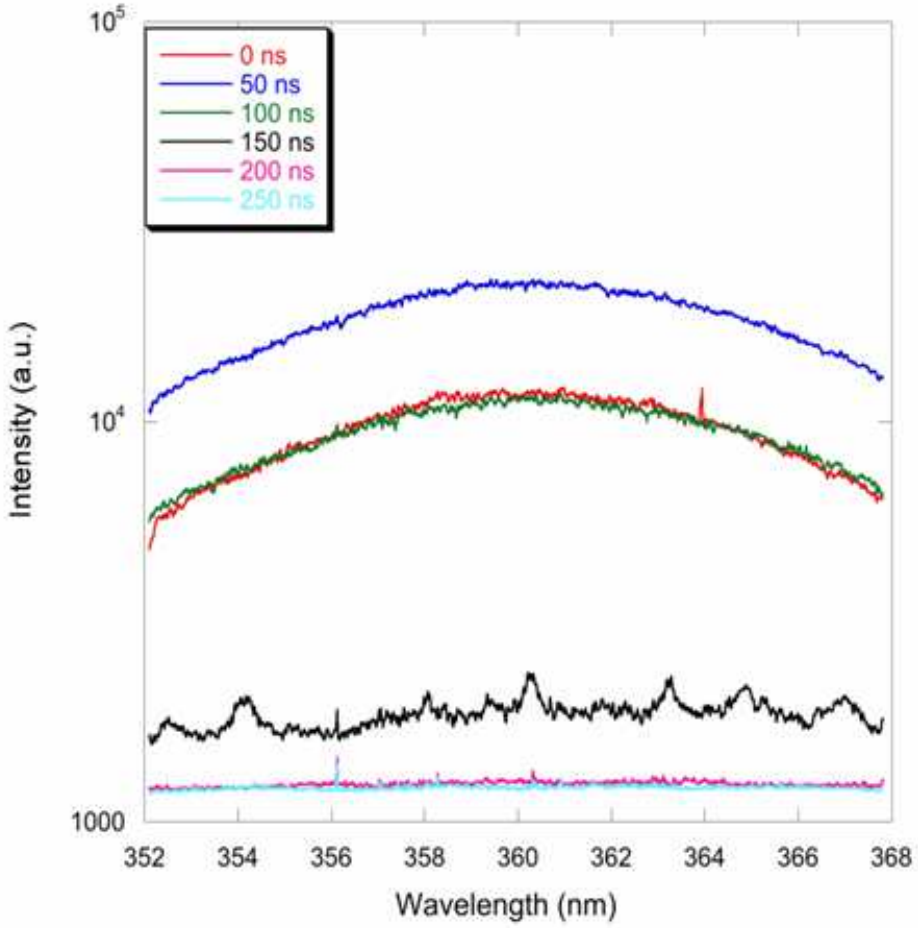

Figure 3.12 Temporal evolution of a typical frame of plasma emission spectrum during laser ablation of bulk Ti in water.

In fig. 3.12 is reported the emission spectrum during the ablation of a titanium bulk target in water, which shows the presence of a strong continuum radiation. After 150 ns from the laser pulse it is also possible to observe atomic and ionic discrete peaks due to low energy transitions.

The continuum radiation is mainly due to radiative recombination of ions with electrons when the plasma is characterized by high number density (typically with N ranging from 10^{21} to 10^{19} cm^{-3} during ablation of metals **[32]**). It is possible to estimate the recombination time by following the variation of intensity of the continuum with the following equation **[33]:**

$$I(t) = a_1 \exp\left(-\frac{t-t_0}{t_1}\right) + a_2 exp\left(-\frac{t-t_0}{\tau_2}\right) \quad (3.12)$$

where I is the intensity, t_0 is the time corresponding to the peak emission, τ_1 is the electron-ion recombination time, τ_2 is the electron-atom attachment.

In this experiment, if the electron-atom attachment is neglected, the recombination time has been estimated to $\tau_1=10^{-7}$s, in agreement with previous literature referring to works performed in different environments **[34]**.

Fig. 3.13a and 3.13b show the temporal evolution of the continuum intensity and of the temperature as determined by a Planck-like distribution with the method described in detail in ref. **[32]**.

It can be seen that while the intensity reaches a maximum value after about 60 ns from the laser pulse and then decrease exponentially, the temperature presents approximately a constant value. This behaviour can be explained considering that the emission volume of the plasma reaches its maximum few tens of nanoseconds after the laser pulse and then it decreases as a consequence of the interaction of the laser induced plasma with the surrounding liquid and the initial cavitation effect already discussed.

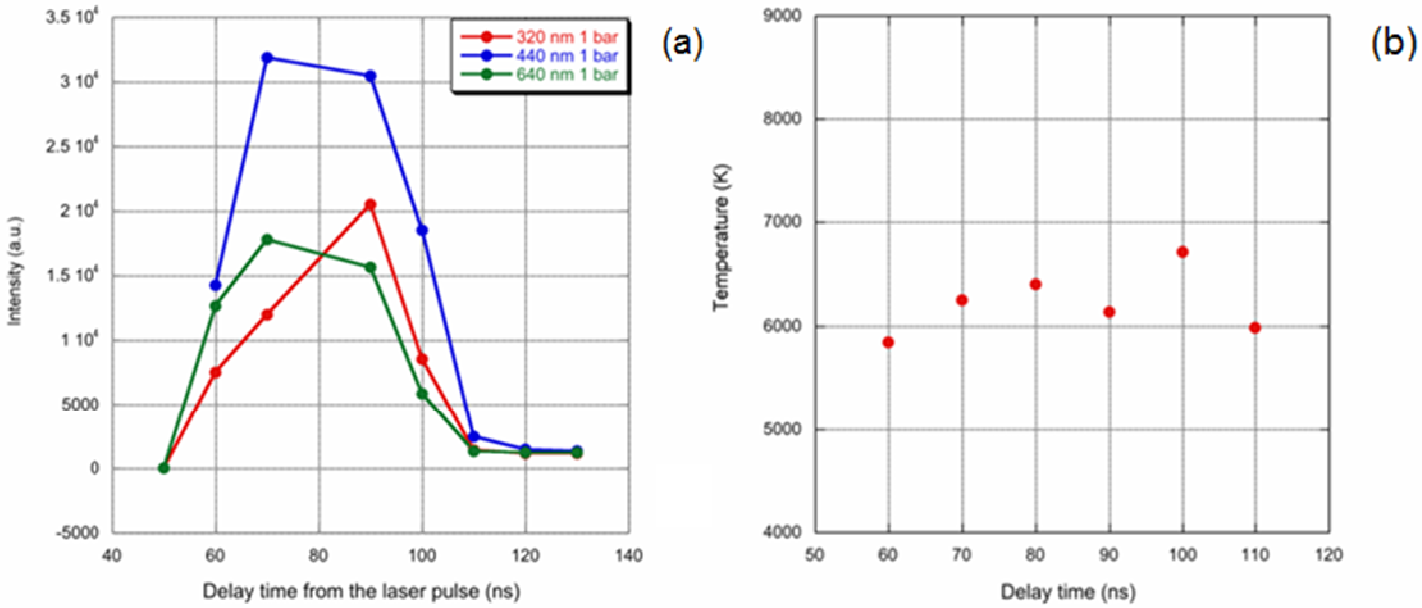

Figure 3.13 Temporal evolution of the (a) plasma continuum intensity and of the (b) plasma temperature as determined by a Planck-like distribution.

The recombination, while decreasing the electron number density and the total amount of electrons energy, at the same time delivers energy to heavy particles, so that the core of emitting plasma preserves its overall energy throughout its whole persistence time. Indeed, in laser induced plasmas, the electrons involved in recombination processes are mainly those with low energy, so that the bulk of the electron energy distribution function holds high temperature for long time **[35]**.

Although the duration of the plasma is longer than the time scale reported in fig. 3.13, the detected emission signal becomes too weak to perform a significant analysis of the data at longer delay times, because it is strongly compressed by the cavitation bubble. The intensity trend in fig. 3.13a and the imaging of figs. 3.11-3.12 indicate that whereas the plasma core holds a temperature around 6500 K, a fast cooling of the ablated material in the external part of the plasma should be expected, as a consequence of laser induced plasma front-head interaction with the surrounding liquid **[36]**. This material could grow in small nanoparticles and enable their transfer to the cavitation bubble. This transport of matter should be facilitated by the high number of instabilities generated at the boundary between the plasma and the backward expanding cavity. It should be also underlined that on the base of these results, the plasma behaviour does not seem to differ if a metal bulk target or a metal wire target is ablated. This is because the interaction of the metal with the laser, as well as the electron heating, are parameters which depend mainly on the laser features like energy, intensity and wavelength **[26,35]**.

3.6 CAVITATION BUBBLE INDUCED AFTER BULK ABLATION

As discussed above, the thin layer of vapour that grows around the plasma is initially characterized by high temperature and high pressure and, when expanding against the surrounding liquid, generates a cavitation bubble. The dynamic of the cavitation bubble includes an expansion stage and a subsequent shrinking, which can be repeated several times, reproducing a situation similar to damping oscillations **[36-40]**.

The pressure of the initial layer of vapour can be estimated determining its volume directly by the shadowgraph images and then assuming the number density of vapour as determined at later times by Van der Waals equation and the plasma temperature previously determined by optical emission spectroscopy. Assuming that the water vaporization due to the exchange of the energy between the plasma and the surrounding liquid is complete and that condensation during the expansion and collapse is negligible, this method gives an acceptable estimation. In the case of the laser irradiation with fluence of 6 J/cm^2 of metal targets such as silver, copper and titanium, this estimation gives an initial pressure of about 10^8 Pa.

During the oscillation period, the bubble reaches its maximum radius when the gas inside the bubble is in equilibrium with the surrounding liquid, that is the temperature of the bubble is approximately equal to that of the surrounding liquid and the pressure is equal to the saturation

pressure at that temperature. Under this condition, pressure inside the bubble (around 3000 Pa) is about two orders of magnitude lower than that of the liquid water, then the bubble is suddenly compressed and starts to contract. This shrinking stage is of fundamental importance in determining the process of particle production because part of the material can be pushed back to the surface of the target instead of being delivered into the solution.

Temporal resolved shadowgraph and laser scattering images of the cavitation bubble produced during the laser irradiation of a bulk target are shown in fig. 3.14. It is possible to observe the typical trend of the cavitation bubble near a solid boundary, which reproduces results already known by literature **[25,31,37]**.

In the specific case, it can be noted that the bubble rebound effect is very weak because a substantial amount of bubble energy is delivered to the target surface at the collapse, resulting in a new shock wave and in bubble fragmentation with the formation of smaller bubbles at the target surface **[38]**.

The low magnitude of the bubble rebound is mainly due to the asymmetric collapsing dynamics of the bubble in the presence of the boundary that could be strongly affected by the surface of the target, which is not perfectly smoothed, and by the spatial and temporal distortions of the laser pulse profile crossing the liquid.

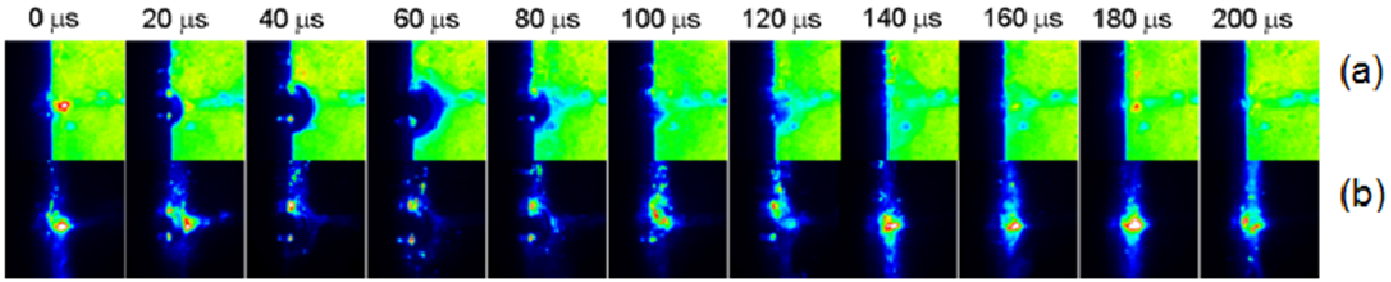

Figure 3.14 Temporal resolved (a) shadowgraph and (b) laser scattering images of laser induced bubble on a Ti bulk target in water at fluence of 203 J/cm^2 and a gate width of 20 µs.

From the scattering signal it is possible affirm that the produced particles, after the collapsing of the bubble, lay near the target surface. It is reasonable to state that part of the ablated material is deposited back on the target surface as a result of the bubble confinement and collapse. These hypotheses have been verified by mean of Scanning Electron Microscopy.

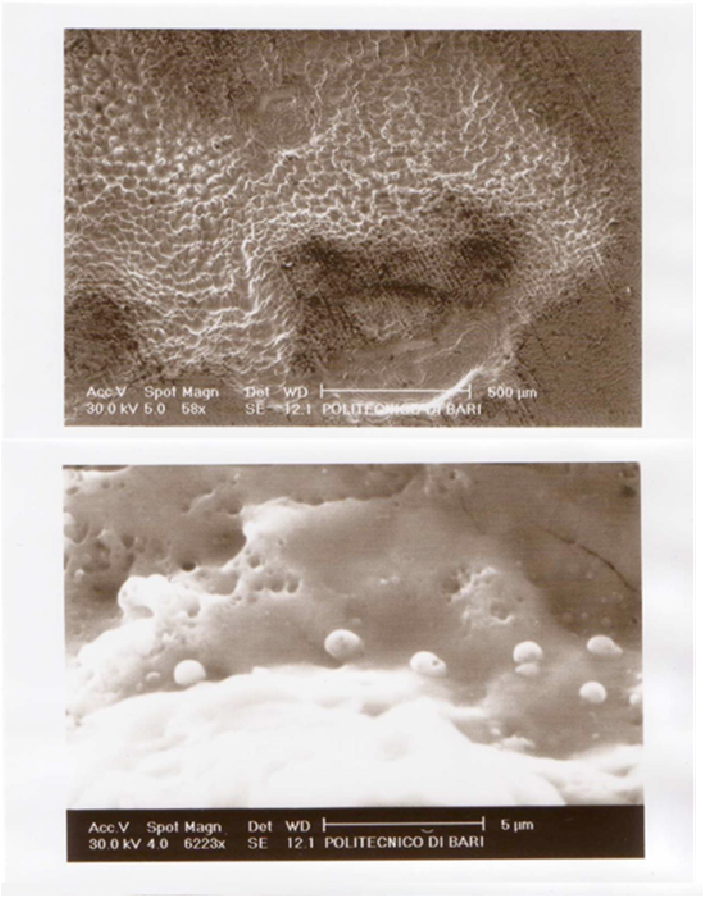

Figure 3.15 Deposited film of titanium oxide around the laser focus point on the target surface after ablation of metallic Ti in water.

In fig. 3.15 it is possible to note how the target surface around the focus point shows the presence of deposited titanium oxide after the ablation of metallic titanium in water, which presents the typical molten-like morphology including spherical particles.

Fast shadowgraph allows the determination of the bubble radius at each observation time and it enables to estimate the pressure and temperature in the bubble with the hard core Van der Waals models:

$$P(t) = \left(P_\infty + \frac{2\sigma}{R}\right)\left(\frac{R_\infty^3 - h^3}{R^3 - h^3}\right)^\gamma \tag{3.13}$$

$$T(t) = T_\infty \left(\frac{R_\infty^3 - h^3}{R^3 - h^3}\right)^{\gamma - 1} \tag{3.14}$$

where P_∞ and T_∞ are respectively the pressure and temperature of the liquid, R is the experimental radius determined as a function of the delay time from the laser pulse, R_∞ is the radius at which pressure inside the bubble corresponds to the liquid pressure, σ is the surface tension of the water, $h = R_\infty/9.174$ is the actual radius estimated taking into account the water molecules covolume, $\gamma = C_p/C_v = 1.22$.

A typical trend of evolution of temperature and pressure inside the cavitation bubble during its evolution is reported in fig 3.16a and 3.16b which shows that temperature reaches values higher than 1000 K and pressure reaches values in the order of 10^7-10^8 Pa. These values represent an underestimation in the time range around the inversion phase from collapse to rebound where much higher values may be expected.

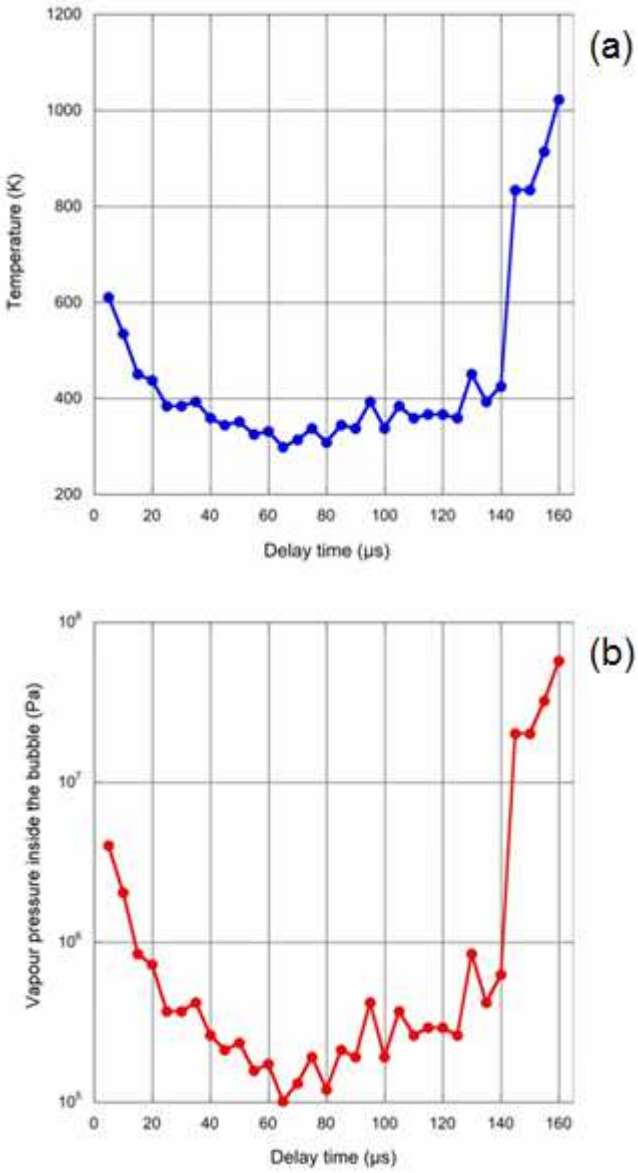

Figure 3.16 Typical trend of (a) temperature and (b) pressure inside the cavitation bubble calculated from data of fig. 3.11a, during its evolution after laser ablation of Ti in water.

Indeed, in this time interval changes of the bubble radius occur on a nanosecond timescale so that using a detection system with a gate width of hundreds of nanoseconds (such as the one used in this work) causes the detected radius to be averaged over the whole gate width.
In this way, the peaks of pressure and temperature at the exact collapse time result smoothened by the time integration. This question has been discussed in literature **[41]**, where a theoretical model has been presented for studying the bubble inversion stage. The results of this model show that at the collapse the temperature of the bubble interior is between 5000 K and 10000 K while the pressure reaches several thousands of MPa. These extreme values confirm that the collapsing of the bubble is responsible for the deposition of the material on the surface of the target, as well as of the formation of structures showing the typical molten-like features.

3.7 WIRE BUBBLE DYNAMICS

It seems appropriate to state that the back deposition of ablated material could be a limit for the productivity, because less material is released into the liquid after the laser-induced cavitation, assuming that the larger amount of material is trapped inside the cavitation bubble which has to release the material into the liquid in order to form colloidal nanoparticles. It is possible that the back deposition effect could be reduced changing the bubble dynamics and in particular changing the

target shape. In fig. 3.17a-3.17b the shadowgraph and laser scattering images of the ablation of a Cu wire with a diameter of 250 μm in water. The images show the typical feature of a cavitation bubble as discussed previously for bulk ablation, but the cavitation bubble generated in this case presents substantial differences: the cavitation bubble expansion appears spherical in the case of wire and semi-spherical in the case of bulk targets, the material delivered after the bubble collapse is ejected farther in the case of wire ablation with respect to bulk target ablation where the scattering material lies near the target surface. Also, fig. 3.17a shows that at the bubble rebound and after the bubble collapse (which at 120 μs in this experiment), a sort of "sucking effect", with a pressure sink in the back region of the off-propagating bubble, of the daughter bubbles and particles can take place. Such drastic bubble ejection has never been observed during laser ablation of a bulk target. The temporal frames around 120 μs (fig. 3.17b) clearly show that particles are ejected in a mushroom-shaped jet after the bubble collapse and rebound. It has been previously demonstrated that at the collapse of the first cavitation bubble a high amount of energy is suddenly delivered to the target surface and surrounding material, due to the very high temperature and pressure reached by the vapour in the shrinking bubble. In the case of bulk ablation two main effects can be hypothesized: the agglomeration of small nanoparticles in bigger particles and the back-deposition of part of this material to the target surface. In the case of the wire geometry, it appears that the latter effect is more limited as a consequence of the different bubble dynamics.

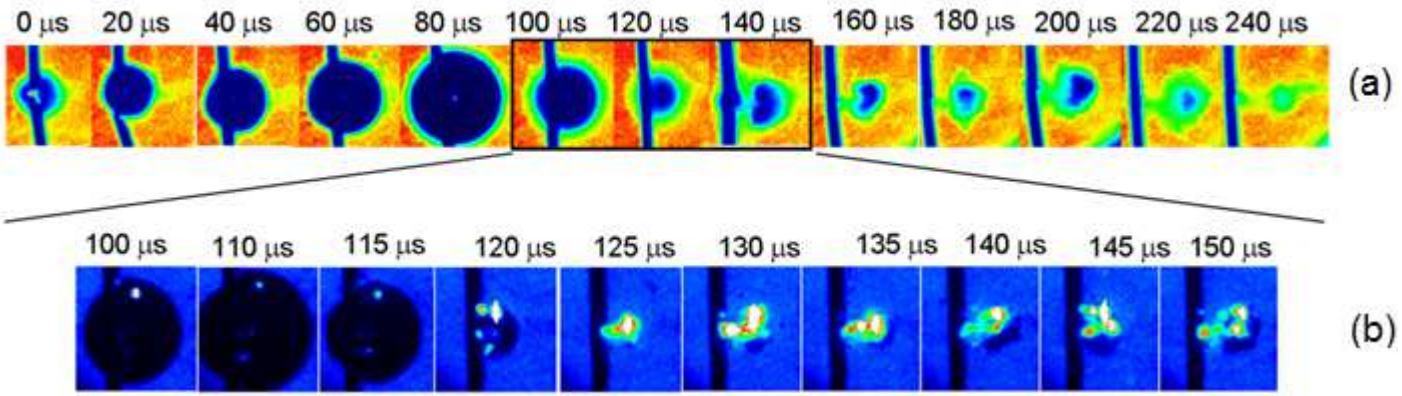

Figure 3.17 Time-resolved (a) shadowgraph and (b) scattering images of laser-induced cavitation bubble on Cu wire in water with wire diameter of 250 µm at a fluence of 68 J/cm^2 and a gate width of 5 µs.

During the expansion phase the vapour expands isotropically and wraps around the wire as shown in fig. 3.18, where a shadowgraphic frame at the maximum of the bubble expansion was acquired along the direction of the wire itself. This dynamics of the wire-bubble system resembles the behaviour of a bow shooting an arrow. The wire is the main pivot and, right before the bubble collapse, when the bubble-wire system strain at its maximum, the bubble is pushed away from the target.

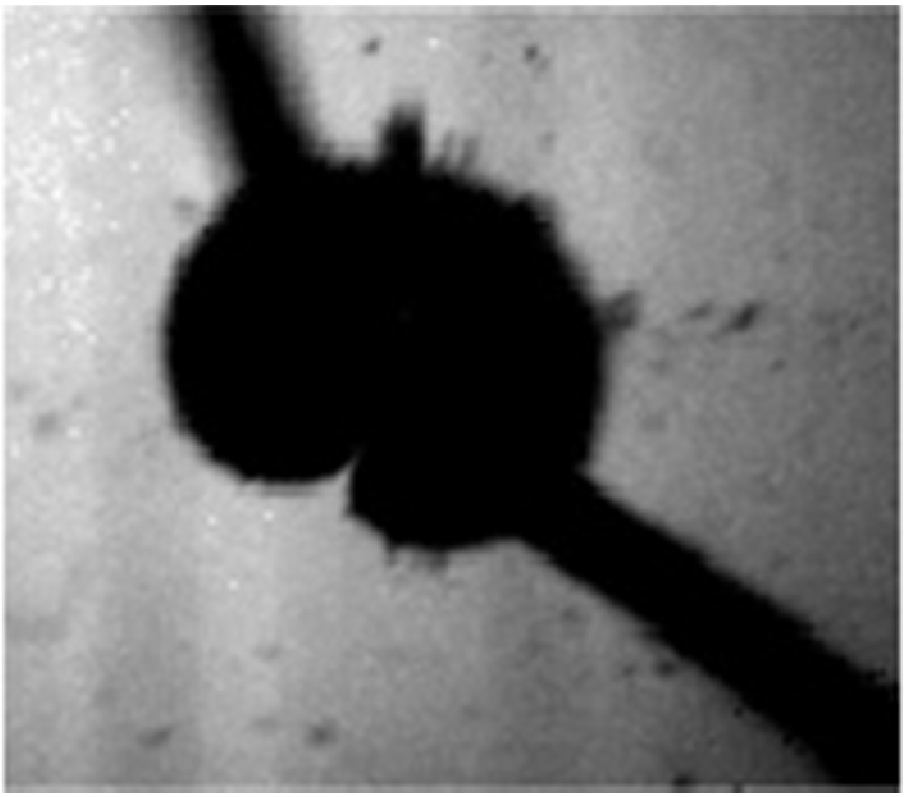

Figure 3.18 Shadowgraph frame at the maximum of the bubble expansion collected in the direction parallel to a Cu wire with 250 μm diameter.

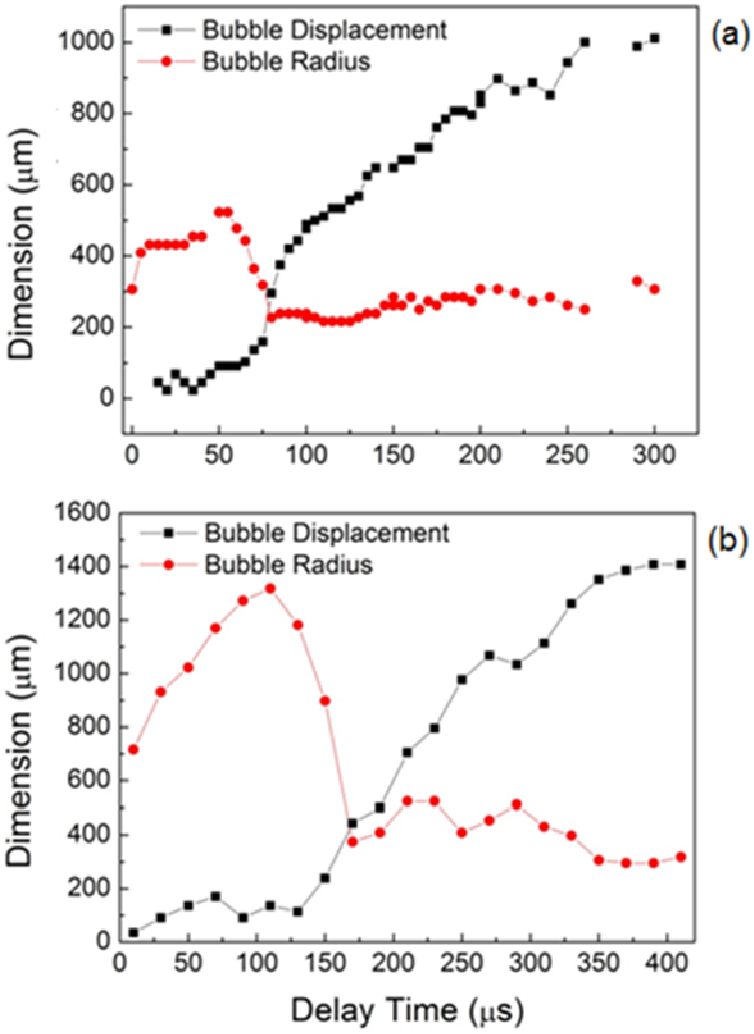

Figure 3.19 Radius and displacement temporal evolution of laser induced bubble on (a) Ag wire in water, measured from shadowgraph images at a fluence of 0.9 J/cm^2 and a gate width of 5 μs (b) Fe alloy wire in water, measured from shadowgraph images at a fluence of 68 J/cm^2 and a gate width of 5 μs.

The displacement of the bubble from the wire and the subsequent carrying of material far from the target are plotted as a function of time in fig. 3.19. The displacement causes a variation of the shape of the bubble which is no longer spherical but acquires a more hydrodynamic shape as reported in fig. 3.20.

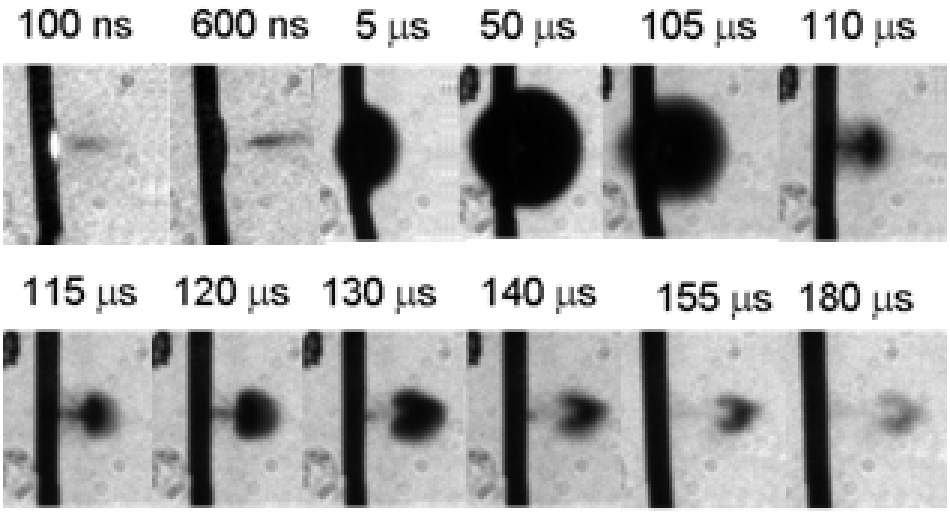

Figure 3.20 Time-resolved shadowgraph images of laser induced bubble on Ag wire in water at a fluence of 1.4 J/cm^2 and a gate width of 5 μs.

Fig. 3.21 shows the effect of the wire diameter on the cavitation bubble dynamics. As the diameter increases, the wrapping around the wire becomes less significant, until reaching the hemispherical shape in the case of the bulk target, which could be considered approximately as a wire of infinite diameter.

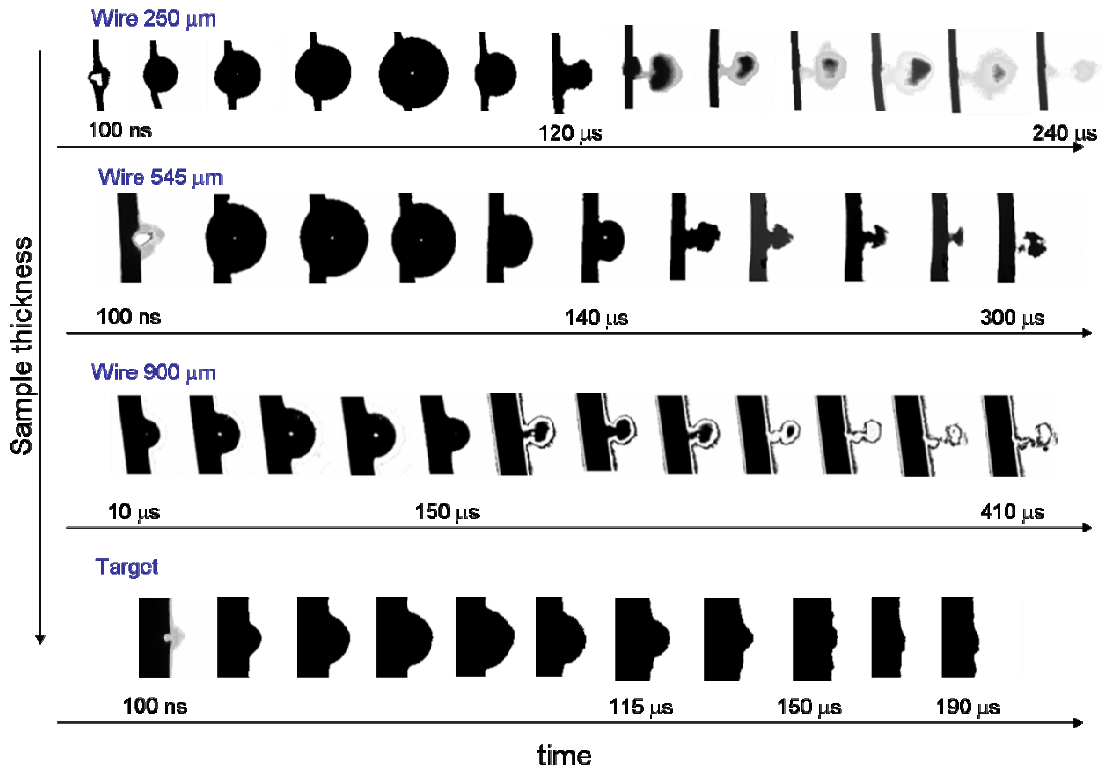

Figure 3.21 Time-resolved shadowgraph images of laser induced bubble on samples with different thickness submerged in water at a fluence=68 J/cm^2 and a gate width of 5 µs

This consideration is fundamental when describing ablation efficiency reported in fig. 3.8

Considering that the passage to cavitation bubble behaviour typical of a bulk target can be observed for a wire diameter of around 1 mm, this is in accordance with the maximum efficiency at 750 μm reported in fig. 3.8. For upper wire diameters, the ablation efficiency asymptotically approaches the bulk behaviour. It is possible to suppose that the formation of a larger cavitation bubble involves the consumption of a higher amount of energy, which is not used for ablating material from the target.

By the analysis of the images reported in fig. 3.21, it is possible to estimate the speed of the ejected material after the bubble collapsing, the duration of the first bubble oscillation, consisting of expansion and collapse stage, and the maximum bubble radius.

These data, reported in tab 3.1, show that with the thinnest wire, the elastic dynamic effect, which pushes the bubble away from the wire, appears more efficient than for thicker wires. The speed of bubble center is far higher the thinner (~9 m/s in the case of a 250 μm wire) than for the ticker wire (~5 m/s for a 900 μm wire). This in agreement with the trend of energy dissipation into the volume of larger bubbles.

Wire Thickness	Speed o f Bubble Center After Bubble Collapse	Collapse Time	Maximum Distance Reached by the Bubble Center Before the Slowing Down	Maximum bubble radius
250 µm (Cu)	9.278 m/s	120 µs	1150 µm (at 200 µs)	830 µm (at 50 µs)
545 µm (Pt)	7.253 m/s	140 µs	1103 µm (at 300 µs)	1170 µm (at 75 µs)
900 µm (Fe)	5.278 m/s	170 µs	1353 µm (at 350 µs)	1301 µm (at 100 µs)

Table 3.1 Bubble parameters obtained from time resolved shadowgraph images of laser induced bubble on Cu, Pt and Fe wires in water (Fluence = 68 J/cm^2, gate width= 5 µs)

The maximum bubble radius results larger for thicker wires. This is due to the fact that, although the total volume of the bubble does not change noticeably, its shape turns from spherical to hemispherical. Thus increases the minimal radius and cause to decrease the detachment impetus of the bubble in the rebound phase.

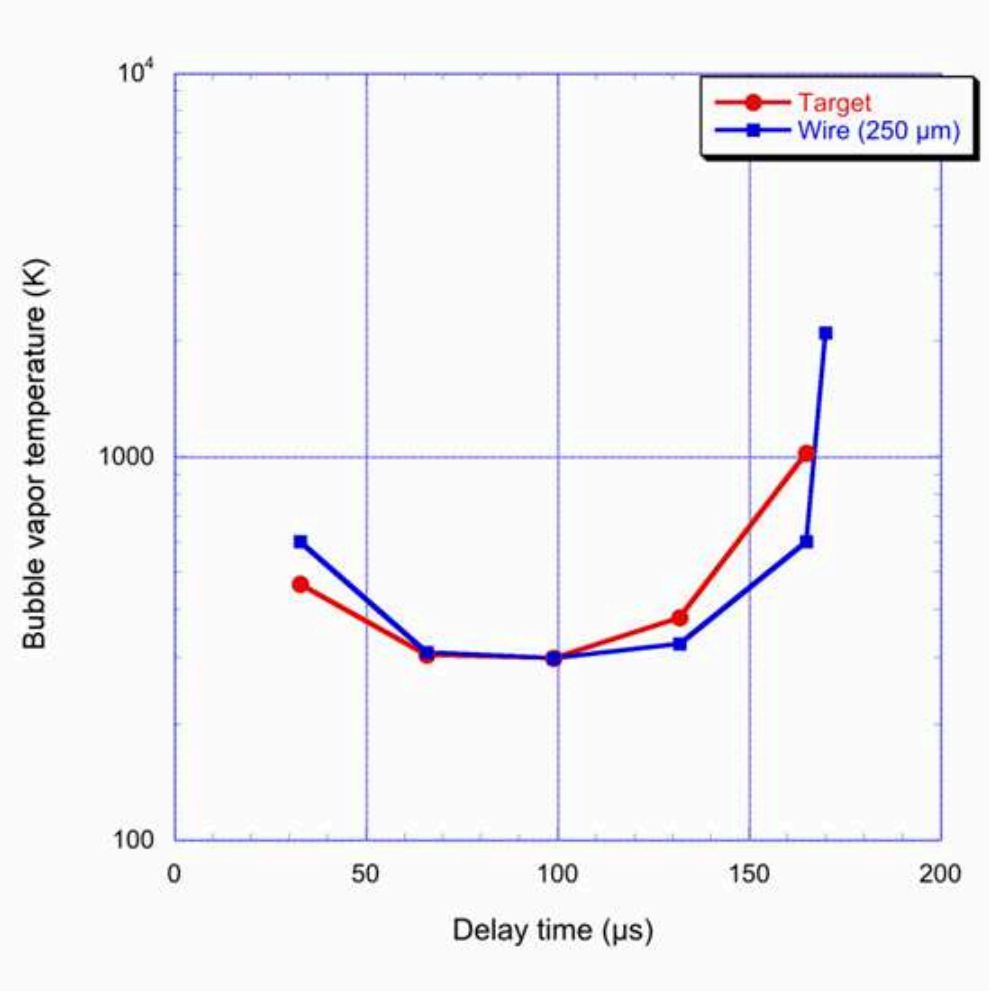

Figure 3.22 Temporal evolution of laser-induced bubble vapour temperature on Ag wire and bulk target in water.

Fig. 3.22 reports the comparison of the bubble pressure and temperature during the first oscillation period as determined by eqs. (3.13)-(3.14) for the different targets. As it can be observed there are no substantial differences between bulk and wire ablation, because the initial energy input is the same in both cases and the plasma temperature mainly depends on the wavelengths of laser photons and their absorption by electrons. So, it appears that the bubble dynamics is significantly altered by the shape of the target, while thermodynamic parameters of the vapour are unaffected.

3.8 EFFECT OF LASER ENERGY

The effect of the laser energy on the bubble radius is reported in fig. 3.23 where the bubble dynamics of laser ablation on a silver wire with a 250 μm diameter is compared at two different fluencies.

At higher fluence the bubble lifetime is longer and the bubble reaches larger volume in agreement with the following equation **[42]**:

$$R_{MAX} = \frac{t_{collapse}}{0.915\sqrt{\rho/(P_\infty - P_v)}} \qquad (3.15)$$

Where R_{MAX} is the radius at the maximum bubble expansion, ρ is the density of fluid, $t_{collapse}$ is the collapse time of the bubble P_∞ is the liquid pressure and P_v the vapour saturation pressure inside the bubble.

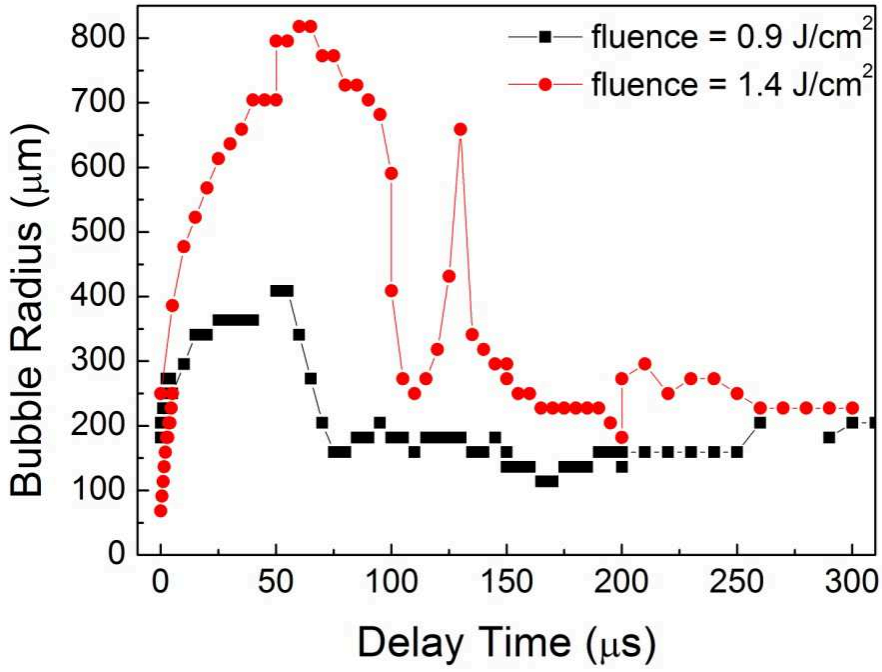

Figure 3.23 Temporal evolution of laser-induced bubble radius on Ag with a diameter of 250 μm diameter in water measured from shadowgraph images, at two different laser fluencies (0.9 and 1.4 J/cm^2) with a gate width of 5 μs.

These observations can be explained considering that at higher fluence, as already shown in fig. 3.7, a higher amount of material is ablated from the target, and this causes the enlargement of the plasma volume and the plasma/water boundary. This implies that a greater amount of initial vapour is formed and, in turn, and increasing of the expansion time and the bubble volume.

Fluence (J/cm^2)	R_{MAX}(μm)	$t_{collapse}$ (μs)
Cu-bulk target		
57.7	1008.8	294
99.5	1317.6	385
Cu-wire target		
4.0	226.5	66
13.9	617.6	181
70.7	720.6	211
137.3	741.2	217

Table 3.2 Radius at maximum of bubble expansion and the corresponding collapse time as calculated by eq. 3.13 as function of fluence during Cu bulk and wire ablation in water.

Tab. 3.2 reports the maximum bubble radius as function of fluence for the ablation of a copper bulk target and wire, confirming qualitatively what already discussed.

Quantitatively, it can be seen that the bubble radius does not scale linearly with the fluence. Indeed an increase of fluence from 4 to 137 J/cm^2, that represents a factor 34, only causes a triplication (particularly 3.3) of both bubble diameter and time interval until the collapsing of the bubble.

It is important to underline that in eqs. (3.13) and (3.14) there is no term taking into account the fluence variation, and the determined pressure and temperature of the bubble result unaffected. This is because pressure

and temperature are intensive variables, and so they are determined mainly by the plasma internal energy. As it has been mentioned in section 3.5, in the case of nanosecond laser, plasma internal energy depends on the effective absorption of laser photons by free electrons immediately after the ablation (Inverse Bremsstrahlung). In the range of fluence employed in this work (0.1-100 J/cm^2), the electron temperature can be considered influenced only by the photon energy, that means by the laser wavelength.

Considerations about pressure and temperature conditions of the cavitation bubble have been confirmed by experimental results.

Fig. 3.24 reports the size distribution of silver nanoparticles prepared by wire ablation at different fluencies. As it is possible to notice, the size distribution based on SEM images evaluate that nanoparticles present a size of around 15-20 nm.

These size values are similar to those found in the case of silver nanoparticles prepared by laser ablation of a bulk target **[43]**.

Since literature reports that the temperature of the cavitation bubble strongly affect the properties of produced nanoparticles **[44]**, The absence of difference between nanoparticles prepared by laser ablation of wire target and laser ablation of bulk target confirm that temperature and pressure conditions inside the cavitation bubble are not influenced by the target geometry, as demonstrated in section 3.7.

Moreover, when working with wire, size distributions do not depend on the used fluence.

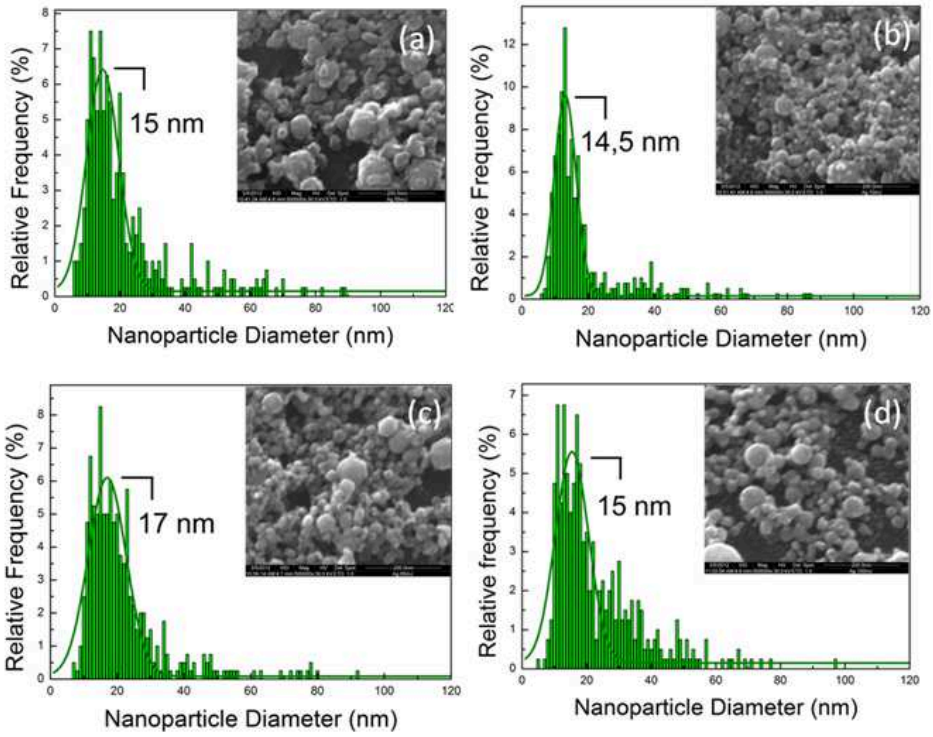

Figure 3.24 Size distributions of silver nanoparticles prepared by laser ablation of a wire with a diameter of 250 μm at a repetition rate of 100 Hz and a fluence of (a) 0.8 J/cm^2, (b) 1.0 J/cm^2, (c) 1.2 J/cm^2 and (d) 1.5 J/cm^2.

It has been demonstrated that variation of fluence influences the radius and dimension of the cavitation bubble due to wire ablation, but not its thermodynamic parameters, which are intensive variables. For this reason, nanoparticles prepared by wire ablation presents the same size distribution in the used fluence range.

3.9 EFFECT OF REPETITION RATE

To harvest the increase in ablation efficiency as increased nanoparticle productivity, it is necessary to scale-up by suitable process parameters. As reported in literature **[45]**, nanoparticles productivity scales linearly with repetition rate in the case of bulk targets.

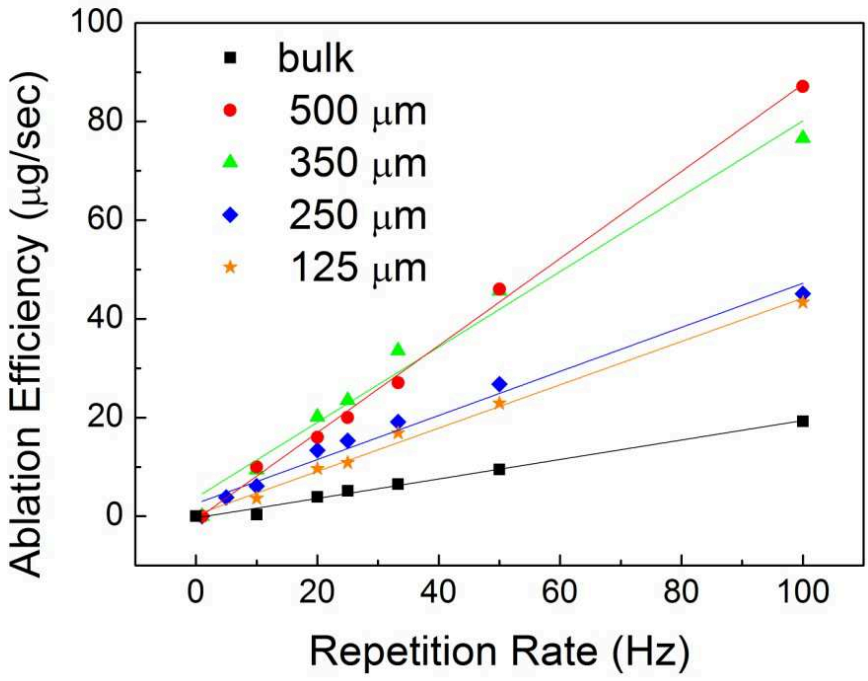

Figure 3.25 Nanoparticle productivity in dependence of the repetition rate for wire and bulk targets.

Fig. 3.25 reports ablation efficiency as a function of the repetition rate, for different wire diameters and for bulk target.

In the range of repetition rate used (from 1 to 100 Hz) wires with different diameters present the same linear behaviour of the bulk target. For a bulk target, it has been shown that shielding of laser pulses and subsequent reduction of ablation efficiency had to be taken in account if the temporal distance between two laser pulses is in the regime of the lifetime of the cavitation bubble **[45]**. As can be seen by fig. 3.17, the total lifetime of the cavitation bubble using a 250 μm diameter wire is about 250 μs which is in good agreement with literature values for a bulk target **[25]**, thus an increase of the number of pulses will lead to an increase of the material removed from the target **[46]**.

The increase of productivity should remain linear till the temporal distance between two consecutive shots is greater than the bubble duration. Further, double pulses experiments have demonstrated that the amount of ablated material is higher respect to a single pulse **[47]**.

It was demonstrated that for interpulse delays $\Delta t > 1$ μ, the existing plasma does not interact with the second laser pulse but it is essentially transparent to it **[36]**.

Similar considerations have been already been reported in literature in the case of bulk targets **[48]**.

Considering the 300-500 μs limit, it is possible to affirm that the linear behaviour will be maintained within the use of a repetition rate of around 2 kHz. At higher repetition rates there will be a shielding effect due to the material ejected from the target. Consequently, the optimization of different parameters, such as fluence, wire target dimension and repetition rate will lead to a maximum of the ablation efficiency, in order

to obtain values of efficiency competitive with chemical synthesis technique.

REFERENCES

[1] S.M. Lee, D. Kim, D.Y. Jeon, K.C. Choi, *Small*, 2012, **8**, 1350-1354

[2] X. Chen, B.H. Jia, J.K. Saha, B.Y. Cai, N. Stokes, Q. Qiao, Y.Q. Wang, Z.R. Shi, M. Gu, *Nanolett.*, 2012, **12**, 2187-2192

[3] A. Hu, J.Y.Guo, H. Alarifi, G. Patanè, Y. Zhou, G. Compagnini, C. X. Xu, *Appl. Phys. Lett*., 2010, **97**, 153117

[4] P. Wagener, G. Brandes, A. Schwenke, S. Barcikowski, *Phys Chem. Chem. Phys.,* 2011, **13,** 5120-5126

[5] G. Compagnini, M. E. Fragalà, L. D'Urso, C. Spinella, O. Puglisi, J Mater. Res., 2001, **16**, 2934-2938

[6] C.L. Sajti, S. Petersen, A.Menendez-Manjon, S. Barcikowski, *Appl. Phys. A*, 2010, **101**, 259-264

[7] H. Ferkel, J. Naser, W. Riehemann, *Nanostruct. Mater.* 1997, **8**, 457-464

[8] J. Naser, H. Ferkel, *Nanostruct. Mater.* 1999, **12**, 451-454

[9] X.-C. Yang, W. Riehemann, *Scr. Mater.*, 2001, **45**, 435-440

[10] C. L. Sajti, R. Sattari, B. N. Chichkov, S. Barcikowski, *J. Phys. Chem. C*, 2010, **114**, 2421–2427

[11] Y. Jiang, P. Liu, Y. Liang, H.B. Li, G.W. Yang *Appl Phys A,* 2011, **105,** 903–907

[12] S. Barcikowski, A. Menéndez-Manjón, B. Chichkov, M. Brikas, G. Račiukaitis, *Appl. Phys. Lett*., 2007, **91**, 083113

[13] C.B. Juang, H. Cai, M.F. Becker, J.W. Keto, J.R. Brock, *Appl. Phys. Lett.*, 1994, **65**, 40-42

[14] C.B. Juang, H. Cai, M.F. Becker, J.W. Keto, J.R. Brock, *Nanostruct. Mater.*, 1994, **4**, 569-575

[15] J. Lee, M.F. Becker, J.R. Brock, J.W. Keto, R.M. Walser, *IEEE Trans. Magn.*, 1996, **32**, 4484-4486

[16] H. Cai, N. Chaudhary, J. Lee, M.F. Becker, J.R. Brock, J.W. Keto, *J. Aerosol Sci.*, 1998, **29**, 627-636

[17] M.F. Becker, J.R. Brock, H. Cai, D.E. Henneke, J.W. Keto, J. Lee, W.T. Nichols, H.D. Glicksman, *Nanostruct. Mater.*, 1998, **10**, 853-863

[18] X. Zeng, Z. Wang, Y. Liu, M. Ji, *Appl. Phys. A*, 2005, **80**, 581–584

[19] T. Tsuji, K.Iryo, Y. Nishimura, M. Tsuji, *J. Photochem. Photobiol. A*, 2001, **145**, 201-207

[20] S. Noël, J. Hermann, T.E. Itina, *Appl. Surf. Sci.*,2007, **253**, 6310-6315

[21] J. Hermann, S. Noël, T. E. Itina, E. Axente, M.E. Povarnitsyn, *Laser Physics*, 2008, **18**, 374–379

[22] A. Schwenke, P. Wagener, S. Nolte, S. Barcikowski, *Appl. Phys. A*, 2011, **104**, 77-82

[23] P. Wagener, A. Schwenke, B.N. Chichkov, S. Barcikowski,*J. Phys. Chem. C,* 2010, **114**, 7618–7625

[24] P. Lorazo, L.J. Lewis, M. Meunier, *Phys Review B*, 2006, **73**, 134108

[25] T. Tsuji, Y. Okazaki, Y. Tsuboi, M. Tsuji, *Jpn. J. Appl. Phys.*, 2007, **46**, 1533–1535

[26] A. De Giacomo, M. Dell'Aglio, R. Gaudiuso, S. Amoruso, O. De Pascale, *Spectrochim. Acta B*, 2012, **78**, 1-19

[27] P. Peyre, L. Berthe, X. Scherpereel, R. Fabbro, *J. Mater. Sci.*, 1998, **33**, 1421-1429

[28] L. Berthe, A. Sollier, P. Peyere, R. Fabbro, E. Bartniki, *J. Phys. D*, 2000, **33**, 2142-2145

[29] A. De Giacomo, M. Dell'Aglio, R. Gaudiuso, G. Cristoforetti, S. Legnaioli, V. Palleschi, E. Tognoni, *Spectrochim. Acta B*, 2008, **63**, 980-987

[30] J.D. Anderson, Jr., "Hypersonic and High Temperature Gas Dynamics", Series in Aeronautical and Aerospace Engineering, McGraw Hill: New York, 1989, pp.213-259 and 611-636

[31] A. De Giacomo, M. Dell'Aglio, O. De Pascale, M. Capitelli, *Spectrochim. Acta B*, 2007, **62**, 87-93

[32] A. De Giacomo, R. Gaudiuso, M. Dell'Aglio, A. Santagata, *Spectrochim. Acta B*, 2010, **65**, 385-394

[33] P.K. Kennedy, D.X. Hammer, B.A. Roclwell, *Prog. Quant. Electr.*, 1997, **21**, 155-248

[34] A. Casavola, G. Colonna, A. De Giacomo, O. De Pascale, M.Capitelli, *Appl. Optics*, 2003, **42**, 5963-5970

[35] A. De Giacomo, *Spectrochim. Acta B*, 2011, **66**, 661-670

[36] A. Casavola, A. De Giacomo, M. Dell'Aglio, F. Taccogna, G. Colonna, O. De Pascale, S. Longo, *Spectrochim. Acta B*, 2005, **60**, 975-985

[37] K. Sasaki, N. Takada, *Pure Appl. Chem.*, 2010, **82**, 1317-1327

[38] W. Lauterborn, T. Kurz, *Rep. Prog. in Phys.*, 2010, **73**, 106501

[39] W. Soliman, N. Takada, K. Sasaki, *Appl. Phys. Express*, 2010, **3**, 035201

[40] R. Petkovsek, P Gregoricic, *J. Appl. Phys*., 2007, **102**, 044909

[41] I. Akhatov, O. Lindau, A. Topolinkov, R. Mettin, N. Vakhitova, W. Lauterborn, *Phys. Fluids*, 2001, **13**, 2805-2819

[42] X. Chen, R.Q. Xu, Z.H. Shen, J. Lu, X.W. Ni, *Opt. Laser Technol.*, 2004, **36**, 197-203

[43] E. Messina, G. Compagnini, L.D'Urso, O. Puglisi, S. Bagiante, S. Scalese, *Radiat. Eff. Defect. S.,* 2010, **165**, 579-583

[44] A.Menéndez-Manjón, B.N. Chichkov, S. Barcikowski, *J. Phys. Chem. C*, 2010**, 114***,* 2499–2504

[45] P. Wagener, A. Schwenke, B.N. Chichkov, S. Barcikowski, *J. Phys. Chem. C,* 2010, **114**, 7618–7625

[46] M. Hashida, A.F. Semerok, O. Gobert, G. Petite, Y. Izawa, J.F. Wagner, *Appl. Surf. Sci.*, 2002, **862**, 197–198

[47] A. De Giacomo, M. Dell'Aglio, F. Colao, R. Fantoni, *Spectrochim. Acta B*, 2004, **59**, 1431-1438

[48] C.L. Sajti, R. Sattari, B. Chichkov, S. Barcikowski, *Appl. Phys. A*, 2010, **100,** 203-206

CHAPTER 4: INDUCED AND SPONTANEOUS JOINING OF METAL NANOPARTICLES

4.1 INTRODUCTION

The unusual optical properties given by the collective oscillation of surface electrons to metal nanoparticles are so intriguing that a whole new branch of photonics has been dedicated to their study. This new field of research, not surprisingly called plasmonics, deals with the manipulation of light on the nanoscale by using the extended and localized properties of surface plasmon resonances **[1]**.

Particular interest has been dedicated to the local field enhancement observed on the surface of a nanoparticle when an electromagnetic wave interacts with it. This behaviour has been attributed to two processes: the crowding of electronic field lines at a sharp metallic tip and the excitation of localized surface plasmon at a metal surface **[2]**.

This effect can find different applications such as Surface Enhanced Raman Scattering (SERS) **[3]**, biosensing **[4]** or nanoantennas **[5]**.

In order to optimize the amplification of electromagnetic fields, there have been several efforts in designing metal nanostructures with different morphologies.

Literature reports the fabrication of metal island films **[6]**, large silver and gold colloids **[7]**, silver triangle arrays **[8]** silver and gold nanoshells **[9]** and silver fractal films **[10]**.

In the case of spherical metal nanoparticles, it has been demonstrated that the strong accumulation of charge in the gap between two of them leads to an enhancement of the near field larger than the sum of the enhancements for individual nanospheres **[9,11-12]**.

Since the fabrication of pure surface spherical nanoparticles can be easily obtained by laser ablation in liquid, an efficient and simple approach could be based on the creation of nanoscale gaps between two or more nanoparticles.

Discussing the issue of the simplest geometry, that is two spherical nanoparticles with a nanoscale gap or two closely spaced nanoparticles, also called dimers, it is possible to talk about plasmon hybridization **[13]**, that it means considering the dimer plasmon as the hybrid of the plasmon of two single nanoparticles.

The plasmon shown by the dimer is polarized **[11-12,14-15]** and in particular, for polarizability perpendicular to the interparticle axis of the dimer, the hybridized plasmon is blue-shifted with respect to the single particle plasmon, while for incident polarization parallel to the dimer axis, there is a strong hybridization of the sphere plasmon and the symmetric plasmon shows a continuous red-shift as the gap between the sphere decreases. This behaviour has been observed in the case of dimers with well defined size and distance, obtained by electron beam lithography **[11,14-15]**.

4.2 AGGREGATION PHENOMENA IN SILVER NANOPARTICLES JOINED THROUGH HIGHLY CONJUGATED CARBON CHAINS

One of the approaches to modify the surface plasmon resonance contemplates the joining of metallic nanoparticles by the use of different molecular entities. This is of particular interest since it allows joining their properties avoiding the direct contact of them **[16]**.

Literature reports examples of dimers obtained by using DNA spacers at fixed distances **[17]**, or by functionalization with thiol ligands **[18]**.

Since their peculiar electronic properties, which point at them as potential molecular wires [**19-22**], good candidates as binding molecules are represented by linear carbon chains, metastable structure with *sp* hybridization.

Due to the high conjugation of the π electron system, such systems coexist in two different forms: polyynes, which present carbon atoms connected by alternating single and triple bonds and less stable structures in which carbon atoms are connected by double bonds, called cumulenes **[23]**.

Scientific interest has risen around these compounds, since the hypothesis of being forerunners of fullerenes **[24]** and nanotubes [**25-26**].

4.2a Laser Ablation of Carbon

The production of these entities can be easily obtained by laser ablation of a graphite target in water **[27]** or other solvents **[28]**.

It is well known that the formation of the high temperature (4000-5000 K) and high pressure (10-15 GPa) plasma environment during ablation of graphite **[29]** is favorable to the formation of metastable carbon phases, that are situated in the high temperature and high pressure zone of the carbon phase diagram, and that can be quenched by the cooling down of the plasma.

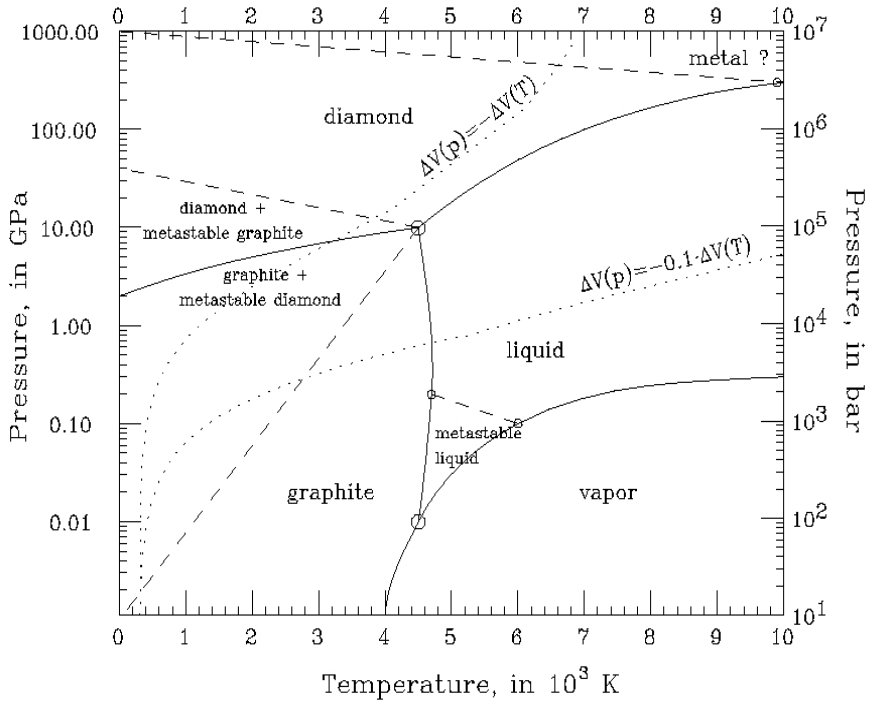

Figure 4.1 Carbon phase diagram. From ref. **[30]**.

Indeed, diamond particulate with cubic structure has been obtained by ruby laser ablation of pyrolytic graphite in benzene **[31]**, while diamond nanoparticles have been obtained by Nd:YAG irradiation of graphite in water, cyclohexane **[32]** and acetone **[33]**.

Moreover, also non-conventional carbon nanostructures have been obtained by laser ablation of graphite target like nanotubes **[34-35]**, nanofoam **[36]**, fullerenes **[37]** and carbon nanowalls **[38]**.

Formation of polyynes in liquid has been explained by a polymerization and hydrogenation mechanism of C_2 and C_2H radicals **[28]**.

Mechanism has been rationalized with the following scheme:

$x\ C_2 \rightarrow C_{2x}$

$C_{2x} + H \rightarrow C_{2x}H$

$C_{2x}H + H \rightarrow C_{2x}H_2$

$C_{2x}H + C_{2y} \rightarrow C_{2x+2y}H$

$C_{2x+2y}H + H \rightarrow C_{2x+2y}H_2$

Hydrogen atoms participating in reaction should necessarily come from the liquid environment, since irradiated target is constituted by carbon only. The liquid constituting the ablation environment will play a fundamental role, since the amount of available hydrogen will depend on the bond dissociation energy. Lower dissociation energy will lead to a higher amount of hydrogen and termination reactions will acquire more importance and shorter chains should be obtained. Different liquid environments will produce polyynes differently terminated. For instance, it is possible to ablate a graphite target in acetonitrile, obtaining polyynes with both hydrogen and cyano-termination **[27]**.

4.2b Preparation of Nanoaggregates

A polyyne solution has been prepared by laser ablation at 532 nm of a graphite rod submerged in Millipore grade water. Laser used was a Nd:YAG laser (Surelite II model by Continuum), with a pulse duration of 10 nanoseconds and a repetition rate of 10 Hz. In order to control the polyyne concentration, specific absorption measurements in the range of 190-300 nm have been performed with a Jasco V-650 Spectrometer and the data have been analyzed using known molar extinction coefficients taken from literature data **[39]**.

Fig. 4.2 reports the UV-Vis spectrum of as prepared polyynes solution. It is possible to observe the presence of an intense peak at 200 nm and weaker absorptions at 215 and 225 nm.

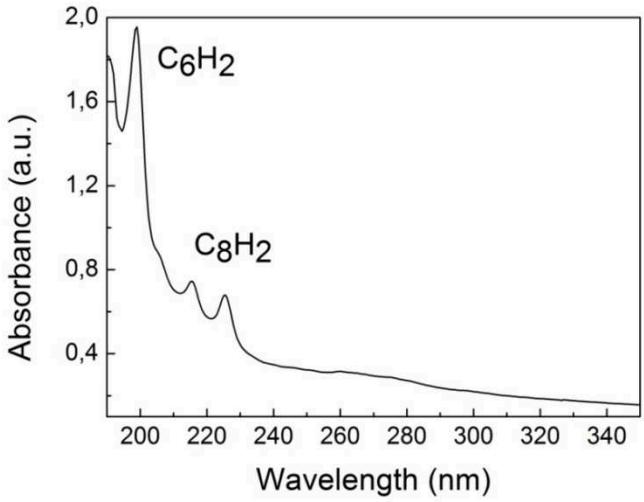

Figure 4.2 UV-Vis spectrum of a polyyne solution obtained by laser ablation of graphite in water.

In literature is reported the separation of a solution of polyynes with different chain lengths by HPLC and the attribution of UV-Vis features to each specie **[40]**.

By comparison with these data, it has been possible to recognize this signal as absorptions of C_6H_2 and C_8H_2 molecules. Since no features have been found at higher wavelengths, it is not possible to obtain polyynes longer than C_8H_2 in these experimental conditions.

The same experimental setup has been used to obtain silver nanoparticles in water. In the case of the metal, both the first (λ=1064 nm) and the second harmonic (λ=532 nm) radiations have been used.

UV-Vis spectra of obtained colloidal solutions are reported in fig. 4.3.

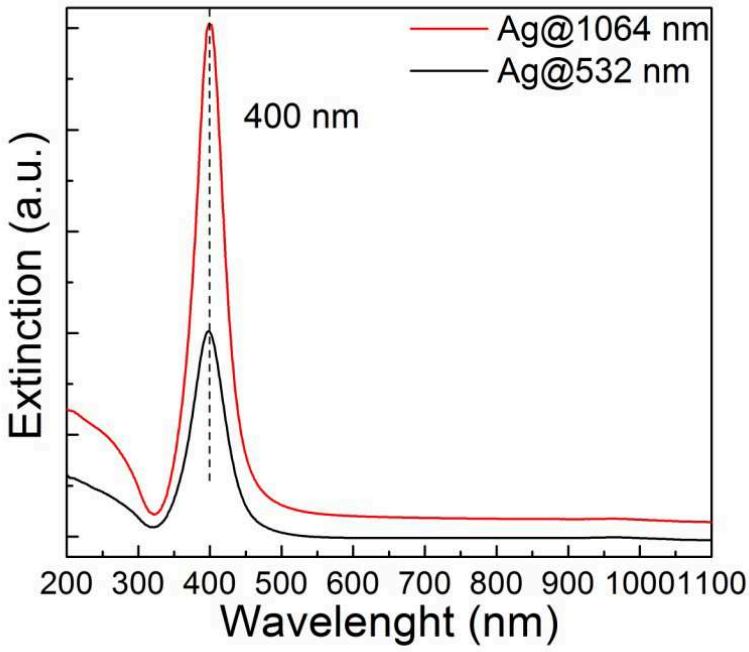

Figure 4.3 UV-Vis spectra of silver nanoparticles obtained by laser ablation of silver in water at 1064 nm (red line) and 532 nm (black line).

Fig. 4.3 shows that plasmon resonance peaks of the dispersions obtained with the two different wavelengths present the same position and width. This means that, at used experimental parameters, the laser wavelength does not influence size and shape of silver nanoparticles. Nevertheless, the spectrum of particles obtained with the first harmonic presents a higher intensity ascribable to a higher concentration of the solution. This behaviour can be attributed to the fact that while at 1064 nm the laser beam does not interact with the already formed nanoparticles, since at this wavelength the light absorption is negligible, at 532 nm it overlaps with the tail of the plasmonic signal, thus reducing the amount of energy absorbed by the target and used for removing material and increasing the local temperature of the colloid **[41]**.

To join the metal nanoparticles, silver colloids and polyyne suspensions were immediately mixed after separated preparation.

4.2c Plasmon Resonance and Surface State

Fig. 4.4 reports the extinction spectra of silver nanoparticles prepared with the 532 nm wavelength (Ag@532) suspensions before (black line in figure) and after (red line in figure) the mixing with the linear carbon chains. Slightly variations of the plasmon resonance peak can be detected, consisting in a red shift of 14 nm and a certain increase in the signal width.

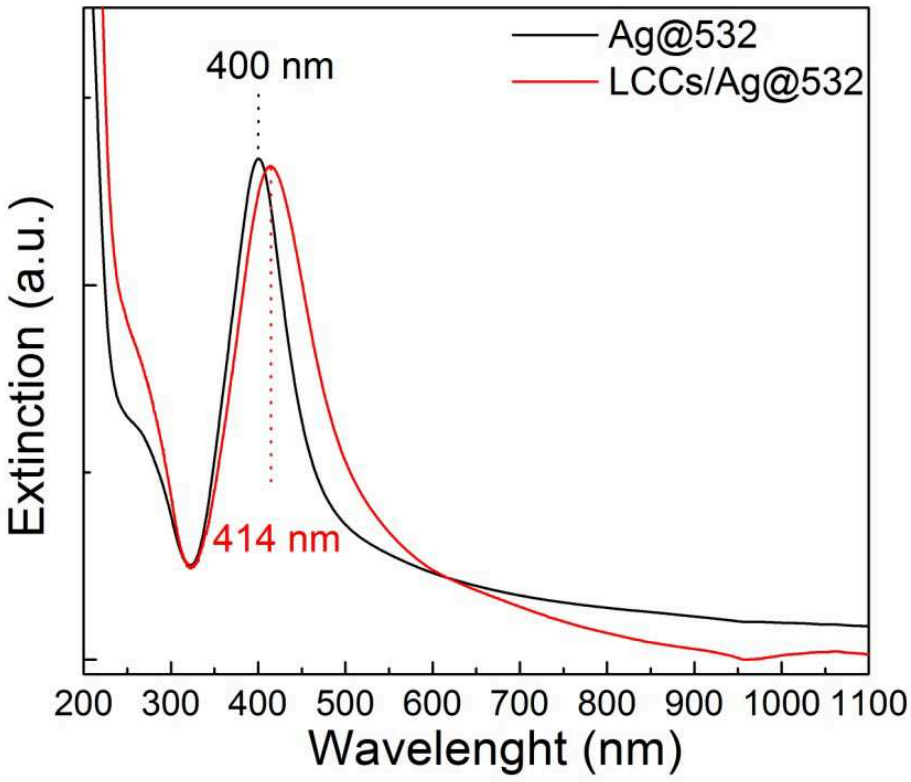

Figure 4.4 Extinction spectra of silver nanoparticles prepared at 532 nm before (black line) and after (red line) mixing with linear carbon chains

The behaviour can be attributed to common aggregation phenomena of nanoparticles, which are only favored by the presence of carbon.

On the other way, fig. 4.5 reports that the colloidal dispersion obtained by ablation at 1064 nm behaves in a deeply different way.

When the carbon chains solution are added to the sol, a second plasmon component appears at around 713 nm, while the component at lower wavelength still remains peaked at about 416 nm.

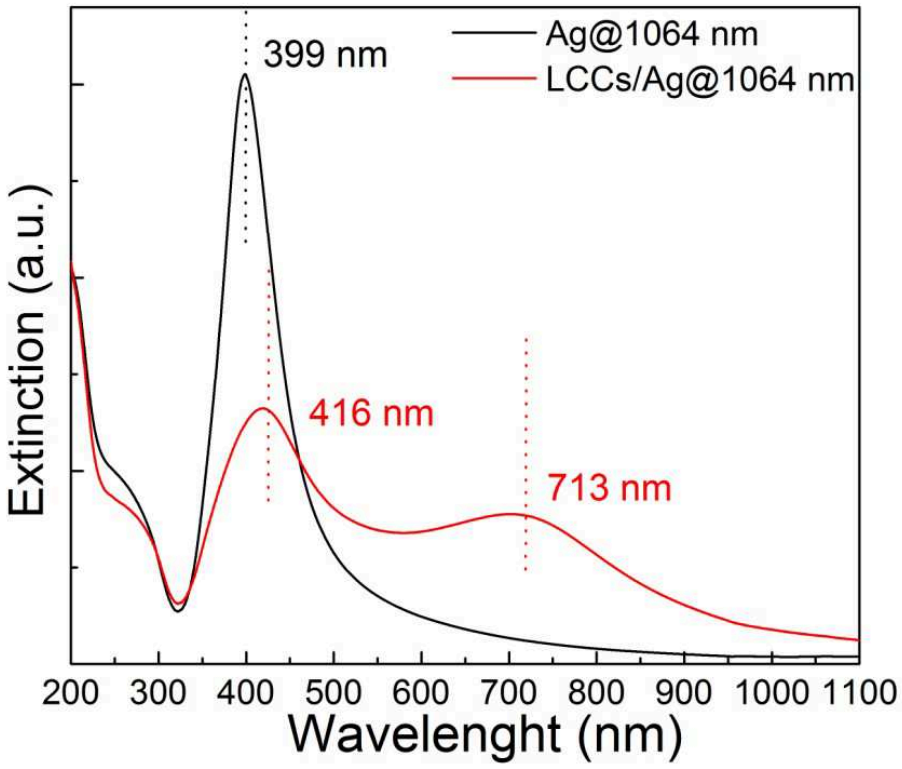

Figure 4.5 Extinction spectra of silver nanoparticles prepared at 1064 nm before (black line) and after (red line) mixing with linear carbon chains

When two nanoparticles are brought into proximity, within 2.5 times the particle diameter **[42]**, their plasmon resonance wavelength red-shifts at the decreasing of interparticle distance **[43]**.

This behaviour has been rationalized in literature **[44]** where the magnitude of the shift of the SPR (identified as λ-λ_0) has been correlated in an exponential way to the distance g between nanoparticles of diameter D:

$$\frac{\lambda-\lambda_0}{\lambda} = 0.18exp^{\left(\frac{-(g/D)}{0.23}\right)} \quad (4.1)$$

Where the *g/D* ratio is also indicated as σ. This simple mathematical model takes in accounts only dipole-dipole couplings and can be considered valid for all kinds of metals.

This relation is often indicated as the plasmon ruler equation since system constituted by couple of metal nanoparticles can be used for monitoring the distance at the nanoscale. The advantage of these structures with respect to molecular rulers based on Fluorescence Resonance Energy Transfer (FRET) **[45]** is that they do not present usual problems correlated with organic dyes, like short lifetime when continuously irradiated, blinking due to trapping in dark states **[46-47]** and limited measurements to distances lower than 10 nm **[48]**.

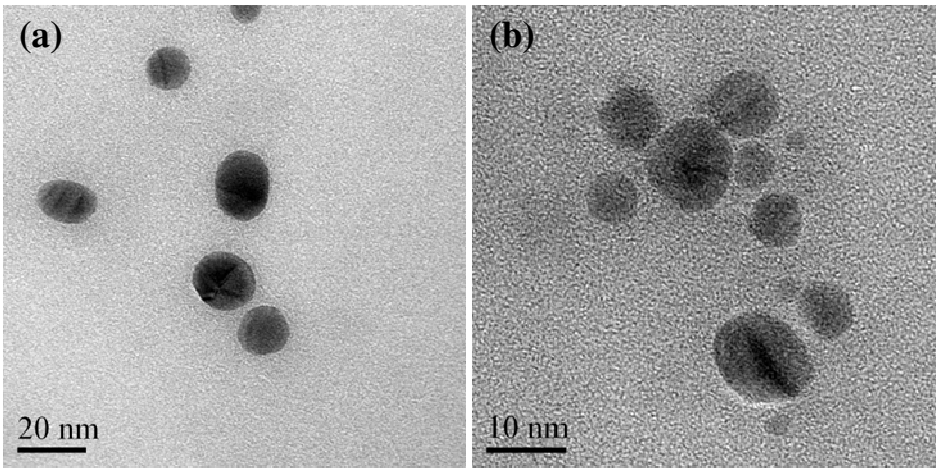

Figure 4.6 TEM images of silver metal nanoparticles obtained at 1064 nm (a) before and (b) after interaction with linear carbon chains

As can be detected by Transmission Electron Microscopy (TEM) images reported in fig. 4.6, average diameter of silver nanoparticles used for this experiment is supposed to be around 15 nm, while the average carbon chain length is estimated as 1.19 nm, corresponding to 8 carbon atoms/chains, as detected by Raman studies **[49]**.

On the basis of this hypothesis, the resulting value of σ should result far below 1.05, which is considered as a limiting value for the appearance of a double resonance contribution **[44]**. Such behaviour is due to the presence of the extended π electron system of the carbon chain acting as a plasmonic linker.

As discussed in section 4.2b, the use of different laser wavelengths during the ablation process causes a different increase of the metallic particles temperature and a change of its surface chemical state. Since the surface is a key parameter to obtain a plasmonic connection, some drops of the as prepared colloids have been deposited onto a silicon substrate for XPS measurements. These were obtained using an AXIS-ULTRA spectrometer with a basic chamber pressure in the range of 10^{-9} Torr. The X-Ray radiation was generated by Al Kα line decay (1486 eV) at operating conditions of 10 KV and 15 mA. Emitted photoelectrons were analyzed with a hemispherical electron energy analyzer. Detailed spectra have been acquired with a resolution below 1 eV.

Fig. 4.7 reports Ag3d core level spectra for the two Ag systems. XPS analysis clearly indicates that the Ag3d binding energies of Ag@532 aggregates are located at lower energy (0.93 eV) respect to the peaks of the Ag@1064 aggregates.

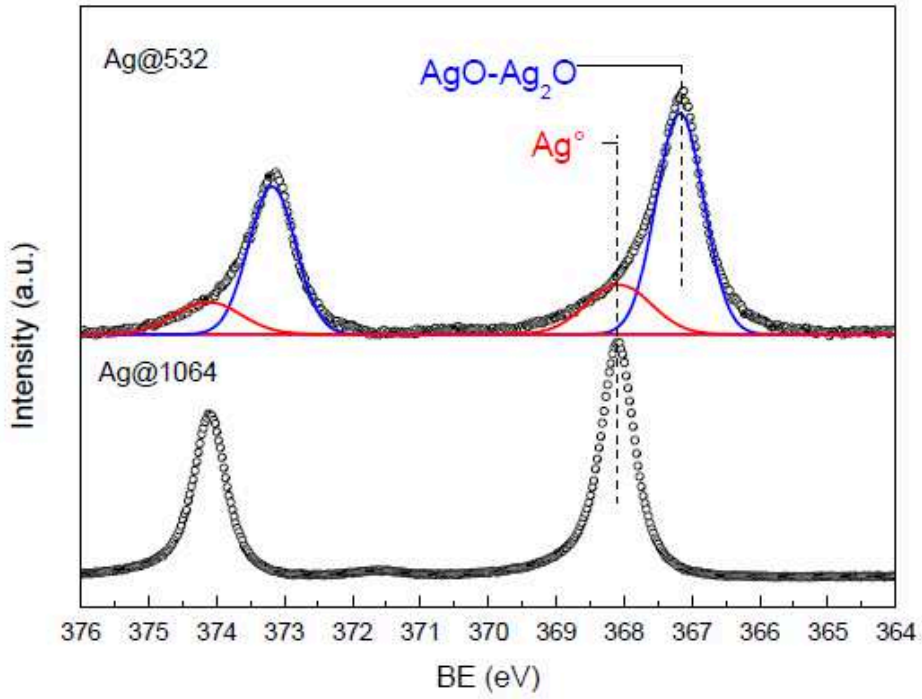

Figure 4.7 XPS spectra in the region of the Ag3d core electrons indicating the presence of silver oxides species in those silver particles prepared by ablating the metal target with a 532 nm radiation.

Such a shift indicates the presence of an oxide shell, composed by AgO and Ag_2O, at the particle surface which is formed during or immediately after its growth and is probably a consequence of the increase of temperature due to the overlapping of the irradiating wavelength with the surface plasmon resonance of the nanoparticles **[41]**. In the case of Ag@1064, it is possible to affirm that the amount of oxide is negligible and the surface can be considered "oxide free". In fig. 4.7 it is also shown the position of metallic silver and the enlargement of the line width for

the oxide signal, in agreement with literature data in which AgO is considered as a mixed oxide with the presence of both Ag^{+} and Ag^{3+} ions **[50]**. In view of the XPS results, it is possible to affirm that the oxide layer prevents the chemisorptions of the linear carbon chains thus preventing the phonon coupling. At this stage it is possible to suppose that polyyne molecules bridge the metal nanoparticles when the colloids are obtained by ablation at 1064 nm while if ablation is operated with a 532 nm radiation, the carbon wires tend to self-assemble around aggregated nanoparticles.

Following Density Functional Theory (DFT) calculations reported in literature **[51]** have shown that when nanowires are put in contact with metallic silver, that is the case of 1064 nm ablation, the terminal carbon atoms interact with silver atoms giving rise to a covalent bond which is also responsible for the formation longer polyynic linear chains assisted by the adsorption of shorter ones at the nanoparticle surface.

4.2d Simulation of Observed Plasmon Resonances

As reported in literature **[52]**, the entire plasmon resonance spectrum can be simulated using a classical Mie approach for a large number of metal nanoparticles. The the basis of this model have already been discussed in section 1.2.

In the case of particles much smaller than the wavelength of light, it is possible to use the dipole plasmon approach, since the electric field of light can be considered constant and interaction is governed by

electrostatics rather than electrodynamics. This is often called the quasistatic approximation, since the wavelength-dependent dielectric constants of the metal particle (ε) and of the surrounding medium (ε_m) are used. The polarizability of a sphere of radius R is given by:

$$\alpha = R^3 \frac{\varepsilon - \varepsilon_m}{\varepsilon + 2\varepsilon_m} \quad (4.2)$$

If the particle cannot be considered "small" enough, multipolar terms have to be taken in account following the complete Mie theory for spherical particles or the Mie-Gans for ellipsoidal particles.

For instance it is necessary to introduce a quadrupolar term such as:

$$\beta = R^5 \frac{\varepsilon - \varepsilon_m}{\varepsilon + 3/2\varepsilon_m} \quad (4.3)$$

Following this last approach the simulation of spectra reported in figs. 4.4 and 4.5 has been operated by using the complete Mie theory for spherical particles with a bulk silver dielectric constant.The results of the simulations (lines) together with the experimental spectra (dots) are reported in fig. 4.8. It should be noted that simulations have been performed considering different sphere radii ranging from 10 to 90 nm, so that the contribution of multipolar terms results more important at the increasing of the nanoparticle size. In particular, fig. 4.8 shows that for small particles, with dimensions of 10-18 nm, there is the presence of a unique resonance structure that shifts to larger wavelength and spreads its Full Width at Half Maximum at the increasing of the radius. For larger sizes (30-90 nm), one or two other resonances appear, attributed to the quadrupole and higher order resonances.

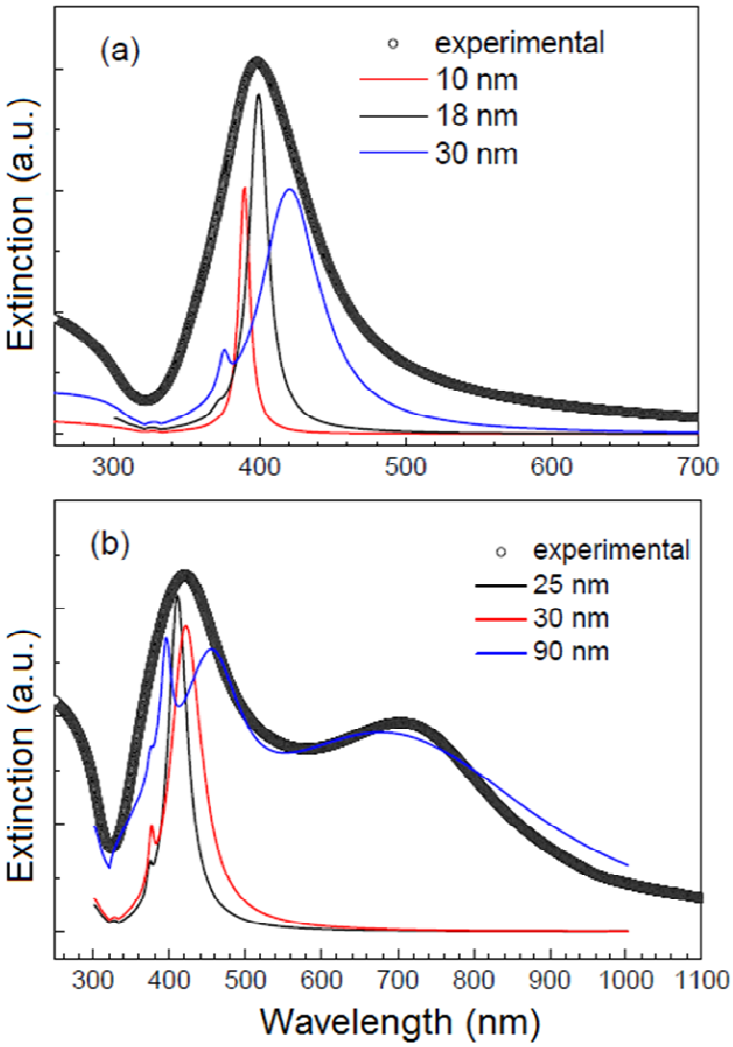

Figure 4.8 Plasmon resonances of silver nanoparticles (a) with and (b) without the oxide shell after the interaction with carbon nanowires. Simulated spectra obtained with a Mie approach in a multipolar expansion approximation and using different particle size in a spherical configuration.

A comparison between experimental data and simulations indicates once again that the overall extinction spectra of silver clusters connected by carbon nanowires can be considered as the result of an extended spherical network of plasmon connected metal nanoparticles free of oxide shells. Fig. 4.8b shows that is necessary to consider resonances extended to a 90 nm global entity (at least three of the as prepared nanoparticles) in order to simulate the experimental plasmon resonance spectrum.
These results are in accordance with the information obtained by TEM image reported in fig. 4.6b, which shows the presence of structures constituted by more mutually connected particles.

4.2e SERS Implications

The local electromagnetic field enhancement is of particular interest in the case of Surface Enhanced Raman Scattering (SERS), since it allows to intensify otherwise weak Raman signals of a factor of 10^6. This effect was first discovered in roughened silver electrodes **[53-54]** and it has been attributed to electromagnetic enhancement due to plasmon excitation and chemical effects, which includes all the molecule-metal interactions.
An area of great interest concerns the observation of single molecule SERS (SM-SERS) **[55]** due to the nominal enhancement factor above 10^{13}.
The maximization of the SERS signals requires several factors, such as a strong plasmon resonance of the substrate and the localization of the

molecule as near as possible on the surface of the nanoparticle since it is a near field phenomenon **[56]**. The obtained intensified local field is often called a SERS "hot spot" [**57**].

These requirements can be fulfilled by pure surface noble metal nanoparticles prepared by laser ablation in liquid that have been recognized as excellent SERS substrates **[58]**. Indeed, silver nanoparticles prepared by laser ablation in water have demonstrated a better reproducibility in SERS enhancement with respect to chemical prepared ones **[59]**.

A further increasing of SERS magnification is obtained once the laser excitation wavelength is close to the plasmon resonance of the metallic nanoparticles **[9,60]**.

Since linear carbon chains are positioned between nanoparticles and that site can be considered as a SERS hot spot **[57]**, it should be possible to identify spectroscopic features of these systems.

Raman spectra of the solutions were directly performed in liquid using a 10X optical objective with a laser power density below 10 mW and a Jobin Yvon 450 mm focal length monochromator, equipped with a CCD camera detector cooled at 77 K. Experiment were performed using two different laser sources: an Argon laser (λ=514.5 nm) and a He:Ne laser (λ=632.8 nm).

In accordance with Raman spectroscopic studies on *sp*-bonded carbon species **[61]**, it is possible to observe clear SERS signals detected in the 1800-2150 cm^{-1} region when the carbon chains have a number of carbon atoms between 6 and 20. In addition to the *sp* vibrational features, a

broad band located between 1000 and 1700 cm^{-1} is generally detected, coming from highly disordered graphite-like structures **[62]**.

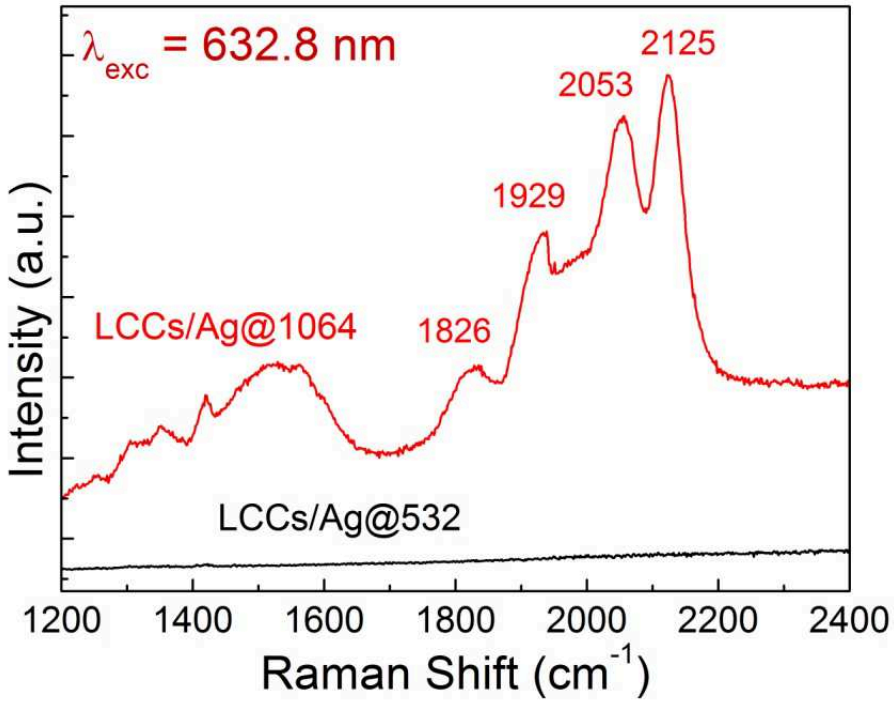

Figure 4.9 SERS spectra obtained at 632.8 nm excitation wavelenght for silver/carbon hybrid structure prepared using silver colloids obtained by laser ablation at 1064 nm (red line) and 532 nm (black line).

Fig. 4.9 reports SERS spectra of solutions obtained by using the 632.8 nm exciting radiation for nanoparticle nanoparticles prepared with the first (red line) and the second (black line) harmonic.

Here, only nanowires which are plasmonically connected to nanoparticles present the typical features correlated to carbon system, while particles prepared with the second harmonic do not show signals at all.

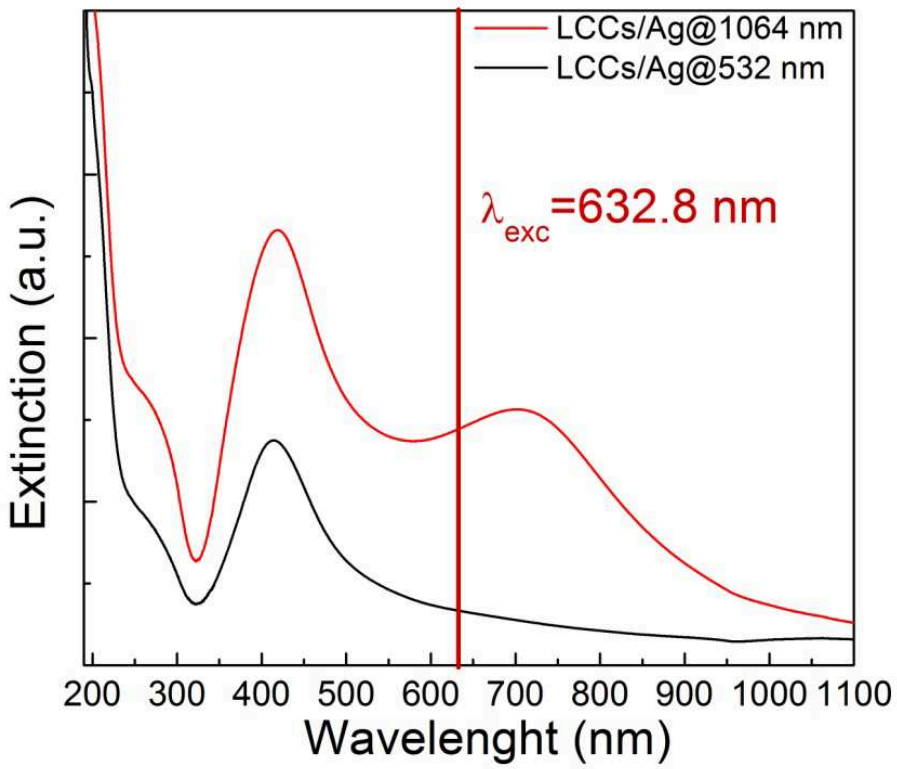

Figure 4.10 Overlapping of 632.8 nm excitation wavelenght with UV-Vis spectra of hybrid systems at 1064 nm (red line) and 532 nm (black line).

This behaviour can be explained considering the resonance contribution discussed above **[9,60]**.

As shown in fig. 4.10, used exciting wavelenght (632,8 nm) overlaps only the plasmon resonance of Ag@1064 nanoparticles, and this causes the enhancement of signals of polyynes bonded to these structures.

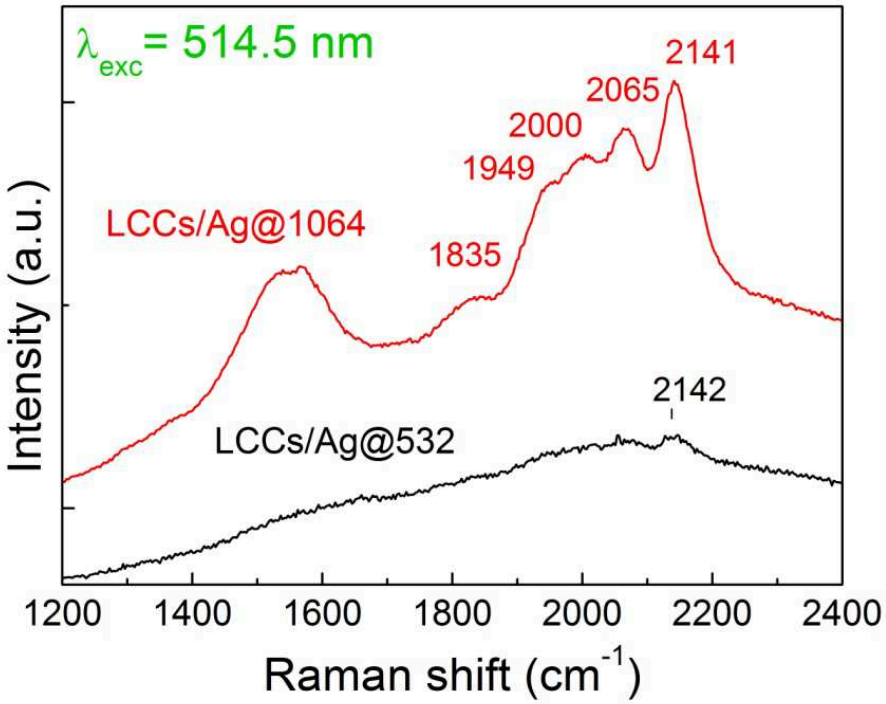

Figure 4.11 SERS spectra obtained at 514.5 nm excitation wavelenght for silver/carbon hybrid structure prepared using silver colloids obtained by laser ablation at 1064 nm (red line) and 532 nm (black line)

Fig. 4.11 reports spectra obtained with the 514.5 nm exciting wavelenght. Here, it is possible to note how either nanowires connected to Ag@1064 and Ag@532 present the typical *sp* spectroscopic features with different intensities. In particular, peaks of linear carbon chains connected to

nanoparticles are clearly visible, while polyynes mixed with silver collids prepared with the second harmonic show only a weak signal at around 2140 cm^{-1}. The results can be attributed to the fact that in this case, the exciting wavelength overlaps the plasmon resonances of both systems, as indicated in fig. 4.12, and thus both systems will present electromagnetic field enhancement.

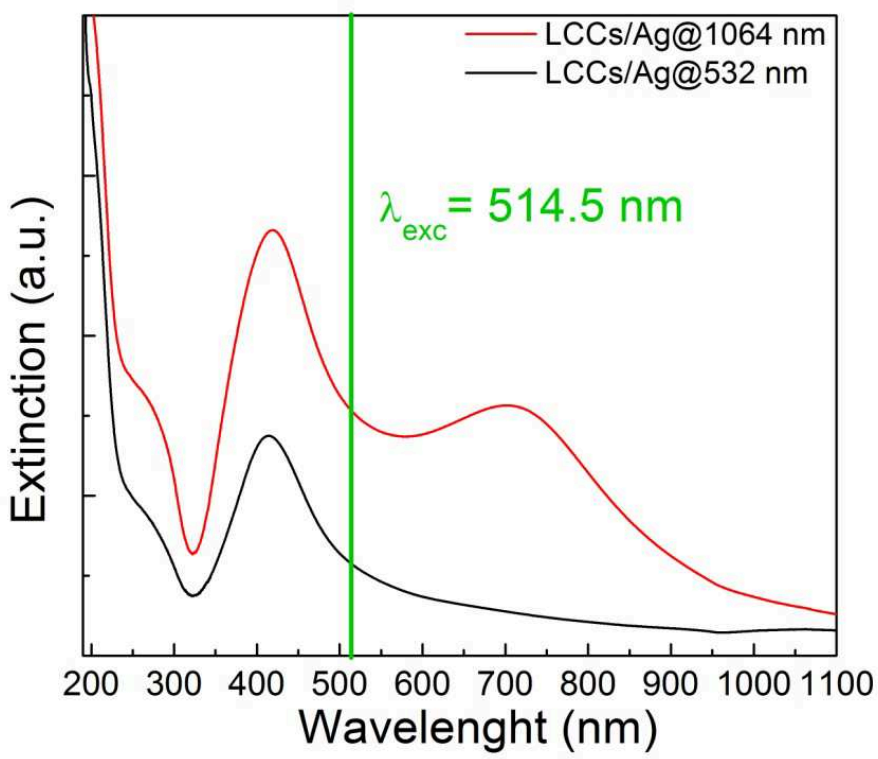

Figure 4.12 Overlapping of 514.5 nm excitation wavelenght with UV-Vis spectra of hybrid systems at 1064 nm (red line) and 532 nm (black line).

To explain the variation in intensities, it should be considered the different surface state of the particle. As already discussed, polyynes are connected only to the surface of particles prepared with the first harmonic, due to the higher purity of them, while they do not chemically interact with 532 nm prepared colloids. Thus, charge transfer phenomena, responsible for SERS enhancement **[63]**, happen only in the first case, and this is the reason why nanowires connected to Ag@1064 present SERS signals one order of magnitude larger.

4.3 MONITORING OF THE AGGREGATION OF GOLD NANOPARTICLES IN LIQUID

As discussed in section 4.2, aggregation of silver nanoparticles strongly depends on the oxidation surface state of the particle and so joining has to be driven by the presence of some molecular entities.

In the past years, scientific interest has also been addressed to a direct surface joining of pure nanoparticles, since the manipulation of the structure leads to a variation of plasmon resonance characteristics.

This is possible since a decrease of melting temperature and enthalpy of melting, due to the reduction of size, has been found in metal nanoparticles **[64-65]**. In particular, research has been focused on the possibility of welding gold nanoparticles.

Aggregation of gold nanoparticles leads to a red shift in surface plasmon, which can be also detected by naked eye as red to blue color change **[66]**.

The variation of color has been attributed to the increased size resulting from the aggregation **[67]**.

Literature reports the possibility of welding gold nanoparticles deposited on carbon-coated copper TEM grids by use of picoseconds laser pulses **[68]**. The welding has been attributed to the heating of nanoparticles due to the absorption of the laser pulses. Gold particles are well conjugated to show single-phased nanoconjunction **[68]**.

The paper discussed above contemplates the use of an energy source, but more interesting results have been obtained studying welding at room temperature, or "cold" welding.

Ultrathin single crystal Au nanowires have been joined using only mechanical contact in a high-resolution transmission electron microscope equipped with scanning tunneling microscope (STM) **[69]**. The joint strength reached ~600 MPa, comparable to that of the original nanowire.

Literature also reports attempts to join gold nanoparticles in liquid at room temperature. Cold-welding of gold nanoparticles has been obtained by injecting a mixture of ethanol and toluene in a gold nanoparticle solution **[70]** and this has been confirmed by a red shift of the plasmon resonance band.

It has also been reported a bottom – up approach for the synthesis of gold nanowires by welding of nanoparticles using carbon nanotubes as templates [**71]**.

However, mentioned examples report morphological characterization by microscopy, which means after deposition of particles on a solid

substrate. Since pure nanoparticles can be produced by laser ablation in liquid environment, a deposition process can change the particle state and introduce spurious effects during and after drying, which depend on many factors such as the drying rate, the nature of the particle surface interaction and the interaction with ambient atmosphere.

Aggregation of nanoparticles happens spontaneously in liquid and studies have demonstrated that aggregation phenomena of noble metal nanoparticles in water are due to strong dipole/dipole interactions generated by an asymmetric charge distribution onto the cluster surface [**72**].

For these reasons, a starting point to control cold welding in liquid environment could include the study of aggregation in liquid phase.

Literature reports that aggregation phenomena of nanoparticles in liquid have been studied by spectroscopic techniques as UV-Vis, Infrared and Dynamic Light Scattering **[73-74]** and it has been demonstrated their importance in giving temporal information about the aggregation processes.

Gold nanoparticles have been produced by focusing the first harmonic of a Nd:YAG laser (λ=1064 nm) (Surelite II model by Continuum) on a gold plate placed at the bottom of a vessel filled with Millipore grade water. Ablation was carried on for 10 minutes with a fluence of 10 J/cm^2 and a repetition rate of 10 Hz.

4.3a Dynamic Light Scattering

Light scattering measurements were performed by a homemade apparatus constituted of a quartz scattering cell, confocal collecting optics, a Hamamatzu photomultiplier mounted on a rotating arm, a BI-9100 AT hardware correlator (Brookhaven Instruments Corporation). Sample has been illuminated by 633 nm He-Ne laser with power ranging between 15 and 50 mW. The autocorrelation function is provided by the hardware correlator operating in single photon counting regime.

Since particles in solution are subject to Brownian motion, the light scattered by the suspension fluctuates in time.

Analysis of the fluctuations of the scattered light is performed by the intensity auto-correlation function **[75]** defined as:

$$g_2(q,t) = \frac{1}{\langle I \rangle^2} \lim_{T\to\infty} \frac{1}{T} \int_0^T I(q,t) I(q,t+\tau) d\tau - 1 \qquad (4.4)$$

where I is the scattered light intensity, $\langle I \rangle$ is the temporal average scattered light intensity and T is the acquisition time, q is the scattering vector defined as $q=(4\pi n/\lambda)\sin(\theta/2)$, being n the refraction index of the solvent, λ the light wavelength and θ the scattering angle. The field autocorrelation function g_1 is calculated by the g_2 using the Segret relation $g_2=|g_1|^2$. For monodisperse non-interacting particles in Brownian motion the g_1 function is a decreasing exponential with a relaxation rate Γ ($\Gamma=1/\tau$ with τ= decay time) while in polydisperse solutions g_1 shows several exponential decay components which can be analyzed either by cumulant or multi-exponential analysis **[75]**.

The intensity autocorrelation function of light scattered with polarization parallel ($g_{2,VV}$) and perpendicular ($g_{2,VH}$) to that of the incident beam has been measured. In particular, DDLS measurements give information about anisotropy in the particle's polarizability through a measure of the rotational diffusion **[75]**.

The intensity autocorrelation function $g_{2,VV}(t)$ and $g_{2,VH}(t)$ measured independently at a scattering angle ϑ=90° (q= 18 μm^{-1}) are reported in fig. 4.13 for as-prepared sols and for the colloid aged for 20 days.

In fig. 4.13 are reported data of the polarized experiment, where it is clearly visible that aging of the colloid induces a slower decay time. Indeed, from an analysis of the autocorrelation function by using the cumulant method, a values of relaxation rates ($\Gamma=1/\tau$) of the order of Γ_{VV}=2372 s^{-1} has been obtained for the as prepared sample, while the aged solution presents a relaxation rate of Γ_{VV}=1865 s^{-1} .

From the obtained relaxation rate, it is possible to calculate both the translational diffusion coefficient (Dt) and the hydrodynamic radius using the following expressions, that have been widely used in literature **[75- 77]** :

$$\Gamma_{VV} = D_t q^2 \tag{4.5}$$

$$R_h = \frac{kT}{6\pi \cdot \eta \cdot D_t} \tag{4.6}$$

Where η is the viscosity of the medium, k is the Boltzmann constant and T the absolute temperature. Specifically, calculated value of D_t=7.4x$10^{-8}$$cm^2$/s and R_H=33±3 nm in the case of the as prepared colloid and D_t=5.7x$10^{-8}$$cm^2$/s and R_H=43±3 nm after aging have been found,

demonstrating a substantial increase in the hydrodynamic radius while aging.

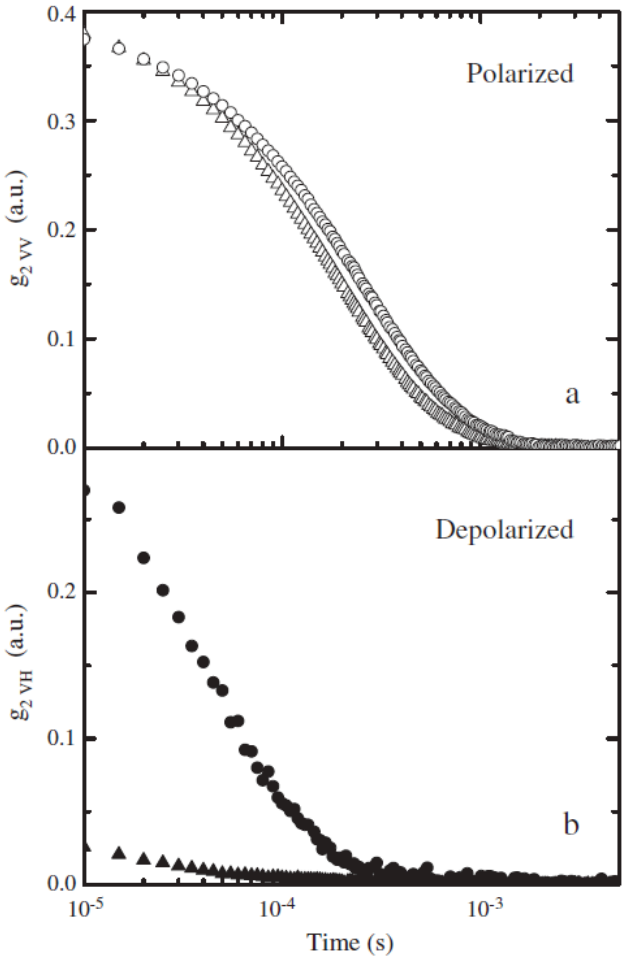

Figure 4.13 Correlation functions $g_{2,VV}(t)$ measured in as-prepared (Δ) and aged solution (o) in polarized conditions (a) and correlation functions $g_{2,VH}$(t) measured in as-prepared (▲) and aged solution (●) in depolarized conditions (b). The measurements are performed at scattering angles of 90°.

Such increase is attributed to aggregation phenomena and the formation of multimers starting from existing particles, which lead to a change of the hydrodynamic radius.

If this hypothesis is correct, new formed aggregates could show anisotropy, detectable through depolarized experiments.

In fig. 4.13b is reported the depolarized autocorrelation functions for as-prepared and aged samples, showing remarkable differences. In fact, the intensity is almost negligible in the case of the as prepared colloid, with a value of about the 5%, while it is consistent in the aged sol. These results qualitatively indicate that the as prepared solution is mainly composed by optically isotropic nanoparticles, which turn to be anisotropic aggregates as time goes by. Moreover it is also clear that the decay time for $g_{2,VH}(t)$, measured in aged sample, is about a factor five lower with respect to that for $g_{2,VV}(t)$.

In order to obtain further insights into the shape of AuNPs, $g_{2,VV}(t)$ and $g_{2,VH}(t)$ at different angles have been measured, thus changing the scattering vector in the range 9 $\mu m^{-1} < q < 23\ \mu m^{-1}$ (40°-120°). It is possible to assume that Γ_{VH} is composed of two terms, as follows **[77]**:

$$\Gamma_{VH} = D_t q^2 + 6D_r \qquad (4.7)$$

where D_r is the rotational diffusion coefficient.

Assuming a decoupling of rotational and translational diffusion mechanisms, relations (4.5) and (4.7) allow to deduce D_t and D_r **[77]**.

Fig. 4.14 reports obtained Γ values as a function of the square of the scattering angle q^2.

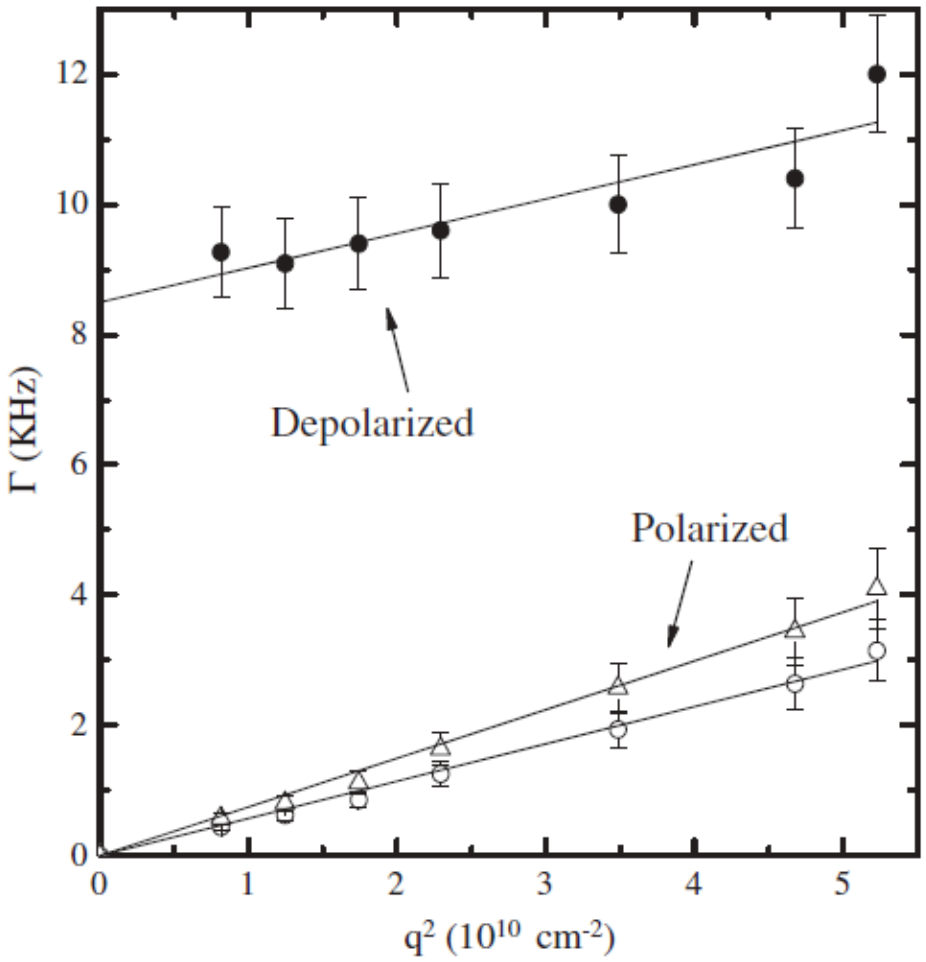

Figure 4.14 Relaxation rate of the correlation function as function of wavevector squared for as-prepared (Δ) and aged sample (o) in polarized conditions and for aged sample (●) in depolarized conditions. The solid lines indicate the linear fits through the data points.

The relaxation rate Γ_{VV} in "as prepared" solution shows a linear increase with q^2 following the relation (4.5). The best fit of experimental data

gives a value of diffusion coefficient D_t=5.71x10^{-8} cm^2/s and a hydrodynamic radius of 41 nm has been determined. These values are in agreement with the radii already calculated after a single angle measurement.

The relaxation rate Γ_{VH} as a function of q^2, follows the relation (4.7), and linear fit to the data have been used to estimate the rotational diffusion coefficient D_r=1416 cm^{-1}. The translational diffusion coefficient obtained by the slope of Γ_{VH} in function of q^2 is very close to the values determined in polarized condition. In the as prepared sample Γ_{VH} has not been calculated because the correlation function intensity is negligible at all scattering angles.

The most intuitive rather than simple geometrical model of an aggregate cluster in solution is that of a prolate ellipsoid **[77-78]**. If we assume such a shape and individuate a major axis a, a minor axis b and an aspect ratio $\rho=a/b$, the translational and rotational diffusion coefficients for a prolate ellipsoid are given by the expressions **[78]**:

$$D_t = \frac{kT}{6\pi\cdot\eta\cdot a} G(\rho) \tag{4.8}$$

$$D_r = \frac{3kT}{16\pi\eta a^3}\left\{\frac{\left(2-\rho^{-2}G(\rho)-1\right)}{1-\rho^{-4}}\right\} \tag{4.9}$$

where

$$G(\rho) = \frac{1}{\sqrt{1-\rho^{-2}}}\ln\left(\frac{1+\sqrt{1-\rho^{-2}}}{\rho^{-1}}\right) \tag{4.10}$$

Non linear eqs. (4.8) and (4.9) have been inverted numerically and the values of a and ρ consistent with the two independent measurements of D_t and D_r of the aged solution have been computed. A value for the major axis a=69 nm and for the minor axis b=36 nm have been found.

Then the major axis is about twice the minor axis *b*, suggesting that the ellipsoidal nanoparticles in aged solution are dimers, which are generated by coupling of spherical AuNPs having average radius of 36 nm, while in as prepared solution there are only spherical particles.

4.3b UV-Vis Sectroscopy

Aggregation phenomena in noble metal sols are frequently observed in terms of changes of the so called "Surface Plasmon Resonance" (SPR) and modeled by considering solutions of the Maxwell equations such as those found in the Mie-Gans theory or in the discrete dipole approximation method **[52]**.

The Mie-Gans model shows that a spherical shaped metallic cluster presents a unique SPR peaked at about 520 nm in the dipole approximation while a prolate ellipsoid gives two characteristic extinction signals, one at the same frequency of the spherical particles, due to the polarization along the shorter axis and the other red shifted due to the polarization along the longer axis.

In fig. 4.15 is reported the experimental extinction spectra for as prepared as well as aged samples in the gold SPR region. The first spectrum shows an SPR at 523 nm instead the spectrum of aged sample evidences two SPR at 530 nm and at 670 nm, confirming the formation of non spherical nanoparticles during aging.

Much more insight can be gained using one of the above mentioned models for the simulation and fitting of the extinction spectra. It is

possible to consider the colloidal suspension as a mixture of spherical and ellipsoidal nanoparticles with a total extinction cross section given by **[52]**:

$$\sigma_{ext} = N_s \cdot \sigma_{sph}(\omega, r) + N_e \cdot \sum_{\rho} \sigma_{ellips}(\omega, \rho, a) \cdot G_{\sigma}(\rho) \quad (4.11)$$

Where N_s and N_e are the concentration of spherical and ellipsoidal nanoparticles respectively, while $\sigma_{sph}(\omega,r)$ and $\sigma_{ellips}(\omega,\rho,a)$ are their cross sections which depend on the radius of the spherical particle (r), the frequency of the incoming light (ω), the aspect ratio (ρ) and the major axis (a) of the considered ellipsoid. In the used model it has also been considered that the ellipsoids are formed in the colloid with a Gaussian distribution of aspect ratios $G_{\sigma}(\rho)$, centered at $\rho=1$ and a broadening σ. Details of the mathematical expressions of $\sigma_{sph}(\omega,r)$, $\sigma_{ellips}(\omega,\rho,a)$ and $G_{\sigma}(\rho)$ can be found in literature **[79-80]**.

It has been demonstrated **[79]** that such a model is suitable for the evaluation of the size, aspect ratio and fraction of non spherical particles in a gold colloid. This has been done through a fitting procedure which involves a limited number of parameters (r, N_s , N_e, ρ, a,σ) which can be further reduced in considered case, thanks to the DLS measurements, since the average particle size (r,a) and the aspect ratio (ρ) have been already calculated by DDLS measurements.

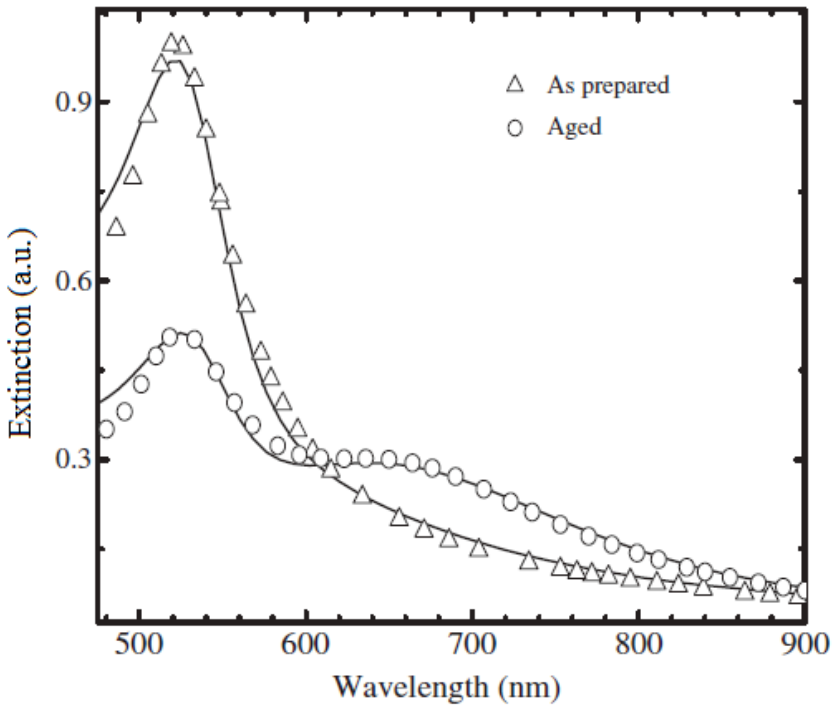

Figure 4.15 UV–Vis spectra of Au-NPs solution of as-prepared and aged sample. The solid lines refer to fit obtained by Mie-Gans model.

Obtained fits are reported in fig. 4.15: the total concentration of ellipsoids (N_e) reaches only a few percent with respect to that for the spherical particles in the as prepared colloid, while it reaches 60% in the aged sample. As regards the standard deviation σ, the fitting procedure indicates that about 68% of the elliptical particles have ρ smaller than 2.4 (σ=*1.4*), in agreement with light scattering measurement where we estimate aspect ratios of about 2.0, confirming that aggregates are mainly constituted by dimers.

REFERENCES

[1] S. Lal, S. Link, N.J. Halas, *Nature Photon.*, 2007, **1**, 641-648

[2] L. Novotny, B. Hecht, "Principles of Nano-Optics", Cambridge University Press: Cambridge, 2006

[3] G. Compagnini, C. Galati, S. Pignataro, *Phys. Chem. Chem. Phys.*, 1999, **1**, 2351-2353

[4] J.M. Yuen, N.C. Shah, J.T. Walsh, M.R. Glucksberg, R.P. Van Duyne, *Anal. Chem.*, 2010, **82**, 8382-8385

[5] M.D. Wissert, K.S. Ilin, M. Siegel, U. Lemmer, H.J. Eisler, *Nano Lett.*, 2010, **10**, 4161-4165

[6] C. Jennings, R. Aroca, R. *Anal. Chem.*, 1984, **56,** 2033–2035

[7] A.M. Michaels, J. Jiang, L. Brus, *J. Phys. Chem. B*, 2000, **104,** 11965–11971

[8] C.L. Hayes, R.P. Van Duyne, *J. Phys. Chem. B*, 2003, **107,** 7426–7433

[9] C.E. Talley, J.B. Jackson, C. Oubre, N.K. Grady, C.W. Hollars, S.M. Lane, T.R. Huser, P. Nordlander, N.J. Halas, *Nano Lett.*, 2005, **5**, 1569–1574

[10] V.P. Drachev, M.D. Thoreson, V. Nashine, E.N. Khaliullin, D. Ben-Amotz, V.J. Davisson, V.M. Shalaev, *J. Raman Spectrosc.*, 2005, **36,** 648–656

[11] T. Atay, J.H. Song, A.V. Nurmikko, *Nano Lett.*, 2004, **4,** 1627–1631

[12] I. Romero, J. Aizpurua, G.W. Bryant, F.J.G. de Abajo, *Opt. Express*, 2006, **14,** 9988–9999

[13] P. Nordlander, C. Oubre, E. Prodan, K. Li, M.I. Stockman, *Nano Lett.*, 2004, **4,** 899–903

[14] W. Rechberger, A. Hohenau, A. Leitner, J. R. Krenn, B. Lamprecht, F.R. Aussenegg, *Opt. Comm.*, 2003, **220,** 137–141

[15] L. Gunnarsson, T. Rindzevicius, J. Prikulis, B. Kasemo, M. Käll, S. Zou, G.C. Schatz, *J. Phys. Chem. B*, 2005, **109,** 1079–1087

[16] M. Hentschel, M. Saliba, R. Vogelgesang, H. Giessen, A.P. Alivisatos, N. Liu, *Nano Lett.*, 2010, **10**, 2721-2726

[17] D. Zanchet, C.M. Micheel, W.J. Parak, D. Gerion, S.C. Williams, A.P. Alivisatos *J. Phys. Chem. B*, 2002, **106,** 11758–11763

[18] T.J. Yim, Y. Wang, X. Zhang, *Nanotechnology*, 2008, **19**, 435605

[19] F. Cataldo, *Polym. Int.*, 1999**, 44**, 191–200

[20] F. Diederich, R.E. Martin, *Angew. Chem. Int. Ed.*, 1999**, 38**, 1350–1377

[21] M. Mayor, M. Büschel, K.M. Fromm, J.M. Lehn, J. Daub, *Chem. Eur. J.*, 2001**, 7**, 1266–1272

[22] N.F. Utesh, F. Diederich, *Org. Biomol. Chem.*, 2003**, 1**, 237–239

[23] R. Zahradnik, L. Sroubková, *Helv. Chim. Acta*, 2003**, 86**, 979–1000

[24] R.J. Lagow, J.J. Kampa, H.C. Wei, S.L. Battle, J.W. Genge, D.A. Laude, C. J. Harper, R. Bau, R.C. Stevens, J.F. Haw, E. Munson, *Science*, 1995, **267**, 362-367

[25] J. Hlavatý, L. Kavan, N. Kasahara, A. Oya, *Chem. Comm.*, 2000, **9**, 737-738

[26] A. Yasuda, N. Kawase, T. Matsui, T. Shimidzu, C. Yamaguchi, H. Matsui, *Reac. Funct. Polym.*, 1999, **41**, 13-19

[27] G. Compagnini, V. Mita, R.S. Cataliotti, L. D'Urso, O. Puglisi, *Carbon*, 2007, **45**, 2456-2458

[28] M.Tsuji, S. Kuboyama, T. Matsuzaki, T. Tsuji, *Carbon*, 2003, **41**, 2141-2148

[29] T. Sakka, K. Saito, Y.H. Ogata, Appl. Surf. Sci., 2002, **197-198**, 246-250

[30] J.M. Zazula, "LHC Project Note 78 / 97", CERN: Geneve, 1997

[31] S.B. Ogale, A.P. Malshe, S.M. Kanetkar, S.T. Kshirsagar, *Solid State Comm.*, 1992, **84**, 371-373

[32] S.R.J. Pearce, S.J. Henley, F. Claeyssens, P.W. May, K.R. Hallam, J.A. Smith, K.N. Rosser, *Diamond Relat. Mater.*, 2004, **13**, 661-665

[33] J.B. Wang, C.Y. Zhang, X.L. Zhong, G.W. Yang, *Chem. Phys. Lett.*, 2002, **361**, 86-90

[34] T. Guo, P. Nikolaev, A.G. Rinzler, D. Tomanek, D.T. Colbert, R.E. Smalley, *J. Phys. Chem.*, 1995, **99**, 10694-10697

[35] T. Guo, P. Nikolaev, A. Thess, D.T. Colbert, R.E. Smalley, *Chem. Phys. Lett.*, 1995, **243**, 49-54

[36] A.V. Rode, S.T. Hyde, E.G. Gamaly, R.G. Elliman, D.R. McKenzie, S. Bulcock, *Appl. Phys. A*, 1999, **69**(Suppl.), S755-S758

[37] A. Fojtik, A. Henglein, *Ber. Bunsen Phys. Chem.*, 1993, **97**, 252-254

[38] G. Compagnini, M.G. Sinatra, P. Russo, G.C. Messina, O. Puglisi S. Scalese, *Carbon*, 2012, **50**, 2362–2365

[39] R. Eastmond, T.R. Johnson, D.R.M. Walton, *Tetrahedron*, 1972, **28**, 4601-4616.

[40] F. Cataldo, *Carbon*, 2004, **42**, 129-142

[41] S. Bruzzone, M. Malvaldi, *J. Phys. Chem. C*, 2009, **113**, 15805-15810.

[42] K.H. Su, Q.H. Wei, X. Zhang, J.J. Mock, D.R. Smith, S. Schultz, *Nano Lett.*, 2003, **3**, 1087-1090

[43] Elghanian, R.; Storhoff, J. J.; Mucic, R. C.; Letsinger, R. L.; Mirkin, C. A. *Science* **1997**, *277*, 1078-1081

[44] B.M. Reinhard, M. Siu, H. Agarwal, A.P. Alivisatos, J. Liphardt, *Nano Lett.*, 2005, **5**, 2246-2252

[45] T. Ha, T. Enderle, D.F. Ogletree, D.S. Chemla, P.R. Selvin, S. Weiss, *Proc. Natl. Acad. Sci. U.S.A.*, 1996, **93**, 6264-6268

[46] A. Yildiz, J.N. Forkey, S.A. McKinney, T. Ha, Y.E. Goldman, P.R. Selvin, *Science*, 2003, **300**, 2061-2065

[47] R. Zondervan, F. Kulzer, S.B. Orlinskii, M. Orrit, *J. Phys. Chem. A*, 2003, **107**, 6770-6776

[48] J.R. Lakowicz, "Principles of Fluorescence Spectroscopy" 2nd ed., Kluwer Academic/Plenum Publishers: New York, 1999

[49] V. Scuderi S. Scalese S. Bagiante, G. Compagnini, L. D'Urso, V. Privitera, *Carbon*, 2009, **47**, 2134-2137

[50] F.A. Cotton, G. Wilkinson, "Advanced Inorganic Chemistry", 5th ed. Wiley-Interscience: New York 1988

[51] A. Lucotti, M. Tommasini, M. Del Zoppo, C. Castiglioni, G. Zerbi, F. Cataldo, C.S. Casari, A. Li Bassi, V. Russo, M. Bogana, C.E. Bottani, *Chem. Phys. Lett.* 2006, **417**, 78-82

[52] U. Kreibig, M. Vollmer, "Optical Properties of Metal Clusters", Springer: New York, 1994.

[53] D.L. Jeanmaire, R.P. Van Duyne, *J. Electroanal. Chem.*, 1977, **84,** 1–20

[54] M.G. Albrecht, J.A. Creighton, *J. Am. Chem. Soc.*, 1977, **99,** 5215–5217

[55] K. Kneipp, Y. Wang, H. Kneipp, L.T. Perelman, I. Itzkan, R.R. Dasari, M.S. Feld, *Phys. Rev. Lett.*, 1997, **78**, 1667-1670

[56] S. Lal, N.K. Grady, G.P. Goodrich, N.J. Halas, *Nano Lett.*, 2006, **6,** 2338–2343

[57] J.P. Camden, J.A. Dieringer, Y. Wang, D.J. Masiello, L.D. Marks, G.C. Schatz, R.P. Van Duyne, *J. Am. Chem. Soc.*, 2008, **130**, 12616-12617

[58] F. Mafune, J. Y. Kohno, Y. Takeda, T. Kondow, *J. Phys. Chem. B*, 2003, **107**, 4218-4223

[59] M. Procházka, P. Mojzeš, J. Štěpánek, B. Vlčková, P.Y. Turpin, *Anal. Chem.*, 1997, **69**, 5103-5108

[60] A.D. McFarland, M.A. Young, J.A. Dieringer, R.P. Van Duyne, *J. Phys. Chem. B*., 2005, **109,** 11279–11285

[61] L. D'Urso, G. Compagnini, O. Puglisi, *Carbon*, 2006, **44**, 2093-2095

[62] G. Compagnini, G. Baratta, *Appl. Phys. Lett.*, 1992, **61**, 1796-1798

[63] W. Park, W.Z. Kim, *Nano Lett*., 2010, **10**, 4040-4048

[64] K. Dick, T. Dhanasekaran, Z. Zhang, D. Meisel, *J. Am. Chem. Soc.*, 2002, **124**, 2312-2317

[65] Z. Zhang, X.X. Lü, Q. Jiang, *Physica B*, 1999, **270**, 249-254

[66] T. Kim, C.H. Lee, S.W. Joo, K. Lee, *J. Colloid Interface Sci.*, 2008, 318, 238–243

[67] J. Storhoff, A. Lazarides, C. Mucic, C. Mirkin, R. Lestinger, G. Schatz, *J. Am. Chem. Soc*., 2000, **122**, 4640-4650

[68] S.J. Kim, D.J. Jang, *Appl. Phys. Lett.*, 2005, **86**, 033112

[69] Y. Lu, J.Y. Huang, C. Wang, S. Sun, J. Lou, *Nature Nanotech.*, 2010, **5**, 218-224

[70] C. Liu, Y.J. Li, S.G. Sun, E.S. Yeung, *Chem. Commun.*, 2011, **47**, 4481–4483

[71] M. Ding, D.C. Sorescu, G.P. Kotchey, A. Star, *J. Am. Chem. Soc.*, 2012, **134**, 3472–3479

[72] J. Liao, Y. Zhang, W. Yu, C. Ge, J. Liu, N. Gu, *Colloids Surf. A*, 2003, **223**, 177-183

[73] T. Kim, C.H. Lee, S.W. Joo, K. Lee, *J. Colloid Interface Sci.* 2008, **318**, 238–243

[74] J.Y. Shim, V.K.. Gupta, *J. Colloid Interface Sci*., 2007, **316**, 977–983

[75] B.J. Berne, R. Pecora, "Dynamic Light Scattering" Whiley: New York, 1976

[76] B.M.I. Van Der Zande, J.K.G. Dhont, M.R. Bohmer, A.P. Philipse, *Langmuir*, 2000, **16**, 459–464.

[77] A.M. Shetty, G.M.H. Wilkins, J. Nanda, M.J. Solomon, *J. Phys. Chem. C*, 2009, **113**, 7129–7133

[78] P.F. Perrin, *J. Phys. Radium*, 1936, **1**, 1–11

[79] V. Amendola, M. Meneghetti, *J. Phys. Chem. C*, 2009, **113**, 4277–4285

[80] V. Amendola, S. Polizzi, M. Meneghetti, *J. Phys. Chem. B*, 2006, **110**, 7232–7237

CHAPTER 5: ALLOYING OF METAL NANOPARTICLES

5.1 INTRODUCTION

The increase of interest in alloying nanoparticles is due to the possibility of mixing properties of single nanocrystals in order to obtain structures with new characteristics that make them desirable starting materials for the production of devices.

For example, pure Fe nanocrystals act as strongly fluctuating superparamagnetic entities at room temperature, while FePt alloy nanoparticles are ferromagnetic, so they find potential application in the creation of ultrahigh density storage systems **[1]**.

An approach for the production of alloy nanoparticles contemplates the irradiation of a target with the composition of the desired alloy.

FePt alloys were produced by laser ablation of a $Fe_{50}Pt_{50}$ target in water and hexane but obtained particles presented stochiometries different from the target one **[2]**.

Literature reports that also PtIr **[3]**, NiFe and SmCo **[4]** nanoparticles have been produced by ablation of mixed metal targets in organic solvents. PtIr and NiFe nanoparticles maintained the stoichiometry of the target but this has not been noted in the case of the Sm-Co alloys. This

result has been attributed to the difference of heat of evaporation between the metals constituting the target **[4]**.

It has also been reported the preparation of Fe-Ni alloying nanoparticles by laser ablation of an iron-nickel target in flowing ethanol **[5]**.

Elongated alloys, like AuGe nanowires with widths of 5-10 nm and length 100 nm have been obtained by ablation in water as well. The target presented the eutectic AuGe stoichiometry, but a lower amount of Ge with respect to the starting material has been found in particles **[6]**.

This technique can also be applied to semicondutcors and nanoparticles have been obtained by ablation of either CdS or ZnSe crystals in water and organic solvents using a Cu vapour laser **[7]**.

Another approach to the production of alloys contemplates the irradiation and subsequent photolysis of precursors of the desired metal in liquid. Literature reports that FePt nanoparticles can be also prepared by this route, inducing the photolysis of iron and platinum precursors in methanol solutions with a KrF excimer laser **[8]**.

Also the synthesis of the metastable silver-nickel alloying nanoparticles has been reached by ablation of nitrate and acetate precursors of silver and nickel with CO_2 and Nd:YAG lasers **[9-10]**.

Mixed techniques contemplate the ablation of a pure metal target in precursors.

It has been demonstrated the formation of silver-nickel rods with 30-50 nm diameters and 300-500 nm lengths, obtained by 532 nm Nd:YAG laser ablation of a nickel target in silver nitrate solution. This result is of fundamental importance since silver and nickel present the same face

centered cubic crystalline structure so they are immiscible from the thermodynamic equilibrium point of view and their alloying is not possible with conventional techniques **[11]**.

The formation of the alloy phase is possible since Ni species inside the plasma can react at the interface with silver in a high temperature high pressure and high density environment, forming a metastable phase that is freezed by the short quenching time.

Increasing attention has been also directed to laser induced melting and vaporization of metal nanoparticles in liquid for the formation of alloys. For this approach, it is necessary that the irradiation wavelength partially overlaps the SPR of the particles.

There are several examples of Ag-Au alloy nanoparticles with different compositions prepared by irradiation at 532 nm Nd:YAG and 510.6 nm of mixtures of gold and silver nanoparticles in water or ethanol [**12-16**].

The plasmon resonance of the alloy presents an intermediate position between resonances of single metals and the peak position shifts in function of the metal ratio.

With the same approach different Au based alloys have been produced by ablation of mixed monometallic colloidal solutions at 532 nm Nd:YAG, such as Au-Zinc **[17]** and Au-Cu **[18]**.

Same results can be obtained starting from metal powder suspensions instead that from colloidal solutions, and the formation of Au/Ag alloys by laser ablation of pure metal powders in SDS aqueous solution has been reported **[19]**.

5.2 FORMATION OF Au/Ni SYSTEMS BY LASER MIXING IN LIQUID ENVIRONMENT

Particular interest has been dedicated to composite magnetic nanoparticles since their potential application in different fields as optics, electronics, and medicine **[20-21]**. Unfortunately, magnetic metals such iron, cobalt or nickel, which are often used for this purpose, present phenomena of surface oxidation. For such reason, it can be useful the interaction of the latter with a noble metal, that maintains unaltered properties as well as presenting high corrosion and oxidation resistance. Several approaches for preparing Ni/Au nanocomposites have been reported in past years, using both wet synthesis as reverse microemulsion **[22-23]** and physical route like ion beam mixing **[24]** or electrodeposition **[25]**. Problems correlated to these approaches are different: in the case of wet synthesis the surfactant that assure the presence of the inverse micelle needs to be removed from the surface of the particles, while in the case of physical approaches, nanoparticles can be only obtained in solid phase. Due to the possibility of alloying single metal nanoparticles by laser irradiation in order to obtain nanostructured alloys, it seems convenient to use this approach for the preparation of a Ni/Au system.

5.2a Preparation of Alloys

Au and Ni/NiO nanoparticles were produced by ablating with the first harmonic (λ=1064 nm) of a Nd:YAG laser (characteristics described in

section 4.2b) a rod of the desired metal (Au and Ni 99.99% by Goodfellow) submerged in Millipore grade water. Ablation was carried out for 15 min with a fluence of 30 J/cm^2. Obtained colloids have been mixed and irradiated with the unfocused beam of the same laser using the second harmonics (λ=532 nm) with a fluence of 0.2 J/cm^2 for 3 hours. The local heating of the water due to the laser irradiation leads to the convection of the colloidal mix, assuring that the whole volume undergoes irradiation.
As prepared, mixed and mixed and irradiated colloids were analyzed with a UV-Visible spectrometer (model V-650 by JASCO).

5.2b Characterization of Alloys

Fig. 5.1 reports the extinction spectra of prepared colloids. It is clearly visible how golden nanoparticles, reported as a red line in figure, show the typical plasmon band at 520 nm. On the other way, the spectrum of particles prepared by ablation of nickel (black line in figure) does not show any particular feature. As reported in literature, the ablation of a nickel target leads to the formation of Ni/NiO core-shell nanoparticles **[26]** and if the oxide layer on the surface of the metal is thick enough, it can impede the oscillation of free electrons.
Since nanosecond laser irradiation induces the optical breakdown of water **[27]**, with subsequent formation of reactive oxygen radicals, it is possible the reaction of these species with nickel and the subsequent formation of an oxide shell on the surface of the nanoparticle.

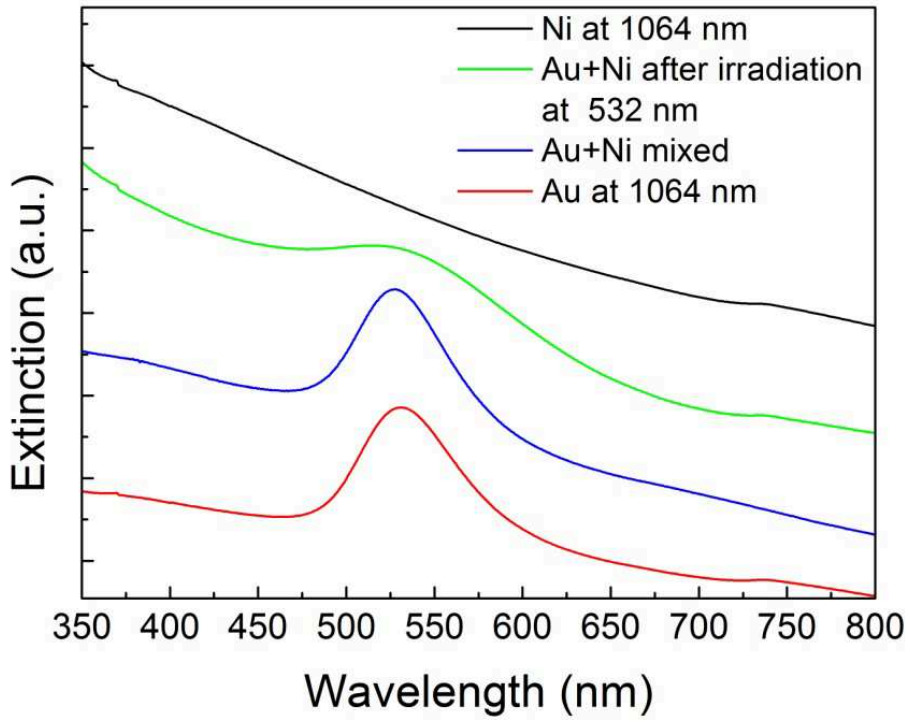

Figure 5.1 Extinction spectra of colloidal solutions of Au nanoparticles (red line), Ni/NiO nanoparticles (black line), mixed solution of Au-Ni/NiO nanoparticles (blue line), irradiated solution of mixed solution of Au-Ni/NiO nanoparticles (green line).

The extinction spectrum of the mixed colloid, reported as a blue line in figure, does not show any relevant difference with the spectrum of the gold colloid on its own. Since the nickel spectrum presents no signal at all, this behaviour can be attributed to the absence of interactions of the two colloids when they are mixed. Contrariwise, the extinction spectrum

of the system after irradiation (green line), presents a weak shift at higher wavelengths and a broadening of the peak width. In literature is reported that smaller nanoparticles present an enlargement of the band width due to the presence of electron scattering surface phenomena, so a broadening of the peak seems a direct consequence of the laser irradiation **[28]**. As reported elsewhere **[29]**, if the wavelength used for irradiation is near to the plasmon absorption of treated nanoparticles, light absorption can happen and can lead to the fragmentation of the nanoparticles themselves by different mechanisms. Since the wavelength used for the irradiation is the second harmonic of a Nd:YAG laser (λ=532 nm), it is probable that gold nanoparticles underwent fragmentation and for this reason their plasmon absorption band is widened.

To investigate the crystal phase of obtained structures, some drops of the dispersion have been deposited on a Si substrate for X-Ray Diffraction (XRD) analysis. XRD measurements were performed with a Rigaku Ultima IV type III diffractometer (Rigaku, Tokyo, Japan) equipped with cross beam optics (CBO) by using a Kα wavelength emitted by a Cu anode. Careful alignment of source and detector with respect to the sample was reached by using a thin film attachment with three degrees of freedom. In order to avoid beam defocusing, the measurements were carried out in parallel beam mode. Divergence of the primary beam was reduced by a 5° Soller slit, while divergence of the diffracted beam was reduced by a 0.5° horizontal Soller slit. For GIXRD measurements, the incident angle was kept at 0.5° to avoid any significant scattering from the substrates.

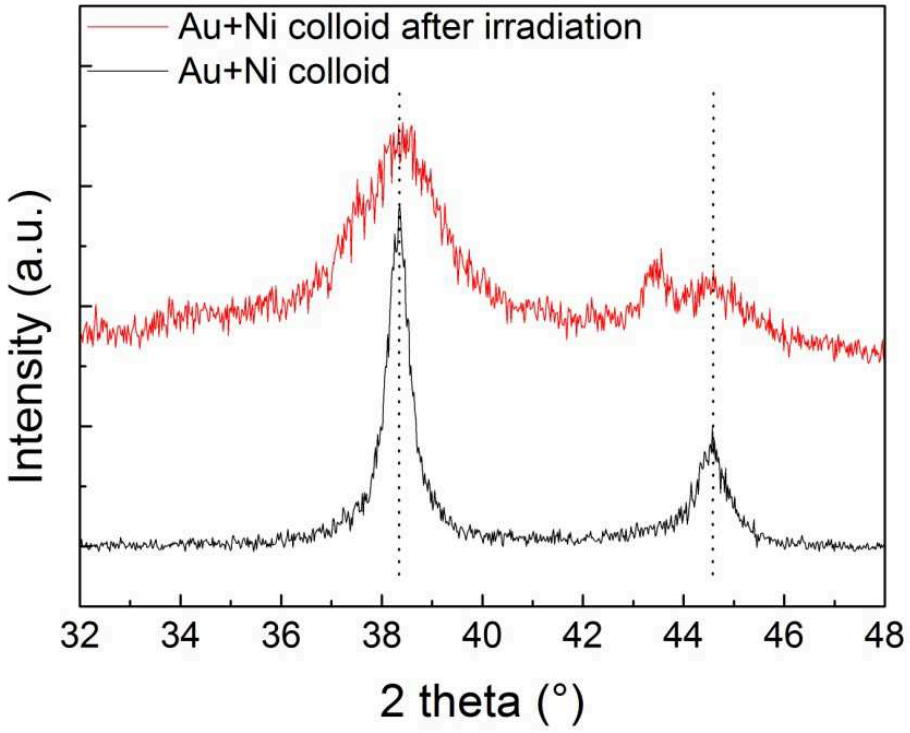

Figure 5.2 X-Ray Diffraction spectra of mixed Au-Ni/NiO particles solutions before (black line) and after (red line) irradiation at 532 nm.

The diffraction pattern of the mixed colloid (black line in figure) reports the presence of two main peaks. From comparison with literature data **[22,23,25,30]**, the signal at lower angle (38.3°) has been attributed to Au (111), while the one at higher angle value (44.6°) has been attributed to the presence of both Au (200) and Ni (111). After the irradiation of the mixed colloid, it is possible to note a variation on the features of the diffractogram. First of all, it is clearly visible the appearance of a new peak at a value of 2θ of 43.4°. Vegard's law theoretically predicts that

the component of an alloy system should present a diffraction peak at an intermediate angle between the peaks of the single components **[24]**. The position of the peak will depend on the ratio between the two metal components, since the reticular parameter varies on the relative amount of one metal respect to the other. Theoretical predictions have been confirmed by experimental data, by reporting the variation of the peak position at different Au/Ni ratio **[24,31]**. Reticular constant values as a function of the Ni ratio calculated by Vegard's law and obtained by literature references **[24,31]** have been reported in fig. 5.3.

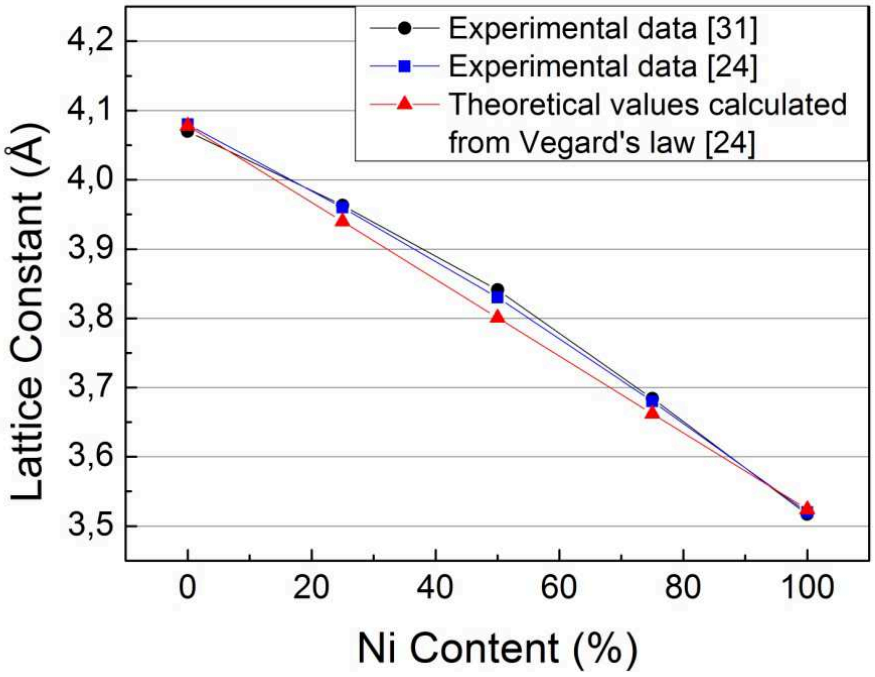

Figure 5.3 Lattice constant as a function of the Ni content for an Au/Ni alloy. Black point data from ref. **[31]**, blue squares and red triangles data from ref. **[24]**.

From Bragg's law it has been calculated that obtained mixed system presents a reticular parameter of 3.59 Å. From comparison with data reported in fig. 5.3, such calculated lattice constant corresponds to an alloy with a relative percentage of 90% of Nickel.

From the study of the phase diagram of a gold/nickel system reported in fig. 5.4, it is possible to note how the alloy phase can be obtained at lower temperatures when one of the two metals is predominant.

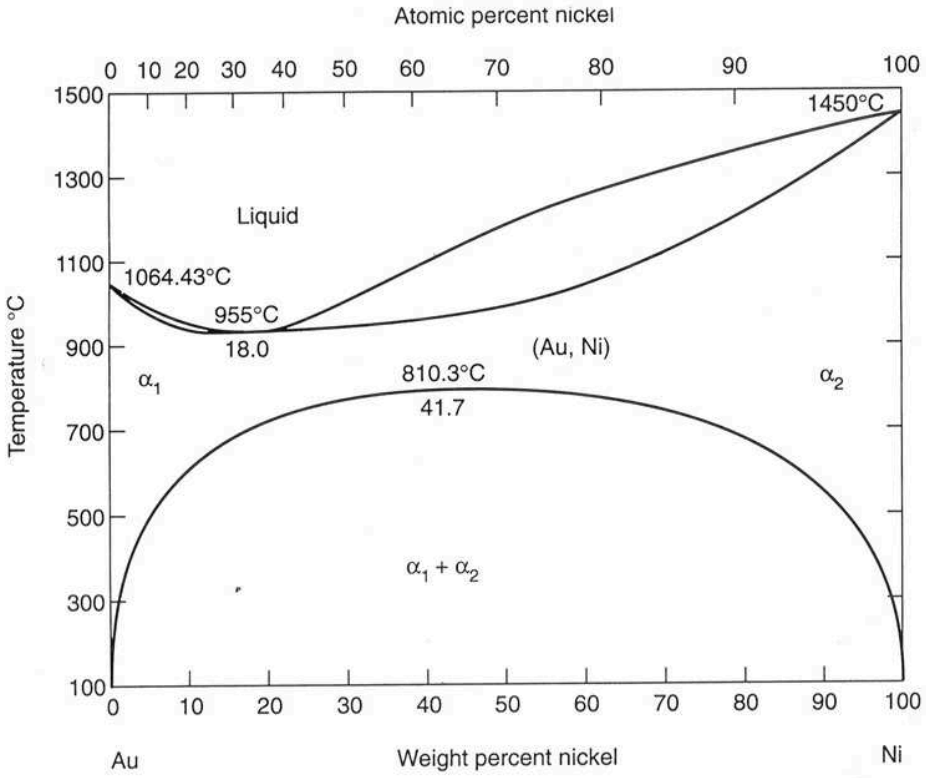

Figure 5.4 Au-Ni phase diagram. From ref. **[32]**.

Literature reports a theoretical model that allows calculating the temperature reached from gold nanoparticles when irradiated by a wavelength overlapping the surface plasmon resonance **[33]**

Temperature in Kelvin is given by:

$$T = \frac{Q - \Delta H_{melt} - \Delta H_{vap}}{C_p} + 293 \quad (5.1)$$

where Q is the laser energy absorbed by the gold particles per mass unit of gold atom and one pulse in J/(g·pulse), ΔH_{melt} is the heat of melting (6.28×10 J/g), ΔH_{vap} is the heat of vaporization (1.87×10^3 J/g) and C_p is the specific heat (0.131 J/g·K) which is independent of the phase **[33]**.

The contribution of ΔH_{vap} can be neglected if reached temperature is lower than the vaporization temperature of gold. The use of bulk physical constant to estimate the temperature of nanostructures may be justified by the fact that the melting point of the gold particles decreases drastically only when the particle size is lower than 5 nm **[34-35]**.

Heat loss for conductive/convective exchanges with the surrounding water and the radiative transfer can be omitted because it is negligible within the pulse duration **[33]**.

Q is defined by the following equation **[33]**:

$$Q = \frac{E}{RCV} \quad (5.2)$$

Where E is the laser energy absorbed by the solution of the gold particle per unit time (J/s) as measured by the power meter, R is the repetition rate of the pulsed laser (10 Hz), C is the mass concentration of gold (g/m^3), and V is irradiated volume of the solution (m^3).

Considering experimental parameters used for irradiation, it has been calculated that nanoparticles reach approximately a temperature of 750-800°C, which, as shown in the Au-Ni phase diagram, is sufficient to reach the alloy phase when the alloy composition presents a strong percentage of Ni.

In the XRD diffractogram in fig. 5.2 it is also possible to note an increase of the peak width after the irradiation of the system. Scherrer's equation allows correlating the dimension of nanocrystals smaller than 1000 Å with the full width at half maximum of the diffraction peak.

Thus, the mean diameter can be expressed by Scherrer's equation as follows:

$$D = \frac{k\lambda}{\beta \cos\theta} \tag{5.3}$$

Where k is the shape factor, λ is the used exciting wavelength, β is the FWHM expressed in radians and θ is the Bragg angle.

The shape factor k can assume values ranging from 0.89 for spherical particles to 0.94 for cubic particles. For particles with unknown shapes this value can be assumed equal to 0.9

To calculate the size reduction, Au(111) peaks have been considered and are reported in fig. 5.5

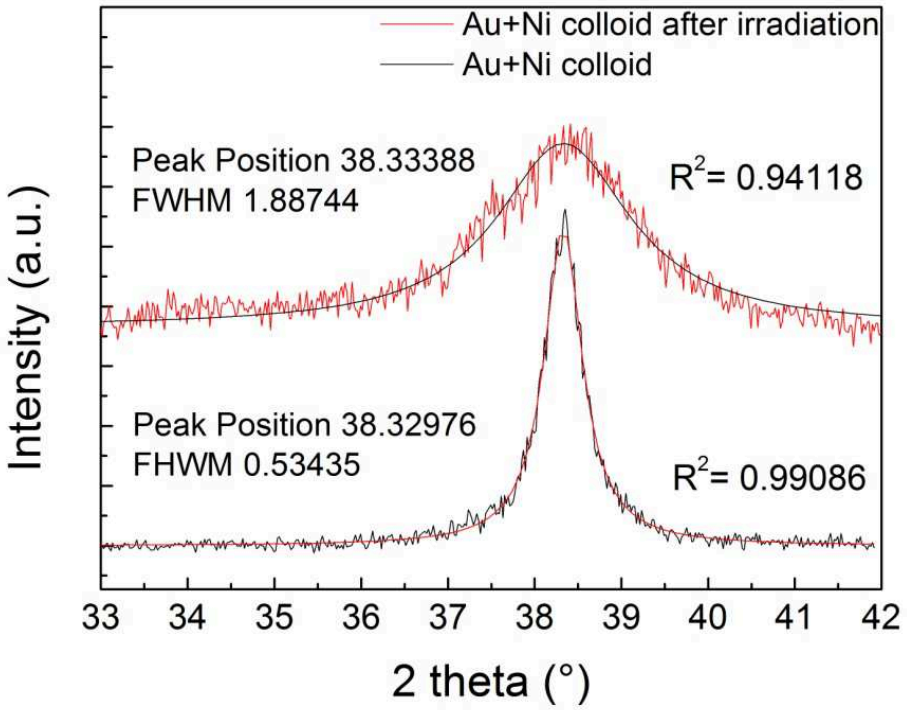

Figure 5.5 X-Ray diffractogram showing the Au(111) peaks and their fitting with Lorentzian distributions for mixed Au-Ni/NiO colloids before (black line) and after (red line) irradiation at 532 nm.

Here, a fitting based on a Lorentzian distribution has been applied to the peaks in order to obtain values of peak position and FWHM, and these values have been substituted into Scherrer's equation.

Calculations have demonstrated that gold nanoparticles before irradiation present a size of around 16.8 nm, which is in accordance with average values of dimension of gold nanoparticles obtained by laser ablation in water **[36]**. On the other way, when particles undergo irradiation, the dimension calculated by the Scherrer's equation is 6.4 nm. The reduction

of dimensions shown by gold nanoparticles confirms the hypothesis on particles fragmentation based on UV-Vis spectra.

However, literature reports that reached temperature (750-800°C) is not enough to have evaporation of the gold from the surface of nanoparticles and a subsequent size reduction **[33]**, thus meaning that other mechanisms should be involved for the lowering of size.

Reduction of nanoparticles dimension has also been attributed to a Coulomb explosion model which presumes the ejection of a large number of electrons to generate multiple ionized nanoparticles that undergo spontaneous fission because of the charge repulsion. Evidences of this mechanism have been found in nanosecond laser ablation **[37-38]** and probably this mechanism is responsible for the variation of size of gold nanoparticles reported in this work.

To obtain confirmation of the nanoparticles size, irradiated system has been analysed by Scanning Electron Microscopy and images are reported in fig. 5.6.

SEM images show the presence of a large number of very small particles, with dimensions lower than 10 nm (fig. 5.6), which is in accordance with values obtained by Scherrer's equation and thus confirming the fragmentation phenomenon discussed above.

It is also possible to note the presence of some bigger particles, with diameter in the order of the hundred nanometers.

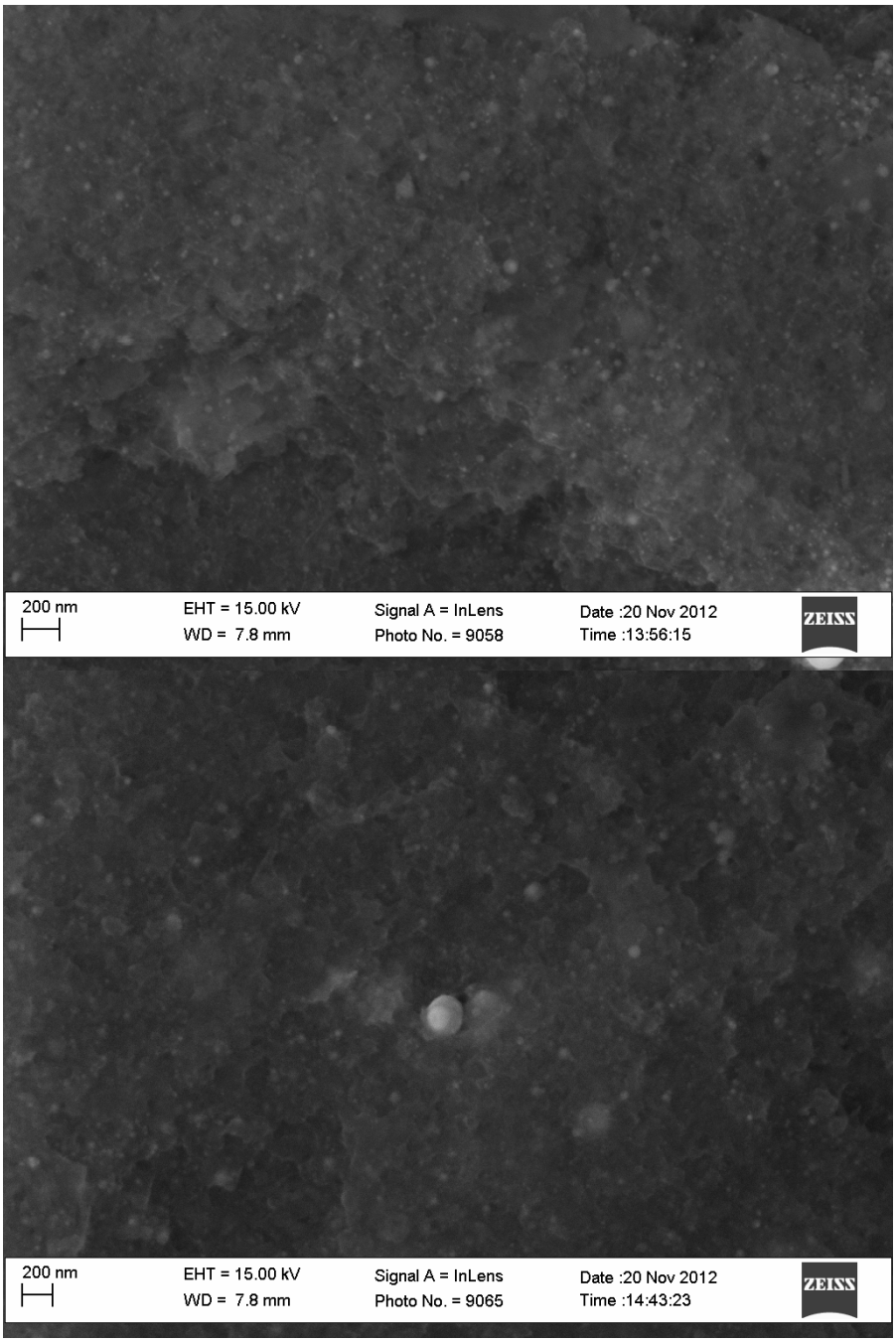

Figure 5.6 SEM images of the obtained Au/Ni systems.

Analysis of the composition of nanoparticles has been operated through Energy Dispersive X-Ray Spectroscopy (EDX) and results are reported in fig. 5.7.

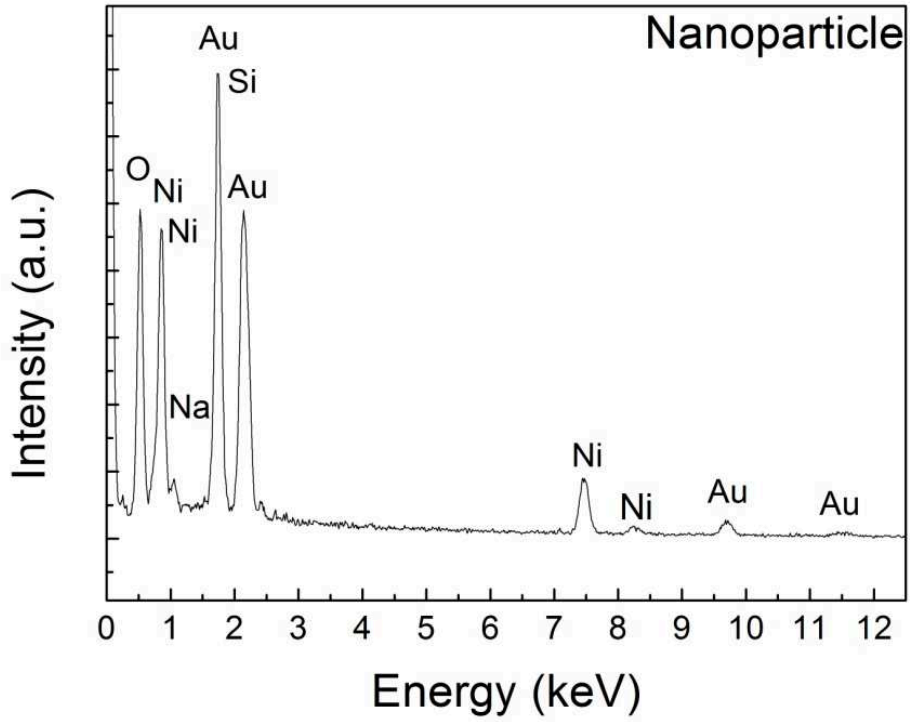

Figure 5.7 EDX spectrum showing the composition of Au/Ni mixed nanoparticles.

The spectrum shows the presence of intense peaks attributed to Ni, Au and O, corresponding to the elemental composition of alloy systems. It is also possible to note the presence of Si and Na peaks. The Si signal is due to the substrate used for the deposition, while the presence of Na derives from the water used as ablation environment. A quantitative

analysis can be obtained by the atomic weight percentages of these elements reported in tab. 5.1

The most interesting feature is the presence of a metal ratio of Au/Ni of around 1/10, which is in accordance with hypothesis based on the calculation of reticular parameter obtained by XRD. Tab. 5.1 reports also a relevant amount of O, which can attribute both to the presence of Ni and Si oxides.

To evaluate the contribution of these species to the amount of oxygen, EDX analysis have been operated also on the substrate and the spectrum is shown in fig. 5.8.

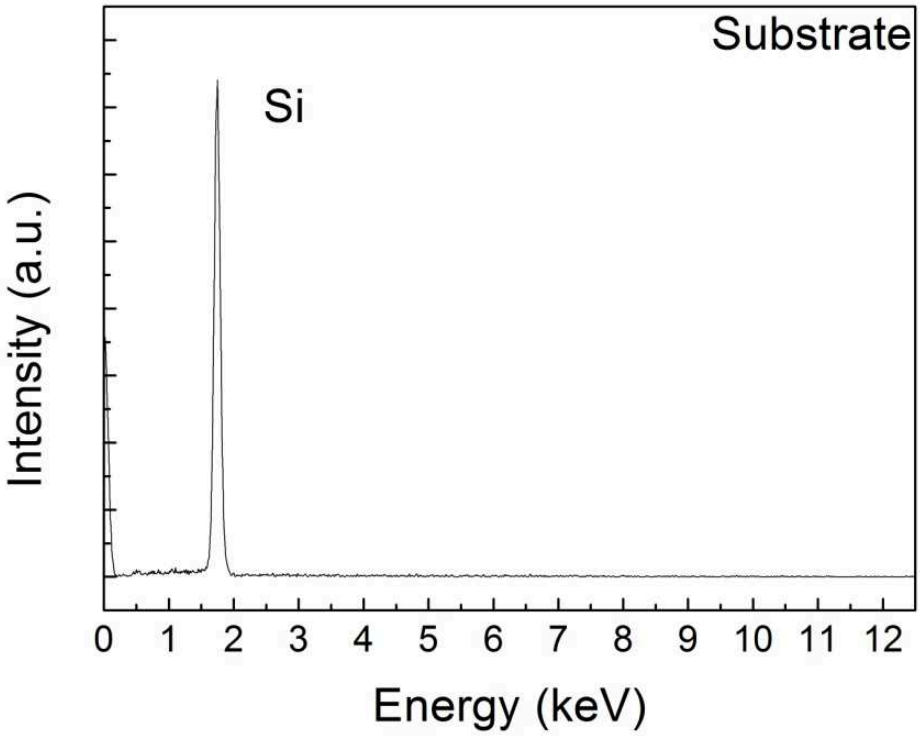

Figure 5.8 EDX spectrum showing the composition of the substrate.

Here, it is possible to note the absence of peaks corresponding to O species and a low O atomic weight percentage is reported in tab. 5.2, thus meaning that the substrate oxidation is negligible. For this reason, the high amount of oxygen reported in the spectrum of nanoparticles in fig. 5.7 has to be attributed mainly to the contribution of the alloy systems, which still present a strong NiO component.

Element	**Atomic Weight Percentage**
Si	27.33%
O	47.69%
Ni	20.33%
Au	1.95%
Na	2.39%

Table 5.1 Elemental atomic weight percentage of EDX spectrum reported in fig. 5.7

Element	**Atomic Weight Percentage**
Si	83.2%
O	15.35%
Ni	1.32%
Au	0.14%

Table 5.2 Elemental atomic weight percentage of EDX spectrum reported in fig. 5.8

The presence of single metal particles has not been revealed by EDX analysis, thus demonstrating the complete alloying of the sample.

The proposed mechanism for the formation of mixed systems is based on the assumption that Au NPs absorb the laser radiation and undergo fragmentation by Coulomb explosion. Small clusters formed by this process can get in contact with Ni/NiO particles in a relative low temperature environment, which is favorable to the formation of the alloy metastable phase with a dominant amount of Ni.

REFERENCES

[1] S.H. Sun, C.B. Murray, D. Weller, L. Folks, A. Moser, *Science*, 2000, **287**, 1989-1992

[2] Y. Ishikawa, K. Kawaguchi, Y. Shimizu, T. Sasaki, N. Koshizaki, *Chem. Phys. Lett.*, 2006, **428**, 426–429

[3] J. Jakobi, A. Menéndez-Manjón, V.S.K. Chakravadhanula, L. Kienle, P. Wagener, S. Barcikowski, *Nanotech.*, 2011, **22,** 145601-145607

[4] J. Jakobi, S. Petersen, A. Menéndez-Manjón, P. Wagener, S. Barcikowski, *Langmuir*, 2010, **26**, 6892–6897

[5] W.G. Zhang, Z.G. Jin, *Sci. China Ser. B*, 2004, **47**, 159-165

[6] O.R. Musaev, E.A. Sutter, J.M. Wrobel, M.B. Kruger, *J. Nanopart. Res.*, 2012, **14**, 654

[7] K.V. Anikin, N.M. Melnik, A.V. Simakin, G.A. Shafeev, V.V. Voronov, A.G. Vitukhnovsky, *Chem. Phys. Lett.*, 2002, **366**, 357-360

[8] M. Watanabe, H. Takamura, H. Sugai, *Nanoscale Res. Lett.*, 2009, **4**, 565–573

[9] D. Poondi, J. Singh, *J. Mater. Sci.*, 2000, **35**, 2467-2476

[10] D. Poondi, T. Dobbins, J. Singh, *J. Mater. Sci.*, 2000, **35**, 6237-6243

[11] Q.X. Liu, C.X. Wang, W. Zhang, G.W. Yang, *Chem. Phys. Lett.*, 2003, **382**, 1-5

[12] Y.H. Chen, C.S. Yeh , *Chem. Commun.*, 2001, **4**, 371-372

[13] A.T. Izgaliev, A.V. Simakin, G.A. Shafeev, *Quantum Electron.*, 2004, **34**, 47-50

[14] A.T. Izgaliev, A.V. Simakin, G.A. Shafeev, F. Bozon-Verduraz *Chem. Phys. Lett.*, 2004, **390**, 467-471

[15] G.Compagnini, E.Messina, O.Puglisi, V.Nicolosi, *Appl. Surf. Sci.*, 2007, **254**, 1007-1011

[16] G. Compagnini, E. Messina, O. Puglisi, R.S. Cataliotti, *V. Nicolosi, Chem. Phys. Lett.*, 2008, **457**, 386–390

[17] F. Hajiesmaeilbaigi, M. Fazeli Jadidi, A. Motamedi, *Acta Phys. Polonica A*, 2012, **121**, 59-61

[18] M. Ganjali, M. Ganjali, S. Khoby, M.A. Meshkot, *Nano-Micro Lett.* 2011, **3**, 256-263

[19] J. Zhang, J. Worley, S. Dénommée, C. Kingston, Z. Jakubek, Y. Deslandes, M. Post, B. Simard, *J. Phys. Chem. B*, 2003, **107**, 6920-6923

[20] M. Spasova, V. Salgueiriño-Maceira, A. Schlachter, M. Hilgendorff, M. Giersig, L.M. Liz-Marzán, M. Farle, *J. Mater. Chem.*, 2005, **15**, 2095-2098

[21] S. Mornet, S. Vasseur, F. Grasset, E. Duguet, *J. Mater. Chem.*, 2004, **14**, 2161-2175

[22] D. Chen, S. Liu, J. Li, N. Zhao, C. Shia, X. Dua, J. Sheng, *J. Alloys Compounds*, 2009, **475**, 494-500

[23] H.K. Chiu, I.C. Chiang, D.H. Chen, *J. Nanopart. Res.*, 2009, **11**, 1137-1144

[24] B.Y. Tsaur, M. Mäenpää, *J. Appl. Phys*., 1981, **52**, 728-735

[25] E. Rouya, G.R. Stafford, U. Bertocci, J.J. Malletta, R. Schad, M.R. Begleya, R.G. Kelly, M.L. Reede, G. Zangaria, *J. Electrochem. Soc.*, 2010, **157**, D396-D405

[26] M.K. Singh, A. Agarwal, R.K. Swarnkar, R. Gopal, R.K. Kotnala *Sci. Adv. Mater.*, 2012, **4**, 532-536

[27] C.A. Sacchi, *J. Opt. Soc. Am. B*, 1991, **8**, 337-345

[28] W.A. Kraus, G.C. Schatz, *J. Chem. Phys.*, 1983, **79**, 6130-6139

[29] S. Hashimoto, D. Werner, T. Uwada, *J. Photochem. Photobiol. C*, 2012, **13**, 28–54

[30] D. Wang, P. Schaaf, *Mater. Lett.*, 2012, **70**, 30-33

[31] E.C. Ellwood, K.Q. Bagley, *J. Inst. Metals*, 1951-1952, **80**, 617

[32] http://oregonstate.edu/instruct/me581/Homework/Overheads/Au-Ni-PD.jpg

[33] A. Takami, H. Kurita, S. Koda, *J. Phys. Chem. B*, 1999, **103**, 1226–1232

[34] M. Takagi, *J. Phys. Soc. Jpn.*, 1954, **9**, 359-363

[35] D.A. Buffat, J.P. Borel, *Phys. Rev. A*, 1976, **13**, 2287-2298

[36] L. D'Urso, G. Grasso, E. Messina, C. Bongiorno, V. Scuderi, S. Scalese, O. Puglisi, G. Spoto, G. Compagnini, *J. Phys. Chem. C.*, 2010, **114,** 907-915

[37] K. Yamada, Y. Tokumoto, T. Nagata, F. Mafune, *J. Phys. Chem. C*, 2006, **110**, 11751–11756.

[38] K. Yamada, K. Miyajima, F. Mafune, *J. Phys. Chem. C*, 2007, **111**, 11246–11251

CONCLUSIONS

This thesis has reported some advances in the production, modification and characterization of metal nanoparticles obtained by laser ablation in liquid environment in view of their use as starting materials for the development of technological devices.

In the first part it has been demonstrated how the ablation of a metal wire in a water flow chamber increases the productivity of silver nanoparticles of a factor 15 with respect to bulk ablation. The production rate has shown a strong dependence on the wire thickness, as well on laser parameters as fluence and repetition rate. The model proposed to describe the dependence on the target thickness includes considerations about heat loss phenomena inside the wire itself and from the wire to the surrounding water, the reflectivity of the surface and the cavitation bubble mechanism. In particular, the cavitation bubble mechanism during wire ablation involves the ejection of a large amount of material from the wire due to a rebound effect.

The second part of the thesis has been centered on the manipulation of nanoparticles by different techniques for a controlled variation of their properties.

Modifications on the plasmon resonance have been obtained by conjugating silver nanoparticles through carbon nanowires, also prepared by laser ablation in water. The efficiency of conjugation is strongly

influenced by the purity of the surface of nanoparticles, which depends on the wavelength used for particles production. These hybrid systems have demonstrated increased SERS activity due to the resonance of the irradiating wavelength with the surface plasmon peaks.

The spontaneous aggregation of gold nanoparticles has been monitored in liquid environment by the use of spectroscopy in order to extend the control on cold-welding approaches in liquid.

Polarized DLS measurements have revealed the formation of dimers after a period of 20 days, and these results have been confirmed by UV-Vis spectroscopy, demonstrating how these techniques are determinant for the study of aggregation phenomena of nanoparticles in liquid.

The modification of single metal properties can be obtained by alloying nanoparticles and in particular, Au/Ni mixed alloys have been prepared by irradiation of a mixture of Au and Ni/NiO colloids obtained by laser ablation in liquid.

Obtained alloys present an Au/Ni ratio of 1 to 10 and this composition has been attributed to the relative low temperature environment in which these structures are formed.

The work of this thesis, through a wide look to synthesis and application aspects, wants to represent a small contribution to the demonstration that laser prepared metal nanoparticles can assume a relevant role in future improvement of nanotechnology. Indeed, the possibility of increase the productivity of nanoparticles, together with a proper modification of their properties, will be crucial aspects for possible industrial developments.

ACKNOWLEDGEMENTS

I would like to thank Prof. Giuseppe Compagnini, my research tutor, for the supervision throughout these years.
I gratefully acknowledge the LABFSN Research Group and in particular Marco G. Sinatra for the XPS measurements and Dr. Elena Messina.
I would like also to express my sincere gratitude to Prof. Stephan Barcikowski for the possibility to work at the Technical Chemistry I and CENIDE laboratories at University of Essen. My appreciation goes to the TCI Research Group too, in particular to Dr. Philipp Wagener for the useful discussions and hints and to René Streubel for the scientific and technical support.
I would like to offer my thanks to Prof. Alessandro De Giacomo at University of Bari and Dr. Antonio Santagata at CNR-IMIP of Potenza for the plasma and cavitation bubble characterization analysis.
My gratitude goes also to Dr. Massimo Zimbone of Physics Department at University of Catania for the DLS measurements and the plasmon resonance simulations.
Many thanks to Dr. Silvia Scalese at CNR-IMM of Catania for TEM images.
I am grateful to Dr. Giovanni Li Destri Nicosia for the XRD measurements. I would like to acknowledge Prof. Giovanni Marletta and

the LAMSUN Research Group of Chemistry Department at University of Catania as well.

My appreciation goes also to Dr. Maria Elena Fragalà of the Engineering Department at University of Catania for SEM and EDX characterizations.